

POLITECNICO DI TORINO

Master's Degree in Biomedical Engineering



**Politecnico
di Torino**



**UNIVERSITÀ
DI TORINO**

Master's Degree Thesis

Image-Guided Surgery and Augmented Reality in Orthopaedic Surgery: a perspective on reducing Iatrogenic Nerve Damage in Elbow

Supervisors

Prof. Filippo MOLINARI

Prof. Massimo SALVI

Prof. Corrado CALÌ

Candidate

Antonio CANGELOSI

2023/2024

Summary

Image-guided surgery (IGS) techniques are the basis of minimally invasive surgeries (MIS). The integration of minimally invasive surgery with the state of the art of augmented reality (AR) significantly improves surgical practice. It promotes: (i) safety during medical procedures for patients, operators, and surrounding personnel; (ii) optimization of execution times; (iii) increased precision in surgery.

Minimally invasive surgery has an inherent risk of damage to nerves and vascular structures. This is called 'iatrogenic damage' and causes about 20% of traumatic nerve injuries. The purpose of this study is to simulate a system of image-guided surgery integrated with augmented reality, in order to assess the possibility of reducing the risk of iatrogenic damage during the insertion of screws and k-wires in orthopedic surgery. Furthermore, the benefits on reduction X-ray radiation exposure and intervention time will be demonstrated.

The system, presented in the following work, consists of two subsystems: i) tracking, and ii) X-ray simulation and AR guidance. The first module, developed in Python, enables the recognition of passive marker. For this purpose, raw data acquired from a time-of-flight IR camera is processed according to the framework of an infrared optical tracking system (NIOTS). The "X-ray simulation and AR guidance system", is developed in Unity software. The 3D coordinates provided by the tracking system are used to reconstruct the spatial pose of tools equipped with markers on a custom physical phantom. This phantom replicates the anatomy from the distal third of the arm to the proximal third of the forearm, starting from the olecranon of the elbow. The tracking system simulates an operative C-Arm for X-rays (displayed on a traditional monitor) and provides AR guidance (with HoloLens) for the insertion of k-wires into targeted positions on the phantom.

The overall performance of the system is evaluated by the accuracy of measurements. An average discrepancy of $1.06 \text{ mm} \pm 2.78$ is observed, by comparing a dataset of 45 measurements from a vernier caliper, on the physical phantom, with the corresponding ones in the virtual model.

The dataset used for the study was collected at the "Palazzo degli Istituti Anatomici dell'Università di Torino" and C.T.O Hospital in Turin. For the assessment of iatrogenic damage risk reduction, quali-quantitative data gathering process was executed among 20 testers. This evaluation occurred according to a multi-phase protocol in medical students and orthopedic residents. In the "Phase 0" the X-ray simulator is provided as insertion guide. In subsequent phases, the participants were provided with a holographic guide that was superimposed onto the simulation scenario. The design of these phases also aimed to assess a potential learning effect associated with the use of this technology and the improvement in participants' procedural execution skills.

In summary, the system's testing and design demonstrate improved surgical performance and training efficacy with the AR system. For future improvements guidelines are proposed. These include the integration of convolutional neural networks (CNNs) with a different sensors and Hardware configuration for data acquisition, processing and visualization.

Table of Contents

List of Tables	VIII
List of Figures	IX
Acronyms	XIII
1 Introduction	1
1.1 Iatrogenic peripheral nerve injuries	1
1.1.1 Nerve Anatomy	1
1.1.2 Categorization of Nerve Lesions	2
1.1.3 Identification of Injuries and Surgery Management	3
1.2 Nerve Injuries Post Orthopedic Elbow Surgery	3
1.2.1 Elbow Anatomy	3
1.2.2 Injuries mechanisms, incidence and risk factors	4
1.2.3 Prevention Strategies	5
1.3 Image-guided surgery and Augmented Reality	6
1.3.1 Intraoperative image-guided surgery systems	6
1.3.2 Augmented Reality	8
1.3.3 Accuracy evaluation International Standard	10
2 Tracking System Development	11
2.1 Tracking systems overview	11
2.2 Experimental Setup	12
2.2.1 Acquisition System (Kinect Azure DK)[53]	12
2.2.2 Tracking Tools	15
2.2.3 Simulation Elbow Phantom	17
2.3 Acquisition Data Software framework	18
2.3.1 Raw Data	18
2.3.2 Segment Detection and Rejection	19
2.3.3 Centroid Detection	21
2.3.4 Point Correspondence	22

2.3.5	Data filtering	25
2.4	Acquisition Data Software UI and Communication Protocol	28
2.4.1	User Interface Overview	28
2.4.2	UDP communication protocol	29
3	X-Ray Simulator and AR Guide System Development	30
3.1	X-ray and AR guidance system overview	30
3.1.1	X-ray in trauma procedures	30
3.1.2	AR system in trauma	31
3.1.3	Hololens 2 [65]	32
3.2	Tracking Tools Pose Estimation	33
3.2.1	Local Reference System Calculation Algorithm	33
3.2.2	Local Reference System for Tracking Tools	34
3.2.3	Phantom Reference Frame Positioning	34
3.3	X-ray and AR guidance system Interface	35
3.3.1	X-Ray Simulator	35
3.3.2	AR guidance system	36
3.3.3	System Settings Interface	38
4	System Performance and Testing Protocol	39
4.1	System Performance Evaluation	39
4.1.1	Accuracy and Precision	40
4.1.2	Fiducial Points	40
4.1.3	Manual and Automatic Distance Measurements	43
4.2	Testing Protocol	44
4.2.1	Objectives	44
4.2.2	Testing Environment	44
4.2.3	Workflow	45
5	Results	47
5.1	System Performance Data Analysis	47
5.1.1	Point's relative location in a coordinate system	47
5.1.2	Repeatability of single-point coordinates	49
5.1.3	Relative point to point accuracy	58
5.2	Data Testing Analysis	65
5.2.1	Duration	65
5.2.2	Radiation Picture Counts	66
5.2.3	Anatomical	67

6	Discussion	73
6.1	System Development Principles	73
6.1.1	Hololens integrated System	74
6.1.2	Modular System Development	76
6.1.3	System Criticism and Development Advancements	80
6.2	Results	86
6.2.1	System Performance Data Analysis	86
6.2.2	Data Testing Analysis	87
7	Conclusion	89
A	Protocol tables	90
A.1	Acquired Points for Accuracy Evaluation at Different Distances . .	93
	Bibliography	95

List of Tables

5.1	Coordinates error in x,y,z at different camera distances: 0.3m (N=16); 0.4m (N=24); 0.5m (N=24); 0.6m (N=24)	48
5.2	Ideal Distances between fiducial Points	59
5.3	Mean and Standard Deviation Difference Values (N=42 for each distance)	61
5.4	Calibre Measurements for Different Targets	62
5.5	Automatic Measurements for Different Targets	63
5.6	Statistical Duration Measures for Each Phase (Phase 0 (N=33) Phase 1 (N=23); Phase 2 (N=6))	65
5.7	Radiation Picture Counts Across Different Phases (Phase 0 (N=33) Phase 1 (N=23); Phase 2 (N= 6))	66
5.8	Distance from Brachial Artery ((Phase 0 (N=33) Phase 1 (N=23); Phase 2 (N=6)))	68
5.9	Distance from Median Nerve ((Phase 0 (N=33) Phase 1 (N=23); Phase 2 (N= 6)))	70
5.10	Distance from Ulnar Nerve (Phase 0 (N=33) Phase 1 (N=23); Phase 2 (N= 6))	72
6.1	Comparison of Kinect Azure DK and Intel RealSense D435i	76
6.2	Comparison of circle detection algorithms.	77
6.3	Mean Processing Times for Circle Detection (632 frames)	79
6.4	Mean Processing Times for Matching Problem Resolution	80
A.4	Phase 1 additional steps	90
A.1	Test steps table	91
A.2	ECP steps table	92
A.3	PA steps table	92
A.5	Points Repeatability at 30cm	93
A.6	Points Repeatability at 40cm	93
A.7	Points Repeatability at 50cm	94
A.8	Points Repeatability at 60cm	94

List of Figures

1.1	Peripheral nerve architecture	2
1.2	Vascularization (left) and Innervation (right) of the elbow.	3
1.3	7D Surgical MvIGS system (left) and 7D Surgical’s trackable surgical tools (right)	7
1.4	3D IV image overlay in spine surgery	9
1.5	Blueprint Phantom in ASTM F2554-10	10
2.1	Experimental Setup	12
2.2	Representation of Kinect Azure DK with color and infrared images captured by the device	13
2.3	TOF phase-measurement principle in AMCW sensors [55].	13
2.4	Kinect FOV and Coordinate System	14
2.5	Drill Guide for k-Wires insetion	15
2.6	Stand for Dummy	16
2.7	NDI spherical markers	16
2.8	Complete model of the elbow including, muscles, nerves, vessels, bones and skin.	17
2.9	On the left are shown the nerves, on the right the vascular structures in the virtual model.	17
2.10	Raw Image from IR camera. On the right image with enhanced contrast	18
2.11	Thresholded Image	19
2.12	Hough Circle Transformation: Circle Mask (OpenCV)	19
2.13	a) Edge points contribute to the accumulator space; b) Edge points contribute to a single point in the accumulator.	20
2.14	sphere labeled with coordinates x_i, y_i, z_i	21
2.15	Marker Labelling for Guide Tracking Tool	23
2.16	Procrustes Analysis	24
2.17	Filtered Marker Data with Kalman Filter	27
2.18	Acquisition Data User Interface	28

3.1	C-Arm for Scintigraphy	31
3.2	Hololens 2	32
3.3	Tracking Tool Local Reference System	34
3.4	X-ray emulator	35
3.5	HMD view of AR scene during insertion	36
3.6	Command Menu displayed in AR user interface	37
3.7	System Settings Interface	38
4.1	Difference between accuracy and precision	40
4.2	Fiducial Markers on Stand	41
4.3	Tool Poses for Coordinate Acquisition in Fiducial Points	41
4.4	Tool User Interface for Performance Estimation	42
4.5	Point recording tool positioning guide	42
4.6	Tool User Interface for Performance Estimation	43
4.7	Distance Registration with Gauge	43
4.8	Protocol phases execution workflow	45
4.9	k-Wires representation in x-Ray AP view	46
5.1	Relative position acquired points - fiducial markers on stand	47
5.2	Euclidean Acquisition error Distance with Standard Deviation.Distances: 0.3m(N=16); 0.4m (N=24) 0.5m (N=24);0.6m (N=24)	48
5.3	Euclidean distance error - Tool Pose	49
5.4	Repeatability M3 fiducial marker at 30cm	50
5.5	Repeatability M4 fiducial marker at 30cm	50
5.6	Repeatability M8 fiducial marker at 30cm	51
5.7	Repeatability M9 fiducial marker at 30cm	51
5.8	Repeatability M3 fiducial marker at 40cm	52
5.9	Repeatability M4 fiducial marker at 40cm	52
5.10	Repeatability M8 fiducial marker at 40cm	53
5.11	Repeatability M9 fiducial marker at 40cm	53
5.12	Repeatability M3 fiducial marker at 50cm	54
5.13	Repeatability M4 fiducial marker at 50cm	54
5.14	Repeatability M8 fiducial marker at 50cm	55
5.15	Repeatability M9 fiducial marker at 50cm	55
5.16	Repeatability M3 fiducial marker at 60cm	56
5.17	Repeatability M4 fiducial marker at 60cm	56
5.18	Repeatability M8 fiducial marker at 60cm	57
5.19	Repeatability M9 fiducial marker at 60cm	57
5.20	Mean differences distances between fiducial points (N=88)	58
5.21	Mean distance differences between fiducial points (N=88)	59

5.22	Comparison between Calibre and Automatic Distance Acquisition. 4 distance for target:manual measurement N=168; automatic mea- surement N=168	60
5.23	Difference between Calibre and Automatic Distance Acquisition. (N=42 for each box plot)	61
5.24	Calibre Acquisition (N=14 for each distance)	62
5.25	Automatic Acquisition (N=14 for each distance)	63
5.26	Duration by Phase with Individual Data Points (Phase 0 (N=33); Phase 1 (N=23);Phase 2 (N= 6))	65
5.27	Radiation Picuter Counts. (Phase 0 (N=33) Phase 1 (N=23); Phase 2 (N= 6))	66
5.28	k-Wires implanted distance from Brachial Artery (Phase 0 (N=33); Phase 1 (N=23); Phase 2 (N= 6))	67
5.29	k-Wires implanted distance from Median Nerve(Phase 0 (N=33); Phase 1 (N=23); Phase 2 (N=6))	69
5.30	k-Wires implanted distance from Ulnar Nerve (Phase 0 (N=33) Phase 1 (N=23); Phase 2 (N= 6))	71
6.1	Augmented Reality Environment from HMD	73
6.2	QR code for phantom and guide tracking and related features. . . .	74
6.3	QR tracking and models superimposition	74
6.4	Communication Interface for coordinates extimation with Hololens IR Camera	75
6.5	Realsense Depth Camera and Kinect Spherical Marker Acquisition comparison	76
6.6	Assessing circle detection algorithms during surgery	77
6.7	Assessing circle detection algorithms during surgery	78
6.8	Center Circle Coordinates in Circle Detection - Hough and MSER .	78
6.9	Application of the Optimal Transport Theorem between two sets of points. The cost matrix used to calculate the transport plan is shown on the right.	79
6.10	Test Set - First Training	83
6.11	Test Set - Second Training	84
6.12	Test Set - Third Training	84
6.13	Frames and Sphere IR segmentation	85
6.14	Points triangulation in Space	85

Acronyms

AR

Augmented Reality

AMCW

Amplitude Modulated Continuous Wave

ASTM

American Society for Testing and Materials

CAS

Computer Aided Surgery

IGS

Image Guided Surgery

MIS

Minimally invasive surgery

OTS

Optical tracking systems

OTS

Near Infrared Optical Tracking System

ToF

Time of Flight

MRI

Magnetic Resonance Imaging

US

Ultrasound

CAD

Computer-Aided Design

CNN

Convolutional Neural Networks

TCP

Transmission Control Protocol

UDP

User Datagram Protocol

FOV

Field of View

SDK

Software Development Kit

PLA

Polylactic Acid

IR

Infrared

RGB

Red, Green, Blue

AI

Artificial Intelligence

HMD

Head-Mounted Display

UI

User Interface

Chapter 1

Introduction

Iatrogenic peripheral nerve injuries account for up to 20% of traumatic nerve lesions. The majority of these incidents occur in the aftermath of orthopedic surgeries, given the nature of procedures conducted on upper and lower extremities [1, 2]. These injuries are subdivided in two broad categories:

- **Direct injuries** encompass nerve lacerations during dissection and harm caused by the insertion or removal of implants, screws and k-wires [3].
- **Indirect injuries** arise from stretch, compression, or thermal factors [3, 4].

Image-guided surgery and augmented reality lend to the reduction of iatrogenic nerve damage, especially in the case of direct damage. Furthermore reduce the need for X-rays, which are harmful to the patient, operators and bystanders.

1.1 Iatrogenic peripheral nerve injuries

1.1.1 Nerve Anatomy

The structure of a peripheral nerve comprises *axons* and *perineural Schwann cells* enclosed within a *connective tissue matrix*.

Axons, whether myelinated or unmyelinated, are organized somatotopically into units known as fascicles within a peripheral nerve. The connective tissue framework of the nerve consists of endoneurium, enveloping individual axon fibers within fascicles, perineurium surrounding individual fascicles, and an epineurium that encircles groups of fascicles, forming the external sheath of the nerve. Within this connective tissue framework, a vascular supply nourishes the nerve.[5].

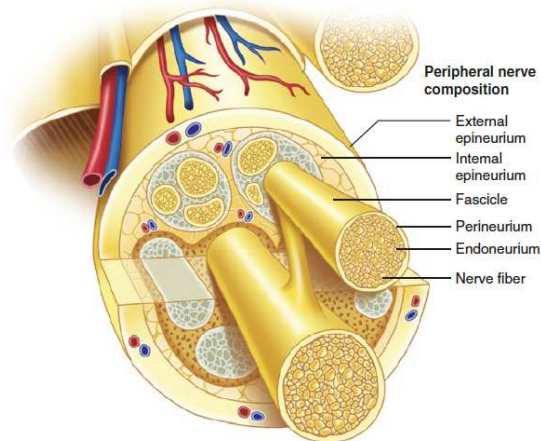


Figure 1.1: Peripheral nerve architecture

Peripheral nerves are endowed with an interconnected network of extrinsic and intrinsic blood vessels. Extrinsic blood vessels follow the longitudinal path of the nerve along the outer surface of the epineurium, providing nourishment to the intrinsic system at various points along the nerve [6, 7].

1.1.2 Categorization of Nerve Lesions

Seddon introduced a classification system that categorizes damaged nerves into three overarching types: *neurapraxia*, *axonotmesis* and *neurotmesis* [8].

- **Neurapraxia:** Temporary interruption of conduction without loss of axonal continuity.
- **Axonotmesis:** Damage to the axon and its myelin sheath, but with preservation of the connective tissue framework of the nerve.
- **Neurotmesis:** Complete transection of a peripheral nerve, leading to the rupture of the axon, myelin sheath, and connective tissues. Poor prognosis for spontaneous recovery without surgical intervention.

Sunderland introduced a more detailed classification system aimed at aligning varying degrees of injury with the underlying pathology. This classification spans from Grade 1, signifying a temporary alteration in nerve function, to Grade 5, indicating complete severance of the nerve. Sunderland's classification establishes a correlation between escalating levels of dysfunction and the extent of damage to the internal architecture of the nerve [9].

1.1.3 Identification of Injuries and Surgery Management

In the case of iatrogenic nerve injuries following surgery, it may be prudent to contemplate prompt re-operation if there is a substantial suspicion of injury beyond Grade 1 or 2. When nerve injuries are identified during the surgery, primary repair should be undertaken or within 3–4 weeks if the zone of injury remains uncertain. Likewise, if postoperative ultrasound (US) or magnetic resonance imaging (MRI) reveals indications of transection or neuroma in continuity, surgery should be conducted without significant delay [10].

1.2 Nerve Injuries Post Orthopedic Elbow Surgery

Nerve injuries during elbow arthroscopy have been documented in approximately 2.5% of cases [11]. Several factors can increase the risk of nerve injuries during elbow arthroscopy; these include patient factors, surgical history, medical conditions, anatomical considerations, surgical technique and experience [12, 13].

1.2.1 Elbow Anatomy

The elbow is a synovial joint formed by the interactions of the humerus, radius, and ulna. Classified as a trochoginglymus joint, it comprises three articulations (ulnohumeral, radiocapitellar, and proximal radioulnar joints) and allows for two degrees of freedom, enabling flexion/extension and pronation/supination [14].

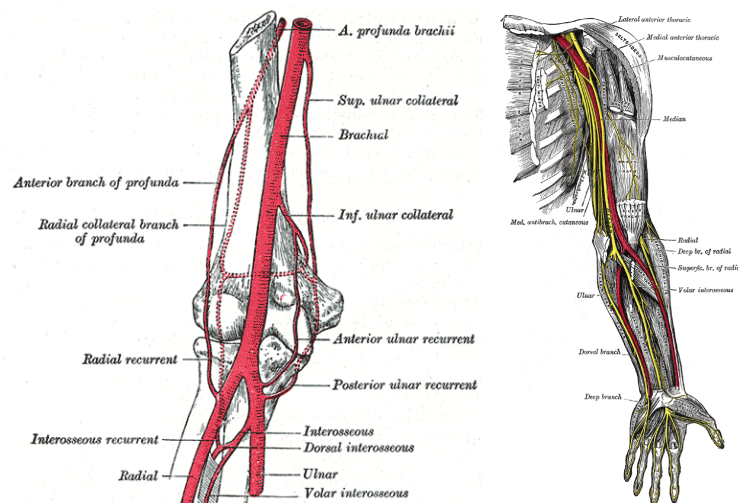


Figure 1.2: Vascularization (left) and Innervation (right) of the elbow.

Nerve structures

The innervation of the elbow joint encompasses the radial, ulnar, and median nerves, primarily providing innervation to structures in the forearm and hand [15].

The *radial nerve* innervates muscles influencing the elbow joint, such as the brachialis, anconeus, supinator muscle, brachioradialis, and triceps brachii. The *ulnar nerve* controls muscles in the forearm and hand, while the *median nerve* passes anteriorly through the elbow joint, extending to innervate the forearm and hand further downstream.

Vascular Structures

The vascular anatomy of the elbow comprises an intricate anastomosis of vessels, including the *radial* and *ulnar collateral arteries* and the *radial and ulnar recurrent arteries*. These structures play a crucial role in providing the necessary blood supply to the elbow joint [16].

1.2.2 Injuries mechanisms, incidence and risk factors

The most common mechanisms of nerve injury are compression and traction; but nerve laceration or complete transection occurs as a result of the surgical procedures.

Mechanisms of nerve injuries

There are four main mechanisms of nerve injuries [17]:

1. **Nerve Compression:** Occurs when a nerve is subjected to excessive pressure, often due to surrounding structures or anatomical features.
2. **Nerve Traction:** Involves the stretching or pulling of a nerve beyond its normal range, potentially leading to damage.
3. **Nerve Laceration:** Results from a sharp cut or injury to the nerve, causing physical damage to its structure.
4. **Nerve Transection:** Refers to the complete severing of a nerve, leading to a complete interruption of its continuity.

Incidence and risk factors

Iatrogenic nerve injuries can occur during the insertion of K-wires and screws in orthopedic procedures. Several studies have reported on the complications associated with these procedures.

A review of K-wire related complications in the emergency management of pediatric upper extremity trauma found 3.8% of cases resulted in iatrogenic nerve injuries, with factors such as pin placement and patient compliance contributing to the complications [18]. Another study on the risks of Kirschner wire placement in the distal radius compared percutaneous and limited open insertion techniques to determine the associated risks [19]. Additionally, a study on risk factors for screw breach and iatrogenic nerve injury in percutaneous posterior pelvic ring fixation reported a 3.2% rate of iatrogenic nerve injuries [20]. Furthermore, a guide to the management of iatrogenic peripheral nerve injuries in orthopedic surgery highlighted the various mechanisms through which these injuries can occur, including the insertion and removal of K-wires and metalwork [21].

Focus on Elbow

Iatrogenic nerve injuries, particularly *ulnar nerve injuries*, can occur during the insertion of K-wires in the elbow. The ulnar nerve is at risk of damage from K-wire insertion, leading to complications such as *ulnar nerve palsy* [18]. This can result from direct ulnar nerve damage, compression from the K-wire causing cubital tunnel syndrome, or the ulnar nerve being caught in the fracture site, especially in flexion-type injuries [22]. Direct visualization of the ulnar nerve during the insertion and removal of K-wires is recommended to minimize the risk of iatrogenic nerve injuries [21]. The ulnar nerve is particularly vulnerable at the elbow, and its injury can lead to specific motor and sensory deficits.

1.2.3 Prevention Strategies

Implementing various preventive measures can significantly reduce the risk of nerve injuries. Blonna et al. have succinctly outlined these strategies in 10 key points [23]: (1) adhere to a learning curve that aligns with operator skill level; (2) possess a clear understanding of nerve locations; (3) employ retractors; (4) minimize swelling according to provided recommendations; (5) disconnect suction from the shaver; (6) exercise caution with burrs in proximity to the ulnar nerve near the medial gutter; (7) adjust your grip on the burr to enhance instrument control; (8) adopt a consistent step-wise technique; (9) collaborate with an experienced assistant; and (10) proactively anticipate and mitigate potential challenges.

The objective of this thesis is to add to prevention methodologies, the use of image-guided surgery systems and reality augmentation as a strategy to prevent iatrogenic damage and improve surgical outcome

1.3 Image-guided surgery and Augmented Reality

Image-guided surgery (IGS) involves the use of preoperative or intraoperative imaging to guide surgical procedures, employing real-time tracking of surgical instruments displayed in multiplanar views relative to the patient’s anatomy enabling precise positioning of instruments and implant placement particularly useful when dealing with unexposed or partially exposed anatomy. The technology enhances surgical accuracy, boosting surgeons’ confidence, ensuring patient safety and gives valuable information during the surgery[24].

Minimally invasive surgery (MIS) leads to better postoperative results and faster healing compared to traditional open surgery. In MIS, image-guided techniques are essential because viewing human anatomy relies on medical imaging. However, MIS encounters challenges, including navigating surgical information on a 2D screen, which complicates hand-eye coordination and reduces depth perception. Augmented reality (AR) has been utilized to address this issue [25].

1.3.1 Intraoperative image-guided surgery systems

Many surgeons still perform surgeries without the aid of guidance systems or rely on traditional fluoroscopy technologies. This approach results in a considerable percentage of screws deviating from their intended trajectory, ranging from 12% to 40% in screw placements [26, 27]. Such deviations pose risks of acute neurovascular injury and, over the long term, mechanical construct failure, necessitating potentially expensive revision surgeries [28, 29]. To address this issue, Image-Guided Surgery (IGS) allows surgeons to visualize unexposed or partially exposed structures, such as the pedicle region of a vertebra. This visual guidance helps prevent potential damage to sensitive nearby organs, including the spinal cord, nerves, and vascular structures. IGS has significantly improved the precision of screw placement across all levels of the spine, resulting in breach rates reduced to under 10% [30, 31, 32].

Fluoroscopy-integrated image-guided surgery (IGS) systems merge *computer-assisted surgical technology* with *C-arm fluoroscopy* [33, 34]. They typically share common elements:

- a C-arm fluoroscope positioned in the operating room.
- a calibration target affixed to the C-arm.
- a reference array.

- a tracking system.
- tailored surgical instruments like screwdrivers, awls, probes and pointers.

The tracking system monitors the reference array and surgical tools in real-time, making them visible during the procedure.

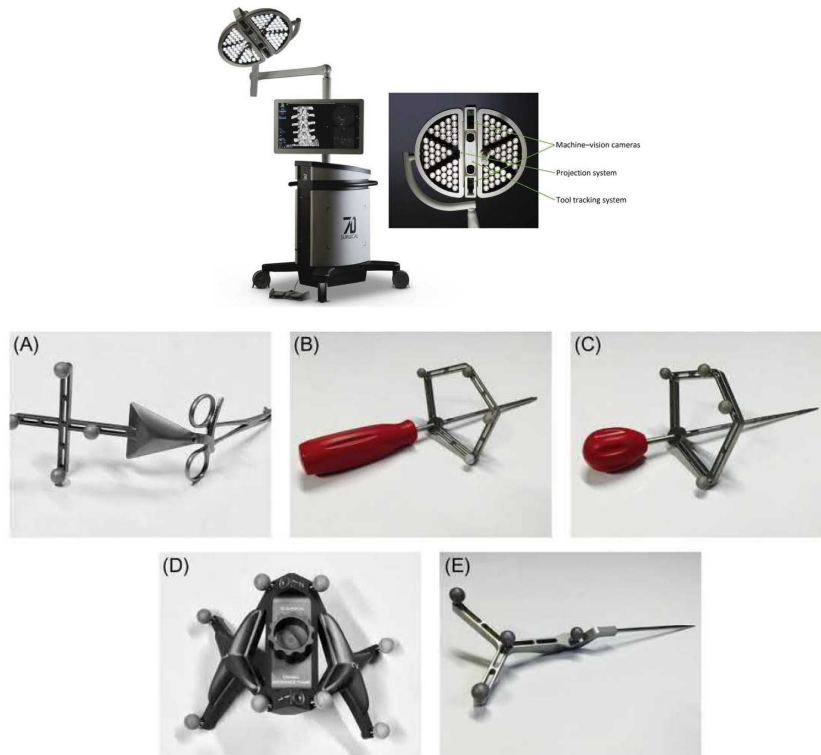


Figure 1.3: 7D Surgical MvIGS system (left) and 7D Surgical’s trackable surgical tools (right)

Comparison between Systems

Conventional fluoroscopy offers an intraoperative visualization of anatomy but presents drawbacks, such as significant exposure to ionizing radiation for patients, surgical staff, and surgeons. Additionally, this method allows imaging in only one plane at a time. In contrast, virtual fluoroscopy minimizes the necessity for frequent C-arm repositioning by utilizing multiple pre-saved images and works as a multiplanar imaging unit. In a 3D intraoperative image-guided surgery systems the 3D intraoperative imaging equipment is integrated into the IGS system through a calibration process, allowing the 3D image volume to have a precise location noted by the tool tracking system [35].

1.3.2 Augmented Reality

Augmented reality (AR) merges real-world images and virtual information in real time. In the intraoperative stage, AR-technologies have the potential to boost surgical precision and offer a more comfortable setting for the surgeon. This includes the integration of information gathered before surgery and the surgical strategy with real-time visualization of the operation area [36, 37]. Digital contents is overlaid onto the surgeon’s operating field view, to obtain a composite view of the patient, superimposing virtual information onto the real-world environment [38].

Augmented reality (AR) can assist in minimally invasive surgery (MIS) and robotic minimally invasive surgery (RMIS), where the tactile sense to detect key anatomical features is lost, by providing real-time visualization of crucial structures. This contributes to reducing the duration of the surgical procedure [39].

This technology has been increasingly reported in various orthopedic applications, including spine, osteotomies, arthroplasty, trauma, and orthopedic oncology. The literature highlights its potential for higher accuracy in surgical execution, reduction of radiation exposure, and decreased surgery time [40].

Registration

The process of adjusting a virtual 3D model to accurately reflect the patient’s anatomy is known as *registration*. It is essential for establishing an AR setting and the instrumentation for intraoperative guidance. Through the application of modular virtual transparency, AR enhances the visibility of target structures and the understanding of anatomical relationships, allowing for the inspection of internal areas within closed cavities or through solid materials [41, 42].

The process of registration is characterized by a mathematical function known as transformation, which may be classified as either rigid or deformable.

1. *Rigid registration* involves a transformation defined by six degrees of freedom (three for rotation and three for translation) under the assumption that the scene remains unchanging in shape [43, 44]. The Iterative Closest Point is the most commonly employed algorithm for rigid registration.
2. *Deformable registration* is characterized by a transformation that ranges from six to an infinite number of degrees of freedom. The aim is to reflect the deformation model complexity. A widely recognized approach to deformable transformations employs the concept of vector fields [45, 46, 47].

Visualization

The choice of AR technique varies according to the surgical setup. It depends on operation area visualization: direct observation, microscope assistance or endoscopic imaging.

- *Projection on patient.* It involves displaying images directly on the patient's body, effective for 2D elements like insertion points or surface markers
- *Optical see-through.* It enables AR data to be displayed on semitransparent surfaces, merging virtual information with the actual scene. This projection can be fixed in front of the scene or integrated into wearable technology.
- *Video see-through.* It allows to overlaid AR content on a live surgery video captured by a camera.
- *Static video display.* It represents AR information in surgical scenario video streamed and display it on a statically mounted display.

In the field of surgery, augmented reality (AR) systems utilizing 3D images primarily fall into two main categories: binocular-based 3D AR systems and 3D autostereoscopic AR systems [48, 49].

- *Binocular-based 3D AR systems:* using supplementary instruments (eg. HMD and AR surgical microscopes) two images with parallax are provided to reconstructs 3D scene simulating binocular vision;
- *3D autostereoscopic AR systems* provide glasses-free 3D visualization . Through parallax barrier and lenticular methods are delivered 3D medical images with only one parallax.

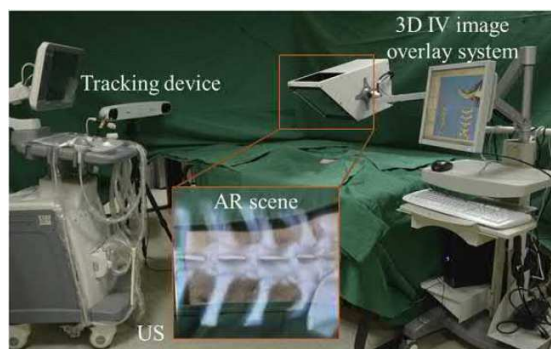


Figure 1.4: 3D IV image overlay in spine surgery

1.3.3 Accuracy evaluation International Standard

Establishing norms and standards in the biomedical field is crucial for ensuring the accuracy and safety of medical devices. Norms provide a framework for evaluating device performance, maintaining consistency, and ensuring quality. Standardization also promotes interoperability among devices, crucial in modern healthcare systems. The ASTM F2554-10 standard is utilized in the literature to assess accuracy performance of CAS System [35].

ASTM F2554-10 standard [50]

The ASTM F2554-10 standard, titled "Standard Practice for Measurement of Positional Accuracy of Computer-Assisted Surgery Systems," provides guidelines for measuring and reporting the accuracy of surgical systems. It ensures that computer-assisted surgery systems meet required performance standards.

Evaluate parameters, considering the system's features:

1. Point location in relation to a coordinate system.
2. Accuracy between points (linear).
3. Repeatability of a single point's coordinates.
4. For optical systems, the visible range of reference frame or tool orientations.
5. This method encompasses all configurations of tool arrays in the system.

To evaluate the mentioned parameters, an example of a phantom reported in the standard is shown in Figure 1.5.

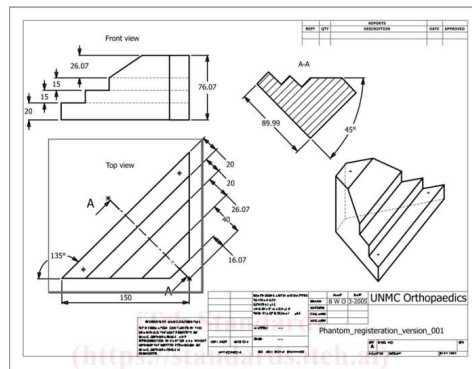


Figure 1.5: Blueprint Phantom in ASTM F2554-10

Chapter 2

Tracking System Development

The following chapter explains the development of the tracking system. Firstly, the setup used is shown, as well as the hardware part of the system and its technical specifications. In succession, the workflow software will be illustrated.

2.1 Tracking systems overview

Various methods are available for determining the pose of an object in space. Typically, a tracking system hardware includes three main components [51]:

- signal-generating sources;
- sensors for receiving the signal;
- a system for data acquisition and signal processing.

Mechanical, acoustic, inertial, magnetic, and radio frequency tracking systems have been utilized previously. However, similar to optical tracking, used in this framework, each approach comes with its own set of strengths and limitations [52]. Optical tracking systems (OTS), that use cameras to locate markers in a fixed arrangement, are widely used in clinical settings. Near Infrared Optical Tracking Systems (NIOTS) operate at near-infrared wavelengths to counter the effects of environmental light. Its frameworks entails markers (active or passive) recognition attached to anatomical structures or instruments.

2.2 Experimental Setup

The experimental setup can be briefly described as follows. The Kinect Azure DK is the acquisition data source. The depth map provided is processed for tracking tools position calculation, based on markers recognition. The position acquired is virtualised on a software developed on Unity® and used to provide information useful for the correct positioning of elements in target positions. In this configuration (Figure 2.1), the tool tracking is positioned on the drill to simulate the k-wire insertion into the elbow dummy.



Figure 2.1: Experimental Setup

2.2.1 Acquisition System (Kinect Azure DK)[53]

The Microsoft Azure Kinect DK is a developer kit that provides AI sensors for computer vision and spatial tracking. It includes a 12-MP RGB video camera, a 1MP depth camera, a 360° microphone array and an orientation sensor.

Depth Camera Features

The 1-Megapixel Time-of-Flight (ToF) depth camera employs the *Amplitude Modulated Continuous Wave (AMCW) principle*. It projects modulated near-infrared (NIR) illumination onto the scene to capture depth information. The depth camera has two NIR laser diodes for near and wide field-of-view depth modes. With the world's smallest ToF pixel, it automatically adjusts the per-pixel gain for a broad dynamic range. The global shutter improves performance in sunlight, and a multi-phase depth calculation method ensures accuracy despite variations in chip,

laser and power supply. The depth camera's performance is evaluated in terms of systematic and random errors. The typical systematic error, excluding multi-path interference, is less than $11 \text{ mm} + 0.1\%$ of the distance [54].

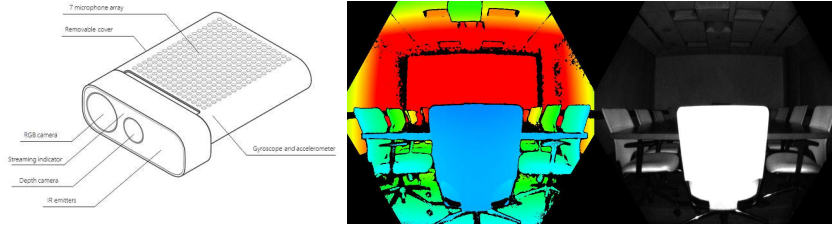


Figure 2.2: Representation of Kinect Azure DK with color and infrared images captured by the device

Amplitude Modulated Continuous Wave (AMCW) principle

The Amplitude Modulated Continuous Wave (AMCW) principle involves varying the amplitude of a continuous wave to measure the time of flight (TOF) for distance determination through phase modulation of continuous wave [55].

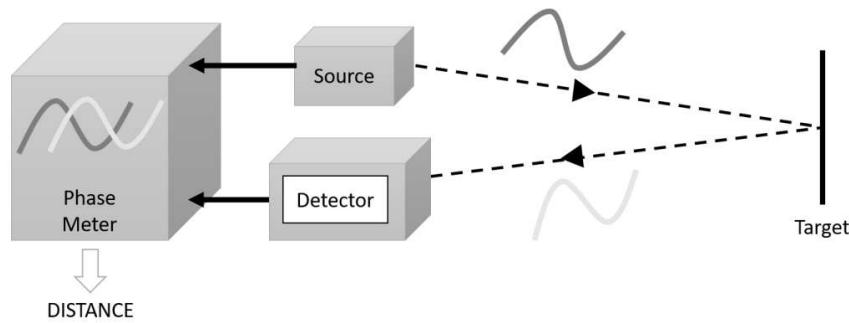


Figure 2.3: TOF phase-measurement principle in AMCW sensors [55].

The optical power undergoes modulation at a constant frequency, usually a few tenths of MHz, resulting in an emitted beam with a sinusoidal or square wave pattern at the same frequency. After reflection from the target, a detector collects the received light signal. Measurement of the distance R is deduced from the phase shift $\Delta\Phi$ occurring between the reflected and emitted signals, according the equation [55]:

$$\Delta\Phi = k_M d = \frac{2\pi f_M}{c} 2R \Rightarrow R = \frac{c}{2} \frac{\Delta\Phi}{2\pi f_M} \quad (2.1)$$

with:

- R : distance to the target,
- c : speed of light in free space,
- kM : wavenumber related to modulation frequency,
- d : total distance traveled,
- fM : modulation frequency of signal amplitude.

Depth Camera Modes and Coordinate System

The Azure Kinect DK depth camera encompasses NFOV (Narrow Field of View) and WFOV (Wide Field of View) modes. Furthermore, supports 2x2 binning modes to increase the Z-range compared to the corresponding unbinned modes at the expense of reduced image resolution. The available modes and resolutions are:

- **NFOV Unbinned** at 640x576;
- **NFOV 2x2 Binned** at 320x288;
- **WFOV Unbinned** at 1024x1024;
- **WFOV 2x2 Binned** at 512x512.

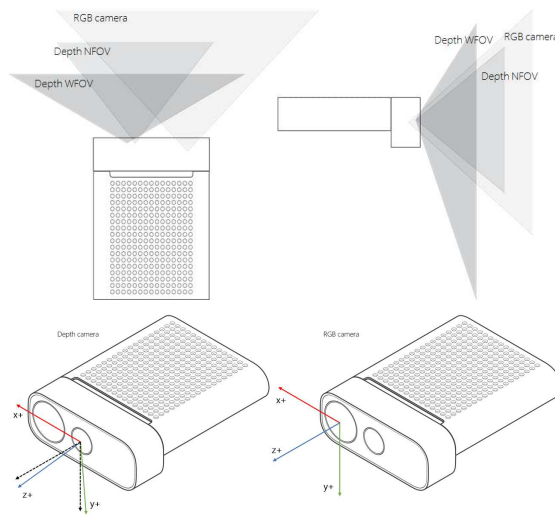


Figure 2.4: Kinect FOV and Coordinate System

The camera's focal point serves as the origin $[0, 0, 0]$. The coordinate system is set with the positive X-axis pointing right, the positive Y-axis pointing down, and the positive Z-axis pointing forward.

2.2.2 Tracking Tools

The tracking tools are inspired by existing surgical navigations systems (eg. Medtronic® StealthStation and Brainlab® VectorVision), and adapted for a Bosch® commercial drill. These were designed with Autodesk® Fusion 360 and 3D printed with the Raise3D® Pro2 3D printer.

For the tracking system developed tools are:

- the *guide integral* to the drill;
- the *support stand* for the dummy.

Both elements are equipped with four IR reflecting spheres (passive markers).

Drill Guide

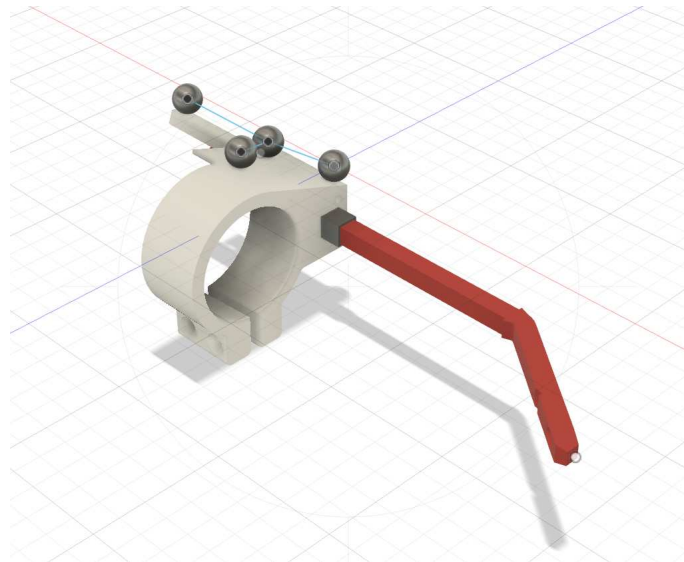


Figure 2.5: Drill Guide for k-Wires insetion

The drill guide (Figure 2.5) comprises two key components:

- the **circular clamp**: fixed to the drill ring and hosts the passive markers;
- the **mobile arm**: to stabilize the k-Wire, ensuring the accurate positioning of the drill in relation to the rest of the system.

Support Stand

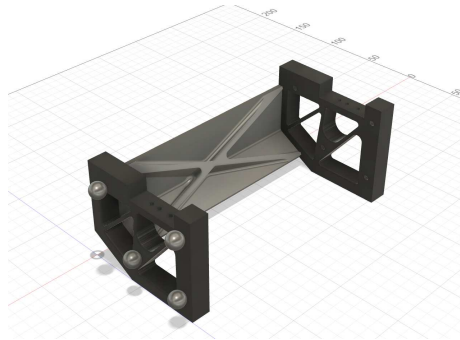


Figure 2.6: Stand for Dummy

The stand ensures stable support to the dummy. Passive markers, placed at known points from the digital model, establish a connection between the digital representation of the elbow —comprising bones, nerves, and vascular structures— and the 3D-printed and silicone-molded replica. The stand has the same function of the reference array of typical image guided surgery systems, where it is attached to the patient ensuring accurate registration of their position.

Passive Markers

NDI (Northern Digital Inc.) passive spheres are one-time-use, sterile, disposable reflective markers (FDA-regulated medical devices) used in image-guided surgery (IGS) systems. They have a retro-reflective surface composed by tens of thousands of microbeads for reflect IR light during tracking [56].

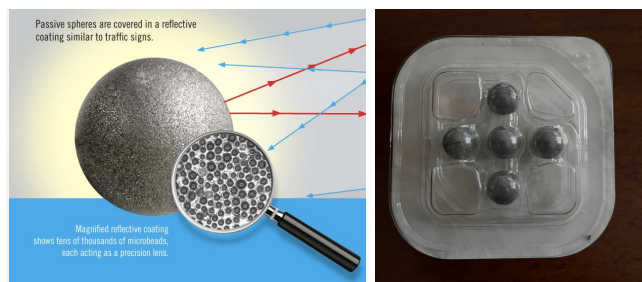


Figure 2.7: NDI spherical markers

2.2.3 Simulation Elbow Phantom

The anatomical model of the elbow was created from the Open Source anatomical atlas Z-Anatomy. To implement the design of the tracking tools with the anatomical model, the components of interest were exported from Blender and imported into Autodesk Fusion 360 in .fbx format.

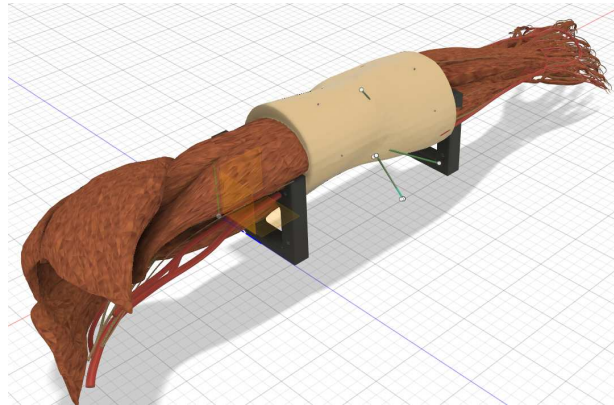


Figure 2.8: Complete model of the elbow including, muscles, nerves, vessels, bones and skin.

The vascular and nerve components are only present in the digital model. Their damage is studied in relation to target points positioned on the dummy.

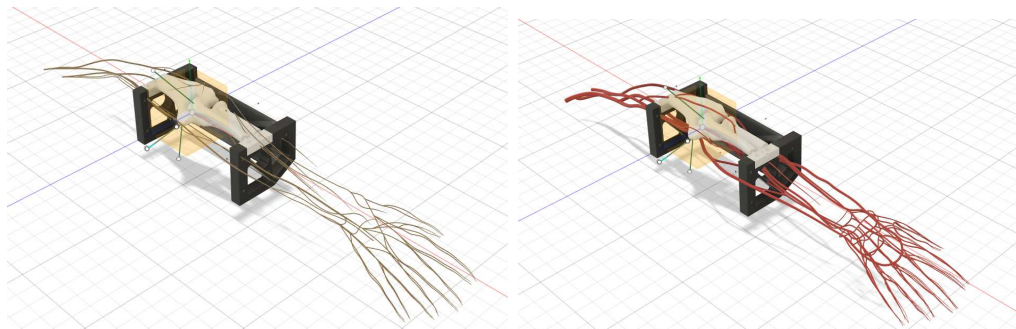


Figure 2.9: On the left are shown the nerves, on the right the vascular structures in the virtual model

In order to reproduce the digital model in a physical model, a mould complementary to the elbow shape was created, within which the 3D-printed PLA sections of radius, ulna and humerus were positioned opportunely.

2.3 Acquisition Data Software framework

The software framework works as follows: Kinect captures images, sending them to Python through a USB-C interface. In Python, the marker positions on the guide and the reference frame are determined. Using a TCP/UDP interface, this marker data is then sent to a Unity program, facilitating guided implantation of k-wires in the dummy.



2.3.1 Raw Data

The data is acquired using the Kinect platform, transmitted to the PC through a USB 3.0 interface and then transferred to Python using the pyk4a library. The received images are represented as numpy arrays, functioning like standard Python objects [57]. For this purpose, the depth camera is configured in WFOV 2X2BINNED mode, with an image resolution of 512x512 as uint16 data. Therefore, each pixel can represent values ranging from 0 to 65'535.



Figure 2.10: Raw Image from IR camera. On the right image with enhanced contrast

2.3.2 Segment Detection and Rejection

The acquired IR image is in uint16 format, with variable values ranging from 0 to 65355. A thresholding is applied to select pixels corresponding to the reflective markers. Threshold values are set between 1000 and 12000, and values outside this range are set to 0.

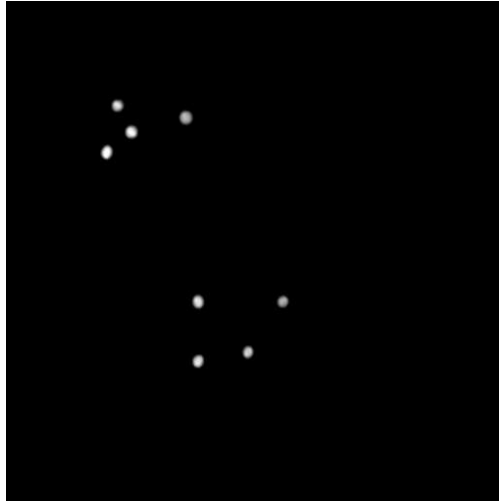


Figure 2.11: Thresholded Image

Hough transform is implemented from OpenCV library's ('cv.HoughCircles()'). In output is obtained a mask of spherical markers.

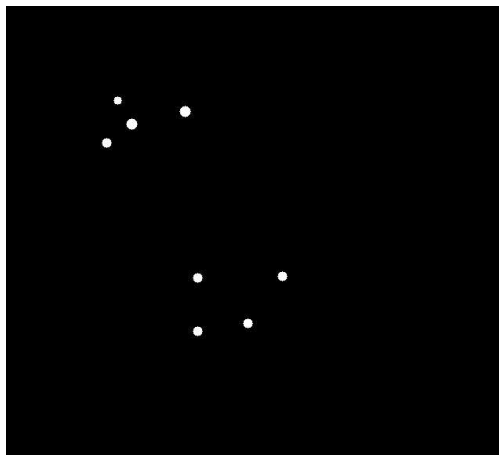


Figure 2.12: Hough Circle Transformation: Circle Mask (OpenCV)

Hough Transformation

The Hough Circle Transform is a technique in digital image processing that creates an accumulator for circle parameters. "Voting" in *Hough parameter space* circles are detected [58]. In 2D space, a circle is described by its center coordinates and radius, expressed by the equation:

$$(x - a)^2 + (y - b)^2 = r^2 \quad (2.2)$$

where:

- (x, y) are the coordinates of the point in the image,
- (a, b) are the coordinates of the circle's center,
- r is the radius of the circle.

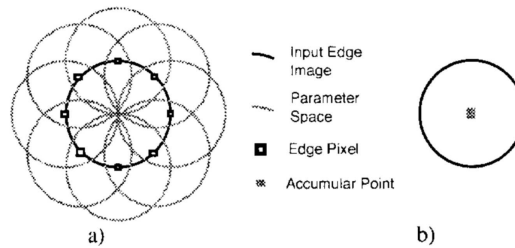


Figure 2.13: a) Edge points contribute to the accumulator space; b) Edge points contribute to a single point in the accumulator.

Applying the Hough Circle Transform, accumulators are created in the parameter space (a, b, r) for each potential center (a, b) and radius r . The concept is to vote for all potential circles in the image, finding maxima in the accumulators that indicate the centers and radii of the most likely circles. A threshold can then be applied to decide which circles should be detected [59].

2.3.3 Centroid Detection

From IR images Kinect computes the correspondent Point Cloud. Each pixel in the image associated to 3D coordinates in camera space. Using the Hough transform's a mask is applied to isolate the 3D points associated with the spheres. Thus, the centroid of each sphere is calculated from the average of the coordinates of the points associated with the surface.

$$x_{\text{avg}} = \frac{1}{N} \sum_{i=1}^N x_i \quad (2.3)$$

$$y_{\text{avg}} = \frac{1}{N} \sum_{i=1}^N y_i \quad (2.4)$$

$$z_{\text{avg}} = \frac{1}{N} \sum_{i=1}^N z_i \quad (2.5)$$

The coordinates of each sphere are represented by $[x_{\text{ave}}, y_{\text{ave}}, z_{\text{ave}}]$. The matching algorithm is supplied with an array where each row contains the coordinates of the four spheres identifying a tracking tool.

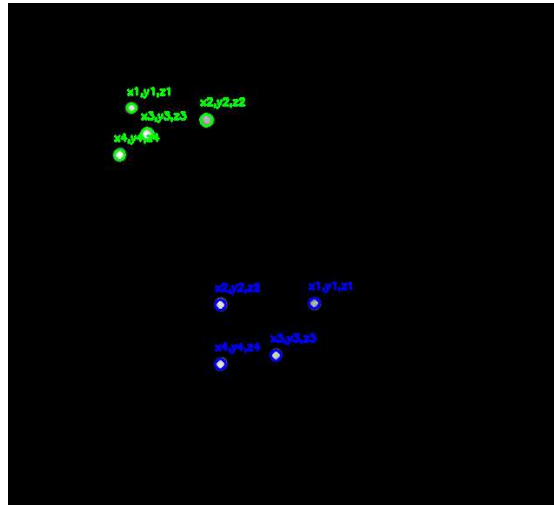


Figure 2.14: sphere labeled with coordinates x_i, y_i, z_i

$$\text{marker_position}_{\text{ave}} = \begin{bmatrix} x_1 & y_1 & z_1 \\ x_2 & y_2 & z_2 \\ x_3 & y_3 & z_3 \\ x_4 & y_4 & z_4 \end{bmatrix} \quad (2.6)$$

2.3.4 Point Correspondence

The objects pose identification requires aligning spatial markers with model markers. Various methods, such as linear sum assignment, optimal transport, and Procrustes analysis, were compared. The Procrustes analysis proved to be the most suitable for the task.

Procrustes analysis [60]

Procrustes analysis is a statistical method used for comparing shapes. It entails identifying the optimal transformation to minimize the differences between two shapes. There are two primary types: ordinary Procrustes analysis, which compares two shapes, and generalized Procrustes analysis (GPA), which is used for superimposing a population of shapes. For this thesis the Ordinary Procrustes analysis is used. The formulation can be expressed mathematically as follows.

The purpose is to find a transformation T that minimizes the sum of squared differences between corresponding points in the two sets:

- the reference shape or configuration: $X = \{x_1, x_2, \dots, x_n\}$
- the shape to be aligned or compared: $Y = \{y_1, y_2, \dots, y_n\}$

The Procrustes cost function D is given by:

$$D(X, Y) = \min_T \sum_{i=1}^n \|T(x_i) - y_i\|^2$$

with:

- $T(x_i)$ represents the transformed point x_i after applying the Procrustes transformation T .
- $\|\cdot\|$ denotes the Euclidean norm.

The transformation can be decomposed into translation, rotation, and scaling components. For two-dimensional data, the transformation T can be expressed as a combination of rotation matrix R , scaling factor s , and translation vector c :

$$T(x_i) = s \cdot R \cdot x_i + c$$

The Procrustes analysis typically involves solving for the rotation matrix R , scaling factor s and translation vector c that minimize the cost function D .

Method Application

The Procrustes method solves the correspondence between acquired markers and those of a tracking tool model. The 3D positions of the markers on the tracking tool are acquired through the User Interface. These coordinates require initial manual reordering for visual comparison with the pre-established model. Essentially, at least one frame requires manual labeling, which then allows automatic labeling for each frame.

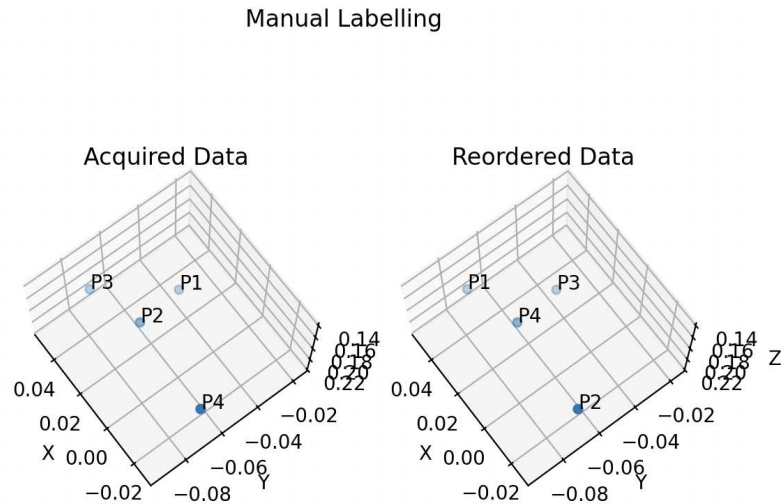


Figure 2.15: Marker Labelling for Guide Tracking Tool

Each frame has four markers, resulting in 24 permutations. To each the analysis is performed with `scipy.spatial`.

```
1 mtx1, mtx2, disparity = procrustes(points_model, points_frame)
```

The function returns:

- the orientation of `points_frame` that optimally aligns with `points_model`;
- the sum of squared pointwise differences between the two datasets:

$$M^2 = \sum_{i=1}^n (\text{points_frame} - \text{points_model})^2 \quad (2.7)$$

The best-fitting permutation for `model_point` minimizes the sum of squared distances across all permutations. The result of applying this method can be seen in the figure 2.16

Procrustes Analysis for a Frame Set Point

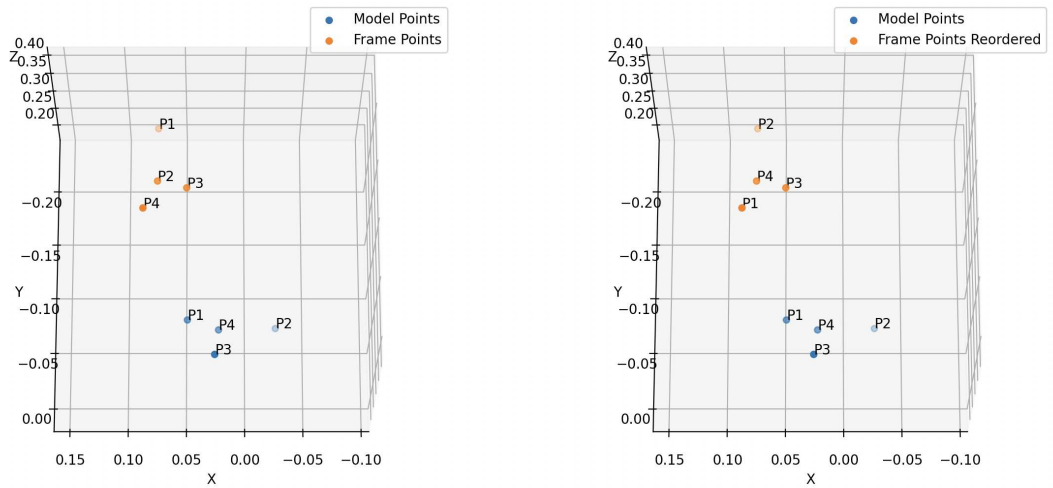
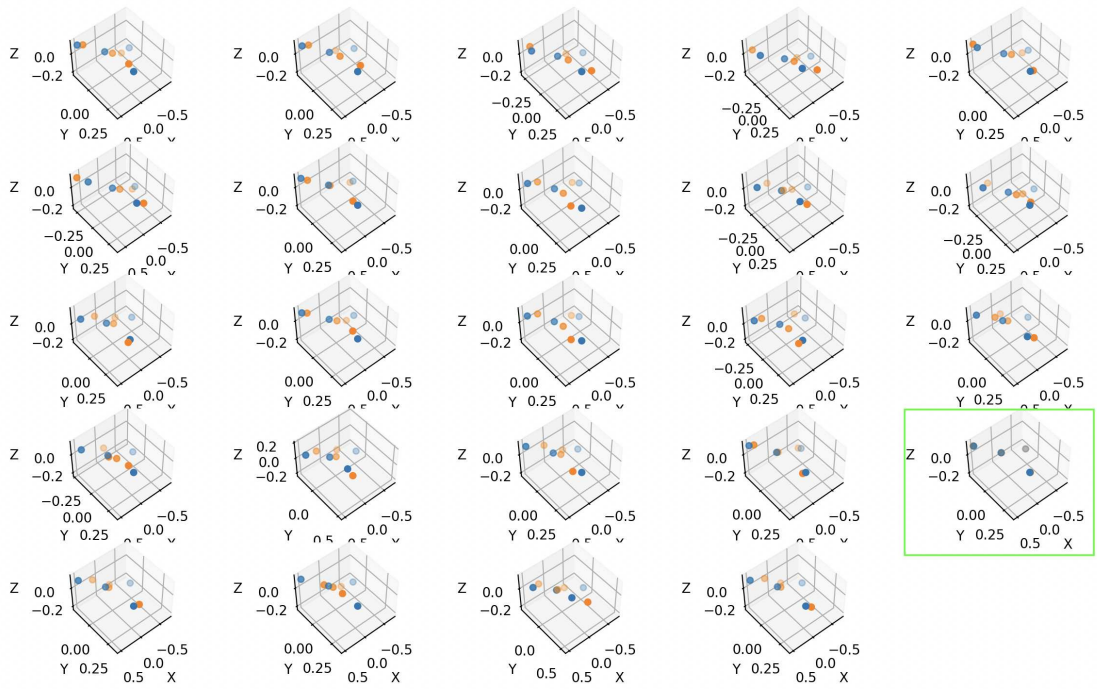


Figure 2.16: Procrustes Analysis

2.3.5 Data filtering

The Kalman filter estimates the internal state of a dynamic system using noisy measurements. It provides a more accurate real-time estimation by incorporating both current input measurements and past state information.

Kalman Filter Formulation [61]

For filtering 3D positions, the Kalman filter equations are formulated as follows.

- x_k represent the 3D position at time k :

$$x_k = \begin{bmatrix} x \\ y \\ z \\ \dot{x} \\ \dot{y} \\ \dot{z} \end{bmatrix}$$

- x , y , and z are the 3D coordinates;
- \dot{x} , \dot{y} , and \dot{z} are their velocities.

- The state *transition matrix* F and the *control input matrix* B , which depend on the system's dynamics, can be represented under a constant velocity model:

$$F = \begin{bmatrix} 1 & 0 & 0 & \Delta t & 0 & 0 \\ 0 & 1 & 0 & 0 & \Delta t & 0 \\ 0 & 0 & 1 & 0 & 0 & \Delta t \\ 0 & 0 & 0 & 1 & 0 & 0 \\ 0 & 0 & 0 & 0 & 1 & 0 \\ 0 & 0 & 0 & 0 & 0 & 1 \end{bmatrix} \quad B = \begin{bmatrix} \frac{\Delta t^2}{2} & 0 & 0 \\ 0 & \frac{\Delta t^2}{2} & 0 \\ 0 & 0 & \frac{\Delta t^2}{2} \\ \Delta t & 0 & 0 \\ 0 & \Delta t & 0 \\ 0 & 0 & \Delta t \end{bmatrix}$$

- The *measurement matrix* H is:

$$H = \begin{bmatrix} 1 & 0 & 0 & 0 & 0 & 0 \\ 0 & 1 & 0 & 0 & 0 & 0 \\ 0 & 0 & 1 & 0 & 0 & 0 \end{bmatrix}$$

In the Kalman filter's update and prediction phases are employed two critical parameters: (1) the *measurement noise covariance matrix* (R) and (2) the *process noise covariance matrix* (Q). R quantifies the uncertainty associated with measurements, representing how much noise is expected in the observations. On the other hand, Q assesses the uncertainty in the process model, indicating the expected variability in the dynamics of the system due to unmodeled inputs or environmental factors.

Application process:

1. Prediction Step:

$$\hat{x}_{k|k-1} = F\hat{x}_{k-1|k-1} + Bu_k$$

$$P_{k|k-1} = FP_{k-1|k-1}F^T + Q$$

2. Update Step:

$$K_k = P_{k|k-1}H^T(HP_{k|k-1}H^T + R)^{-1}$$

$$\hat{x}_{k|k} = \hat{x}_{k|k-1} + K_k(z_k - H\hat{x}_{k|k-1})$$

$$P_{k|k} = (I - K_kH)P_{k|k-1}$$

Where:

- $\hat{x}_{k|k-1}$ is the predicted state estimate.
- $P_{k|k-1}$ is the predicted error covariance.
- u_k is the control input.
- z_k is the measurement at time k .
- $\hat{x}_{k|k}$ is the updated state estimate.
- $P_{k|k}$ is the updated error covariance.
- K_k is the Kalman gain.

Kalman Filter Application

Figure 2.17 illustrates a comparison between unfiltered data and data filtered through Kalman filters, using the Filterpy library. These filters are configured with a state dimension of 6 and a measurement dimension of 3. The configuration includes a 6x6 identity matrix for the state transition (F), a 3x6 matrix for observation (H) to extract position data, and initial state (x) set to [0, 0, 0, 0, 0, 0]. Process covariance (P) is amplified by a factor of 10, while measurement noise covariance (R) is defined by a diagonal matrix with [1, 1, 1].

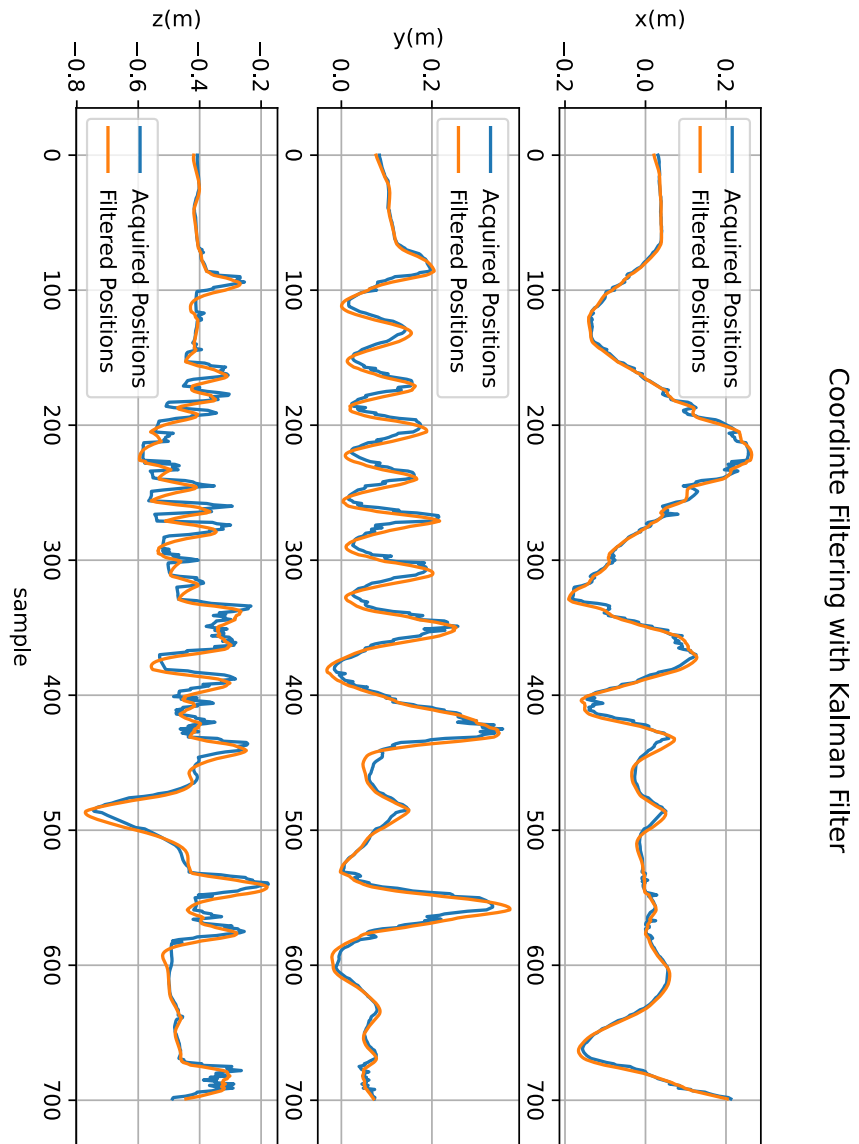


Figure 2.17: Filtered Marker Data with Kalman Filter

2.4 Acquisition Data Software UI and Communication Protocol

A user interface and a data communication system are crucial for the developed system. They enable user interaction and facilitate the integration of the algorithm with other software or systems.

2.4.1 User Interface Overview

The User Interface (UI), developed with Tkinter in Python, is streamlined into three primary sections, as illustrated in Figure 2.18.

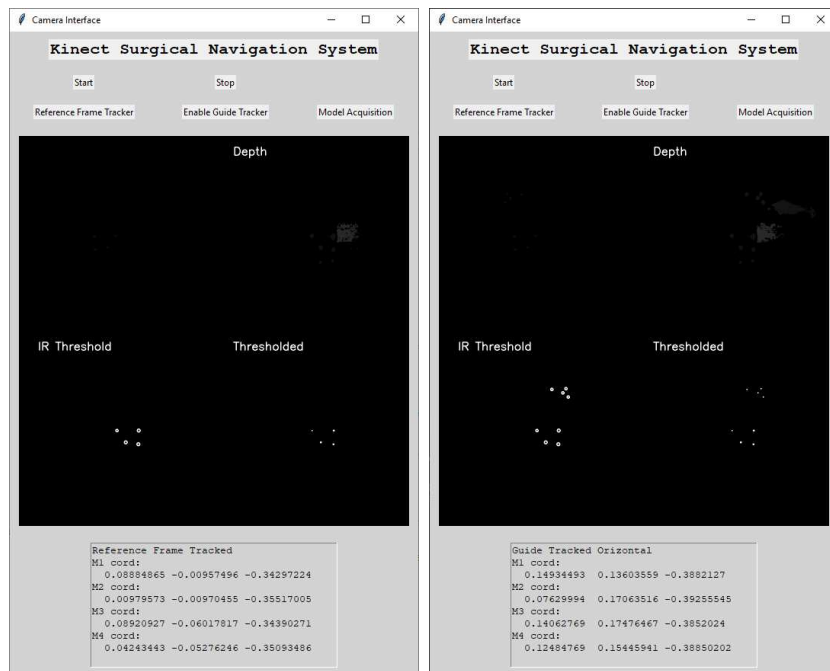


Figure 2.18: Acquisition Data User Interface

- **Control Panel:** At the top, this section houses buttons for operations such as starting, stopping, selecting tracking tools, and model acquisition.
- **Visualization Area:** The middle section exhibits live Kinect sensor frames. It displays the IR camera's original feed, a corresponding depth map, frames with spherical markers, and the post-threshold IR image.
- **Data Output:** The lower section lists the coordinates derived from the Kinect's frames, which are essential for subsequent data evaluation and tracking performance.

2.4.2 UDP communication protocol

The User Datagram Protocol (UDP) is tailored for datagram-based communication across computer networks and utilizes the Internet Protocol (IP) as its foundational layer. UDP streamlines message transmission for applications by minimizing protocol overhead. It is a transaction-oriented protocol without guaranteed delivery or protection against duplicates [62]. When both sender and receiver are on the same machine, as in this setup, the loopback IP address '127.0.0.1' is utilized. The UDP implementation, sourced from the "Python-Unity-Socket-Communication" repository, is initiated with the code below:

```
1 sock = U.UdpComms(udpIP = '127.0.0.1', portTX=8000, portRX=8001,  
    enableRX=True, suppressWarnings=True)
```

This code configures two ports to transmit and receive data concurrently, facilitating communication with the system framework.

Chapter 3

X-Ray Simulator and AR Guide System Development

The tracking system workflow explained in the previous chapter provides the three-dimensional coordinates of the tracking tool markers. The processed data is subsequently transmitted to a X-Ray Simulation Software and AR guide systems, developed in Unity, employing the UDP communication protocol.

3.1 X-ray and AR guidance system overview

3.1.1 X-ray in trauma procedures

X-rays, a form of electromagnetic radiation, penetrate the body. Tissues body are characterized by a different absorption that confers a different representation in radiological images. This differential absorption provides contrasting visual representations: bones, which have a high level of attenuation, appear white, while softer tissues with less attenuation appear darker [63].

In orthopedic surgery are used to create images of internal structure to asses broken bones, joint abnormalities and spine injuries. In trauma care for suspected fractures, the typical steps include assessment, X-ray imaging, and treatment:

- *Patient Evaluation:* The patient undergoes a physical examination and medical history review. This step may involve checking for signs of a fracture such as swelling, deformity, tenderness, and inability to move the affected area. Pain response and vascular assessments are also critical to determine the severity of the injury.



Figure 3.1: C-Arm for Scintigraphy

- *Radiographic Imaging:* X-ray is the first line of imaging used to confirm the presence of a fracture. If the fracture is complex or involves a joint, a Computed Tomography (CT) scan may be conducted to gain a detailed view of the bone fragments and their positions. A CT scan provides cross-sectional images, offering a clearer picture of the extent of the fracture.
- *3D Modeling:* where surgical intervention is required, 3D models of the fracture can be created using the imaging data. These models help understand the fracture's geometry and plan the surgery with precision.
- *Surgical Intervention:* if stabilization is necessary K-wires are placed in the affected bones. K-wires can be used to temporarily or permanently stabilize bone fragments, depending on the nature of the fracture. The placement of K-wires is done carefully to align the bones for proper healing and to avoid damaging nearby structures, such as nerves or blood vessels.

3.1.2 AR system in trauma

In image-guided interventions crucial is the surgeons' capacity to mentally reconstruct the 3D surgical environment based on intra-operative images [64]. Augmented reality technology holds potential for enhancing surgical planning and in the intra-operative context. Surgical reconstruction software and 3D X-ray images permit the bone positioning planning for the insertion of k-Wires in target positions. This enables the visualisation of available trajectories on the surgical field. Within the intraoperative phase, AR navigation systems could lead to a reduction in surgical time and the equivalent X-ray doses required for the correct insertion of screws and/or K-wires. This enriches surgical awareness and surgeon comfort and efficiency [36, 37].

3.1.3 HoloLens 2 [65]



Figure 3.2: HoloLens 2

HoloLens 2, developed by Microsoft, is an holographic computer for mixed reality experiences. Users can interact with holograms merging digital content with the real environment. The device is equipped with six cameras, making it particularly useful as a data acquisition unit:

- The depth camera employs active infrared (IR) illumination and phase-based time-of-flight technology to determine depth. It operates in two modes: one for high-frequency (45 FPS) detection of near depth, often used for hand detection, and another for low-frequency (1-5 FPS) detection of far depth, currently utilized for spatial mapping;
- Two greyscale cameras act as a stereo pair, capturing the front area to determine the absolute depth of detected visual features through triangulation;
- The two extra greyscale cameras widen the field of view for feature tracking. These synchronized global shutter cameras are more light-sensitive than the color camera and can capture images at a rate of up to 30 fps;
- The color camera has autofocus, automatic white balance and automatic exposure. It can capture 8 MP photos and shoot 1080p video at 30 frames per second.

3.2 Tracking Tools Pose Estimation

The camera center serves as the origin of the global reference system, as detailed in section 2.2.1. The local reference system for each tracking tool is derived from its spherical markers. Out of the four markers on each tool, only three are utilized for this calculation. The additional marker is employed to unambiguously resolve the correspondence problem.

3.2.1 Local Reference System Calculation Algorithm

Considering three markers:

$$P_1(x_1, y_1, z_1), P_2(x_2, y_2, z_2), P_3(x_3, y_3, z_3)$$

The local reference system can be computed as follow, considering P1 the origin of the local reference frame.

1. The **x-axis** is determined by the difference between marker 1 and marker 2:

$$\vec{x} = \langle x_2 - x_1, y_2 - y_1, z_2 - z_1 \rangle$$

$$\hat{x} = \frac{\vec{x}}{\|\vec{x}\|}$$

2. The difference between marker 3 and marker 2 is computed to calculate a support vector:

$$v_{sup}^{\vec{}} = \langle x_3 - x_2, y_3 - y_2, z_3 - z_2 \rangle$$

The normal of the plane containing the vectors \vec{x} and $v_{sup}^{\vec{}}$ is determined by their cross product:

$$\vec{n} = \vec{x} \times v_{sup}^{\vec{}}$$

3. The **z-axis** is obtained by the vector product of the x-axis and the plane normal to the three markers.

$$\vec{z} = \hat{x} \times \vec{n}$$

$$\hat{z} = \frac{\vec{z}}{\|\vec{z}\|}$$

4. The **y-axis** is derived from the vector product of the x-axis and the z-axis

$$\hat{y} = \hat{x} \times \hat{z}$$

3.2.2 Local Reference System for Tracking Tools

The algorithm explained in the previous section, applied to the positions of the guide and stand markers lead to a reference systems as shown in the Figure 3.3.

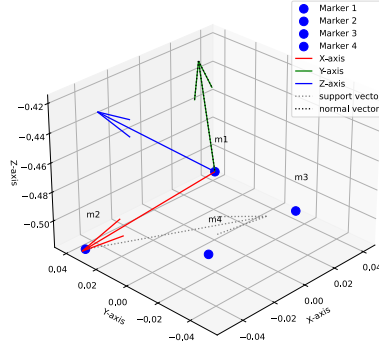


Figure 3.3: Tracking Tool Local Reference System

The x -axis is derived from the positional difference between markers $m2$ and $m1$. The *support vector* is calculated from the positional difference between markers $m3$ and $m2$. The *normal vector* to the plane is then obtained by the cross product of the support vector and the X-axis. The z -axis is determined by the cross product of the normal vector and the X-axis. Finally, the y -axis is the result of the cross product of the X-axis and the Z-axis. This construction ensures that the axes are orthogonal to each other, forming a right-handed coordinate system.

3.2.3 Phantom Reference Frame Positioning

The accurate positioning of the phantom stand's reference frame in the virtual space is critical. For data acquisition, the frame must remain stationary from the beginning of the procedure and throughout its duration. This positioning process can be initiated directly from the start screen. To minimize noise in determining the reference frame's position, the positions of all markers are averaged over a 10-second time window, as demonstrated in the equation below:

$$\bar{x}(t) = s(t) + \frac{1}{N} \sum_{i=1}^N n_i(t) \quad (3.1)$$

3.3 X-ray and AR guidance system Interface

3.3.1 X-Ray Simulator

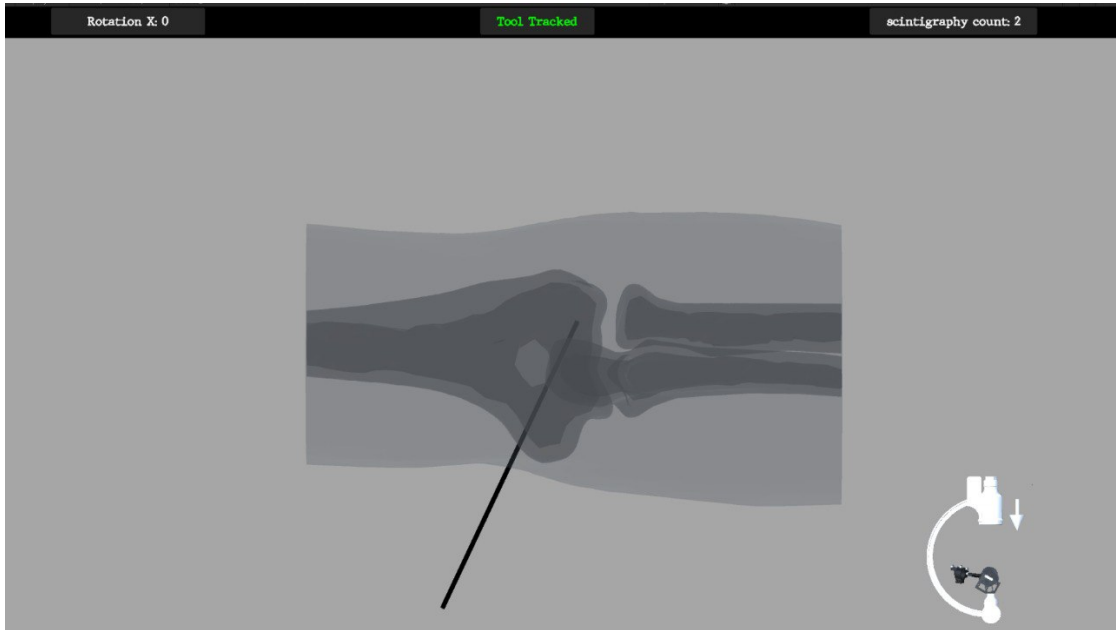


Figure 3.4: X-ray emulator

The method described integrates gamification components to simulate intraoperative radiography with C-arms. The C-arm simulator operates on Unity engine and is able to interface with a Hololens 2. Virtual models imported from Fusion 360 to Unity, simulates a patient's elbow under a C-Arm. Phantom tissues representation mimic X-ray attenuation. Bones appear whiter due to high attenuation, while skin and other subcutaneous tissues are darker due to lower attenuation. Blood vessels and nerves are not visible.

The interface allows the user interact with the C-arm in a realistic way. It renders a detailed visualization of the virtual scene, modelling the spatial relationship between the virtual C-arm configuration and the physical phantom model. Additional information are provided to the user: number of shots taken; the tracking status of the tool and the angle of rotation of the C-arm. To allow users a more natural interaction, without the limits of the user interface, c-Arm rotation and radiograph generation can be controlled by a pedal foot.

3.3.2 AR guidance system

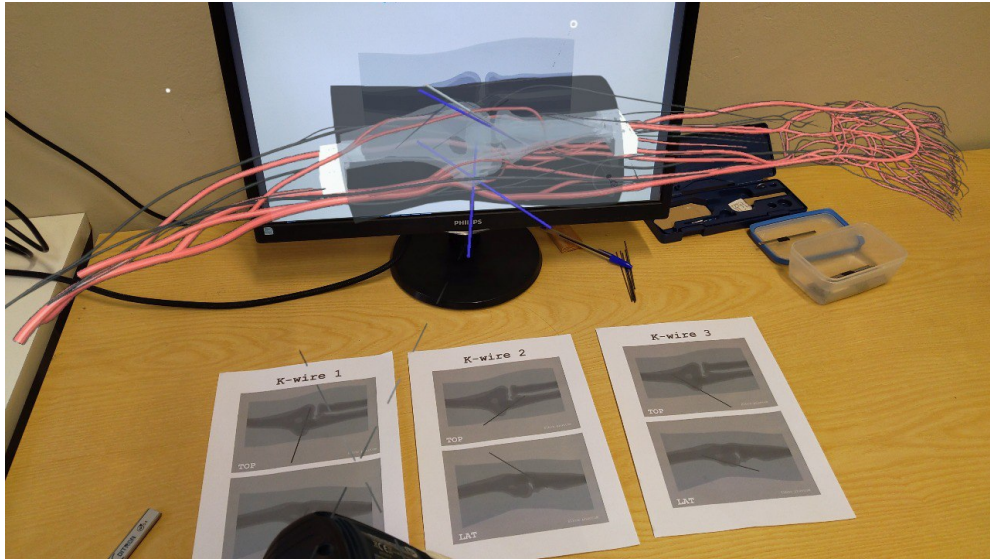


Figure 3.5: HMD view of AR scene during insertion

AR technology is an important innovation in image-guided surgery (IGS) systems. It results in easy integration of surgical navigation with virtual planning based on patient anatomy [66]. External monitors, handheld displays, head-mounted displays, and patient projections offer options for experiencing an AR environment [67].

In this scenario, using an HMD (HoloLens 2), a virtual representation of the dummy with vascularization and innervation is projected. The navigation system does not overlap with the real system, allowing the operator to focus his attention on the simulated surgical field.

The AR application is developed with MRTK. It offers a cross-platform input system, foundational components, and spatial interaction building blocks. The app run locally in the Unity editor on a PC in Play Mode and is streamed to the HoloLens. Data is transferred via Wi-Fi connection. The connection between devices is established after entering the IP address of the HoloLens 2 in the Remote Host Name box in Unity.

The user has the ability to manipulate the virtual model via hand gesture recognition. This enables the model to be spatially positioned and scaled in size using hand movements.



Figure 3.6: Command Menu displayed in AR user interface

Furthermore, by placing the palm in front of the face, users can access the "*Command Menu*" (see Fig.3.6) for more options. This function allows for automatic model positioning in scene, anchors the model in place and visualizes the kWire target.

3.3.3 System Settings Interface

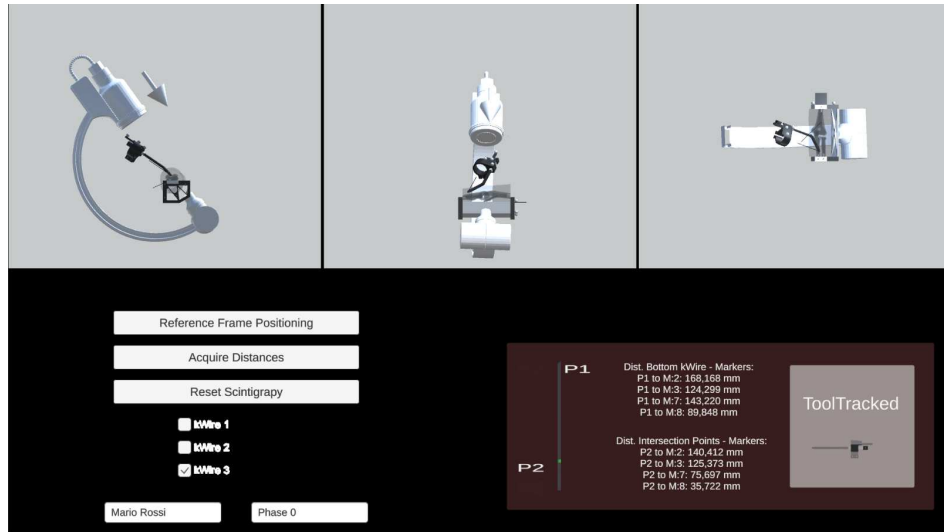


Figure 3.7: System Settings Interface

The "Settings System Interface" allows technicians to interface with the system and controls the its correct functionality. The interface has three views (side, front, and top) to keep track of the correct link between virtual and real-world elements. Furthermore, the following interaction elements are availables:

- **Reference Frame Positioning** (button): it initiates the detection process for the stand's coordinates .
- **Acquire Distances** (button): it measure the distances between reference points on the wire and markers on the dummy;
- **Reset Scintigraphy** (button): it resets the scintigraphy count to zero and the cArm's original inclination.
- **kWire target** toggles selction;
- **"Tester Name"** and **"Phase"** input fields

Additional debug information is accessible in the bottom-right quadrant of the interface. On the right a graphical representation of the reference points on the placed kWire is displayed. When the "Acquire Distances" button is clicked, the measurements appear in the center. While, an iconographic depiction of the currently tracked tool (guide or stand) is shown to the left.

Chapter 4

System Performance and Testing Protocol

The system described is made up of (i) tracking (Chapter 2) and ii) X-ray simulation and AR guidance (Chapter 3). The overall accuracy is assessed by points localization and distance estimation in space. Following the ASTM F2554-10 standard, a tool was developed to extract evaluation parameters.

A protocol is developed to evaluate the effectiveness of augmented reality in enhancing screw and K-wire insertion procedures, aiming to prevent damage to vascular and nerve structures. Augmented reality is compared with simulated X-rays. Data gathered throughout the protocol's implementation is recorded in a database. This database houses both quantitative data for evaluating the tester's performance and qualitative data reflecting the tester's perceptions.

4.1 System Performance Evaluation

The system's performance evaluation consists of two stages: (1) validating fiducial point correspondence and (2) comparing distances obtained automatically by the system to those measured manually with a gauge. The parameters to be evaluated are:

- point's relative location in a coordinate system;
- repeatability of single-point coordinates;
- relative point to point accuracy.

4.1.1 Accuracy and Precision

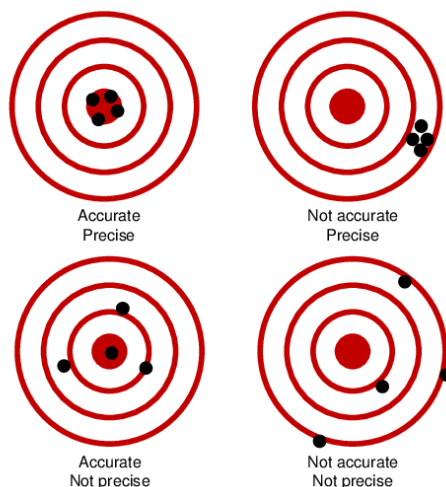


Figure 4.1: Difference between accuracy and precision

Evaluating CAS-Systems performance depends on the definitions of *accuracy* and *precision* [68].

- *Precision* depends on random errors distribution by repeated measurements with an equipment. It describes the sturdiness of the measuring instrument, a higher standard deviation indicates worse precision;
- *Accuracy* is the degree of approximation to a specific expected value. It concerns outcome quality, arising from both random elements and a common systematic error.

4.1.2 Fiducial Points

The purpose is to measure and document the fundamental static performance characteristics of the system, such as accuracy and repeatability. This involves evaluating the system's ability to maintain positioning and movement control under specific conditions and its capability to reproduce results over multiple iterations.

Data Acquisition Procedure

The primary aim of this procedure is to accurately map the spatial coordinates of specific points within both real and simulated environments. This mapping process leverages points on a 3D-printed stand as fiducial markers to ensure precision and reliability in the data acquisition process. Fiducial markers are critical in this

context as they serve as reference points that can be easily recognized both by the data collection system and in the analysis phase.

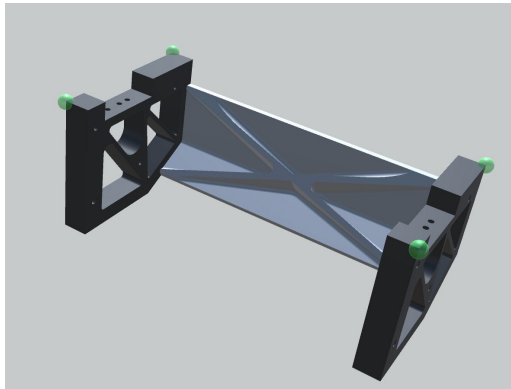


Figure 4.2: Fiducial Markers on Stand

To capture the precise location of each marker, the procedure entails the utilization of a tracking tool, which is maneuvered into six distinct orientations for every point of interest. This multi-orientation approach is designed to enhance the accuracy and robustness of the spatial data collected, by mitigating potential errors or biases associated with any single viewpoint.

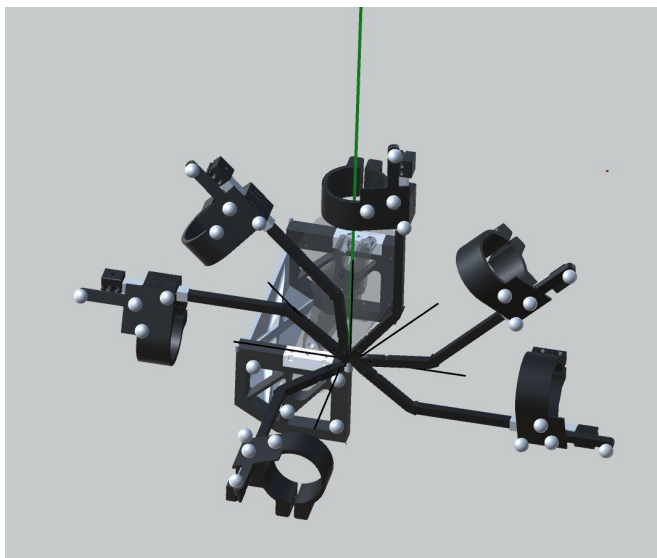


Figure 4.3: Tool Poses for Coordinate Acquisition in Fiducial Points

4.1.3 Manual and Automatic Distance Measurements

The simulation phantom presented in subsection 2.2.3 holds ten marks arranged in its circumference. During the insertion test involving 45 k-Wires, eight measurements were taken in each k-Wire. Specifically, two points on the positioned k-Wire were used as reference: the posterior extremity (P1) and the point of contact with the skin (P2). Distances from these reference points to four selected markers were recorded using both a manual gauge and the system automatic measurements. Only the distances calculated on P1 are considered for the accuracy evaluation. Although the algorithms were initially designed to calculate P2 at two different points on the k-Wire within the two virtualization systems, this resulted in identical k-Wire matches. Essentially, P2 was solely tasked with defining the direction and magnitude of the vector associated with the k-Wire.

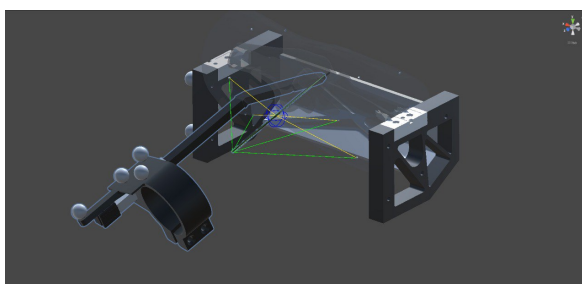


Figure 4.6: Tool User Interface for Performance Estimation

Distances from the measuring system are depicted in figure 4.6. Green lines represent distances from P1 to markers and yellow lines from P2 to markers. The blue sphere indicates the k-Wire entry point related to P2.

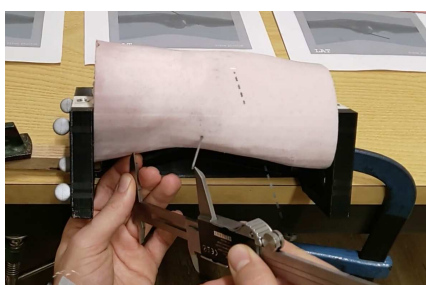


Figure 4.7: Distance Registration with Gauge

Figure 4.7 shows how a distance measurement using a gauge is acquired. For each individual k-Wire is repeated for the eight P1-P2-marker combinations.

4.2 Testing Protocol

4.2.1 Objectives

The protocol's primary objectives are:

- *validation of the Developed Software-Hardware System*: the aim is to evaluate the system's performance for educational and practical applications in surgical settings;
- *comparison of Precision between X-ray and AR Guidance for K-wire Placement*: by comparing these two methods, the protocol intends to identify the strengths and weaknesses of each, with the goal of enhancing surgical precision and outcomes.
- *analysis of the Learning Curve*: this objective involves monitoring progress to understand how skill acquisition unfolds, aiming to optimize the learning process for surgical residents.
- *assessment of Iatrogenic Harm Risk*: this assessment is focused on quantifying the safety of procedures when using the new system, with the ultimate aim of minimizing any potential risk to patients.

4.2.2 Testing Environment

The test environment consists of:

- **director workstations**: running the "*Tracking System*" and the "*X-Ray Simulator and the Augmented Reality Guide System*";
- **collector workstations**: running the "*AR k-wire placement test companion*" and the "*K-wire virtualization system*";
- **candidate workstation**: for interaction with surgical phantom, the simulated X-rays and the AR visor.

The subsystems work together as follows. The tracking system processes coordinates for the "*X-Ray Simulator and Augmented Reality Guide System*". Users interact with the simulation environment, and technicians adjust the system according to protocol requirements. The "*data collector*" assists users with the "*AR K-wire Placement Test Companion*" and collects data. Are gathered feedback from the candidates and measurements for the "*k-Wire Virtualization System*".

4.2.3 Workflow

The protocol consists essentially of two phases (PHASES): *Phase 0* allows X-ray usage, while *Phase 1* introduces augmented reality navigation system support. To observe learning effects from AR use, Phase 2, a repeat of Phase 1, can be conducted. Before starting, candidates receive instructions on drill usage and virtual X-ray machine operation for imaging and can interact with the phantom.

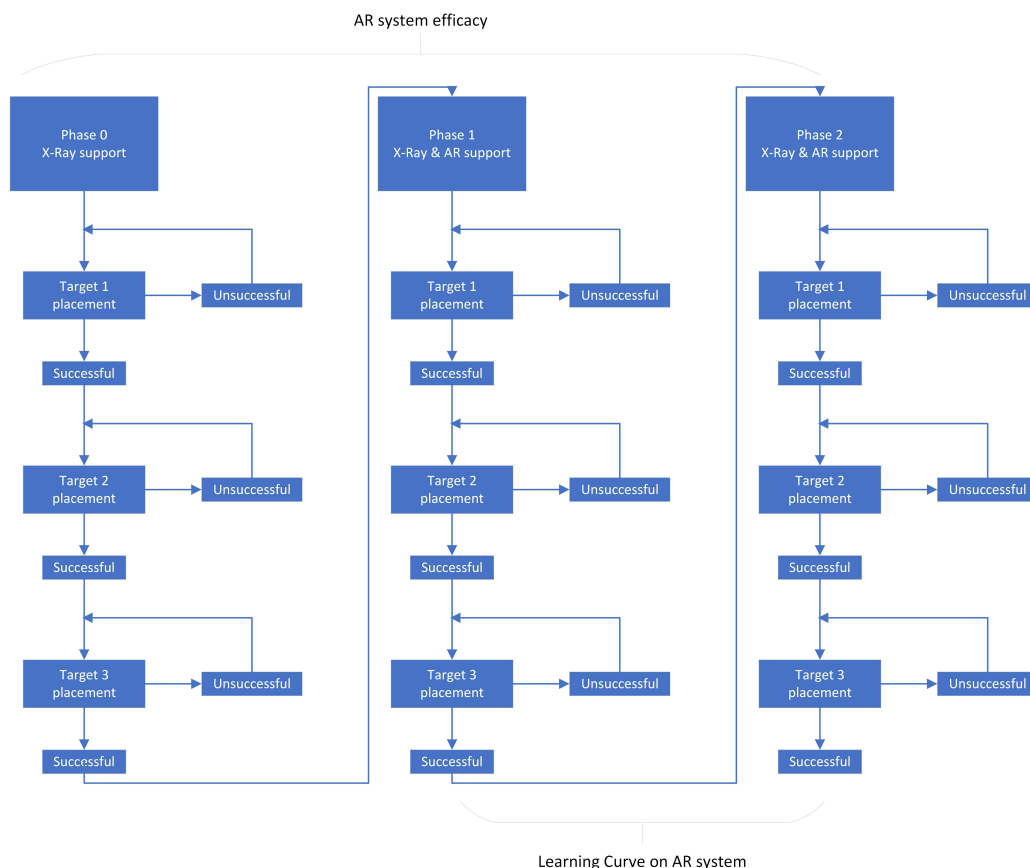


Figure 4.8: Protocol phases execution workflow

Positional parameters are obtained by consecutively inserting three K-wires. Their target positions are indicated by AP orthogonal view X-ray representations (as shown in Figure 4.9). Participants may declare the *positioning attempt* (PA) *successful* if satisfied; otherwise, they may reposition the K-wire after declaring the placement *unsuccessful*. Data are collected in both scenarios. The *Estimated Correct Position* (ECP) is defined as the PA that enables the candidate to achieve the correct K-wire position relative to the target.

Data gathered includes:

- *Demographics*: nationality, age, surgical and 3D vision experience, glasses use;
- *Time*: seconds for each PHASE, ECP, PA;
- *X-ray counts*: from the simulator;
- *Manual k-Wire measures*: 3D positions via 4 markers;
- *Automatic k-Wire measures*: calculated P-marker distances;
- *PA outcomes*: success and failure rates per PHASE and ECP.

Each PA is identified by a 10-character hexadecimal string called Database ID, correlating it with its originating ECP and PHASE.

k-Wire target in Phantom

Considering the bone structure of the elbow, k-Wire targets 1 and 3 are inserted at the distal end of the humerus, specifically into the medial epicondyle. Target 2 is inserted at the proximal end of the ulna, near the olecranon.

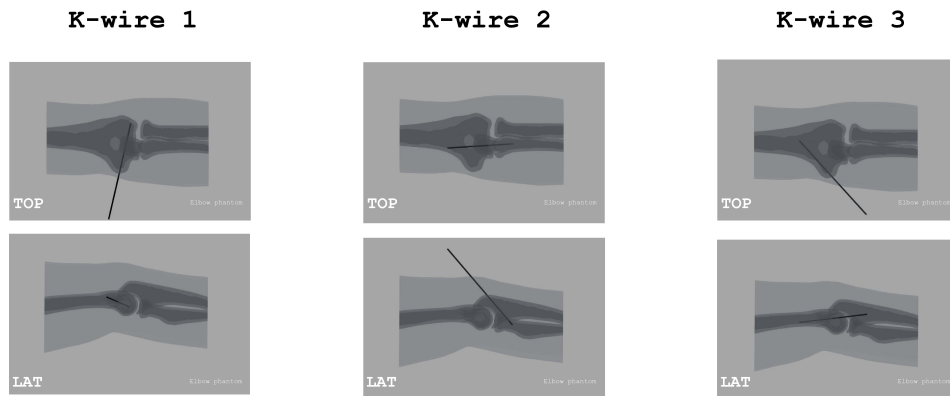


Figure 4.9: k-Wires representation in x-Ray AP view

Chapter 5

Results

5.1 System Performance Data Analysis

5.1.1 Point's relative location in a coordinate system

The relative positions acquired in relation to the fiducial points are shown in the figure. The point (0,0,0) in each subplot corresponds to the fiducial marker.

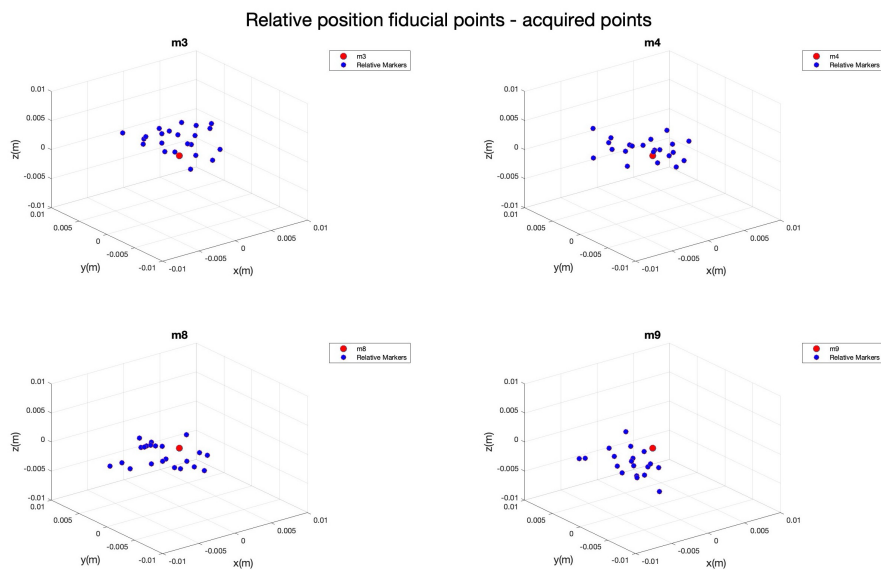


Figure 5.1: Relative position acquired points - fiducial markers on stand

The average acquisition error is defined as the Euclidean distance between the coordinates of the acquired point and the ideal location of the fiducial marker. As shown in figure 5.2, it fluctuates minimally in response to changes in the camera

distance. The mean error ranges from 5.29 mm at 0.6m to 6.15 mm at 0.4 m. This indicate that the tracking system’s accuracy might be relatively unaffected by the distance. Standard deviation varies from 2.13 at 0.3m, indicating the highest consistency, to 3.43 at 0.5m, showing the most variability. This suggests that the distance may have an impact on the tracking system’s consistency.

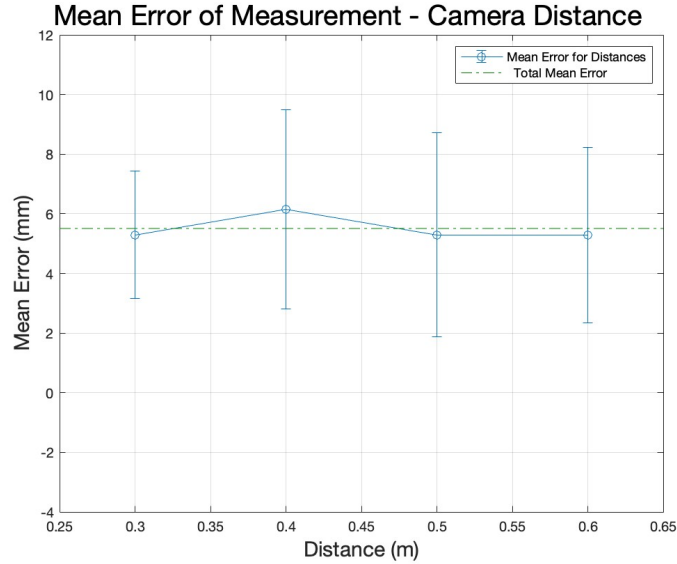


Figure 5.2: Euclidean Acquisition error Distance with Standard Deviation. Distances: 0.3m(N=16); 0.4m (N=24) 0.5m (N=24);0.6m (N=24)

Cam Dist (m)	$\Delta x_{\text{Mean}} \pm \text{SE}(\text{mm})$	$\Delta y_{\text{Mean}} \pm \text{SE}(\text{mm})$	$\Delta z_{\text{Mean}} \pm \text{SE}(\text{mm})$
0.3	3.199 ± 0.438	2.550 ± 0.537	2.149 ± 0.499
0.4	3.754 ± 0.397	2.628 ± 0.420	2.920 ± 0.701
0.5	3.732 ± 0.000	2.452 ± 0.000	1.679 ± 0.000
0.6	3.284 ± 0.575	2.594 ± 0.504	1.962 ± 0.250

Table 5.1: Coordinates error in x,y,z at different camera distances: 0.3m (N=16); 0.4m (N=24); 0.5m (N=24); 0.6m (N=24)

The table 5.1 displays mean deviations along the x, y and z axes (Δx_{mean} , Δy_{mean} , Δz_{mean}) corresponding to varying camera distances (0.3m, 0.4m, 0.5m and 0.6m). For each axis the differences in error as the camera distance changes are not markedly significant. Specifically, the deviation is typically larger along the x-axis, averaging around 3mm, and tends to be smaller for the z-axis.

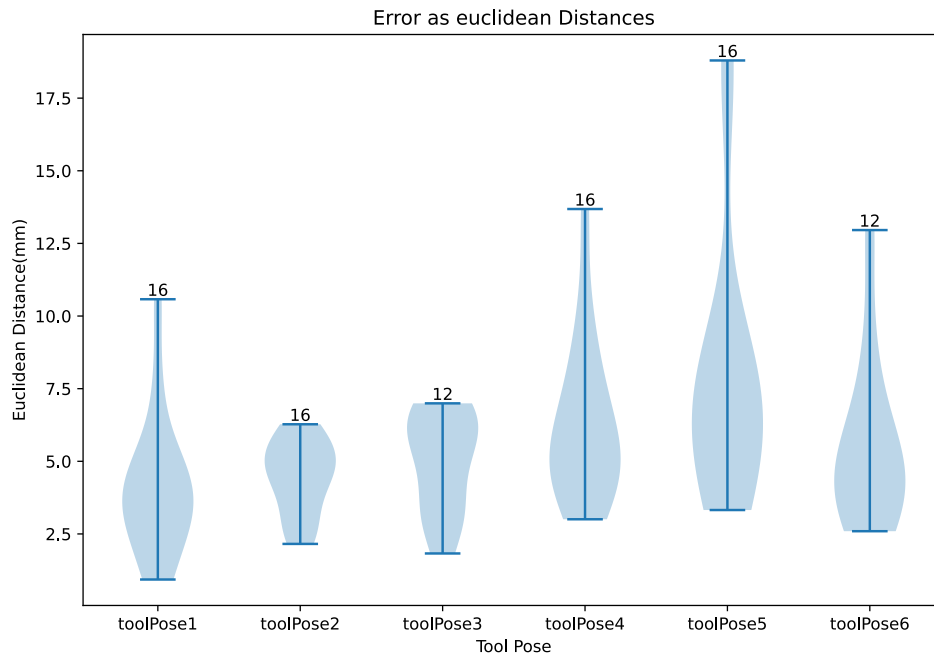


Figure 5.3: Euclidean distance error - Tool Pose

The plot in figure 5.3 illustrates the variability and precision of measurements for each tool pose. It demonstrates that the positioning of the tracking tool affects the precision of the recorded measurements. Tool Pose 5 exhibited the highest error, while Tool Pose 2 demonstrated the lowest error.

5.1.2 Repeatability of single-point coordinates

The repeatability of the coordinates of a single point is examined for each acquisition distance. As it changed, the system was recalibrated by updating the absolute coordinates of the fiducial markers. Data is reported in the appendix A.1. The average position of the tool tip is determined by calculating the mean of all recorded tool tip locations. The deviation of each individual measurement from the mean position is computed. The average deviation, the maximum error, and the standard deviation of the deviations are reported in tables.

Measurements at 30cm

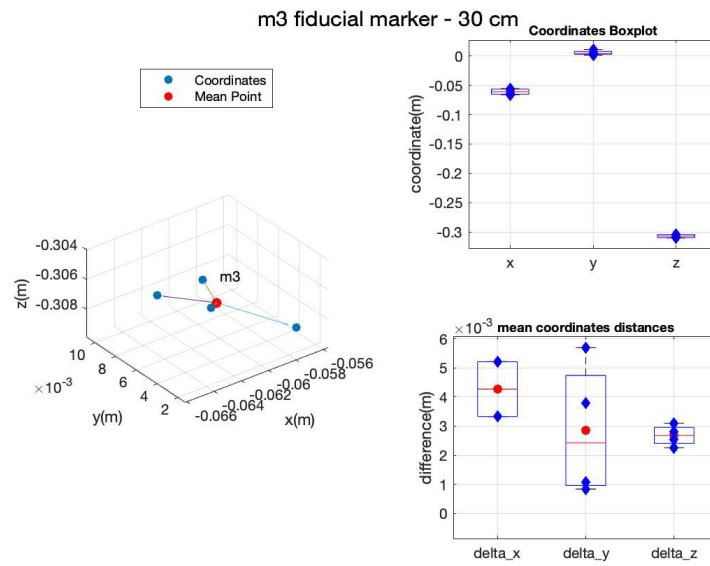


Figure 5.4: Repeatability M3 fiducial marker at 30cm

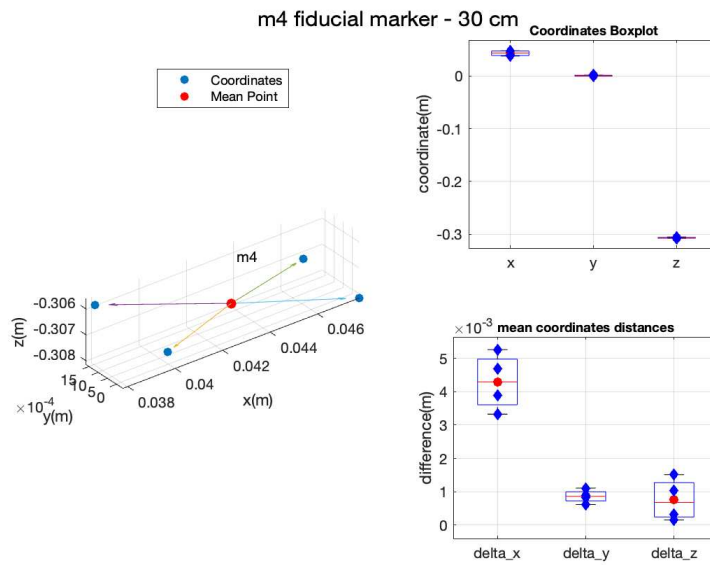


Figure 5.5: Repeatability M4 fiducial marker at 30cm

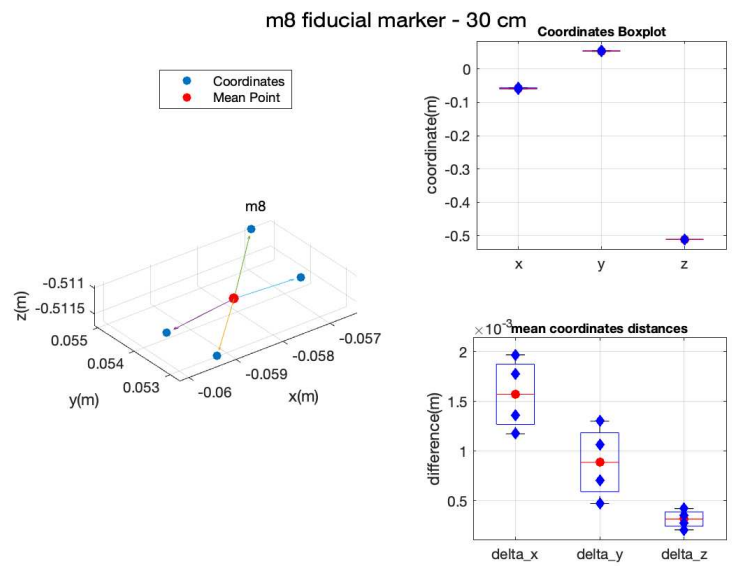


Figure 5.6: Repeatability M8 fiducial marker at 30cm

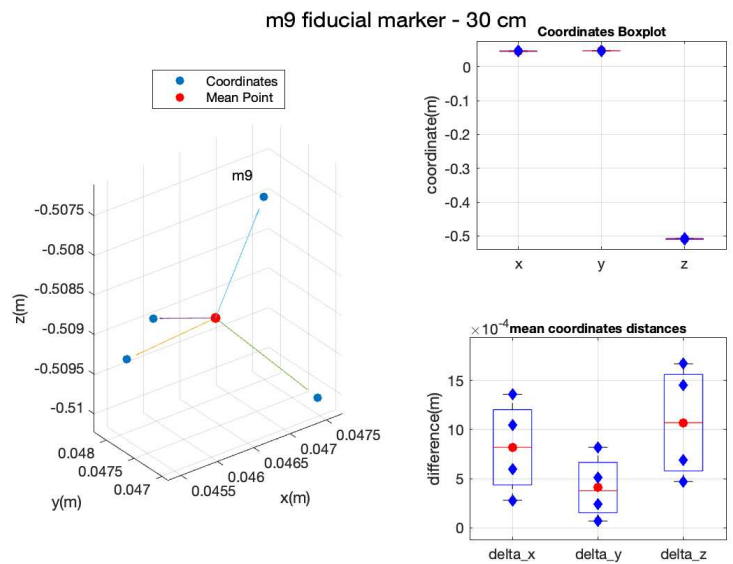


Figure 5.7: Repeatability M9 fiducial marker at 30cm

Measurements at 40 cm

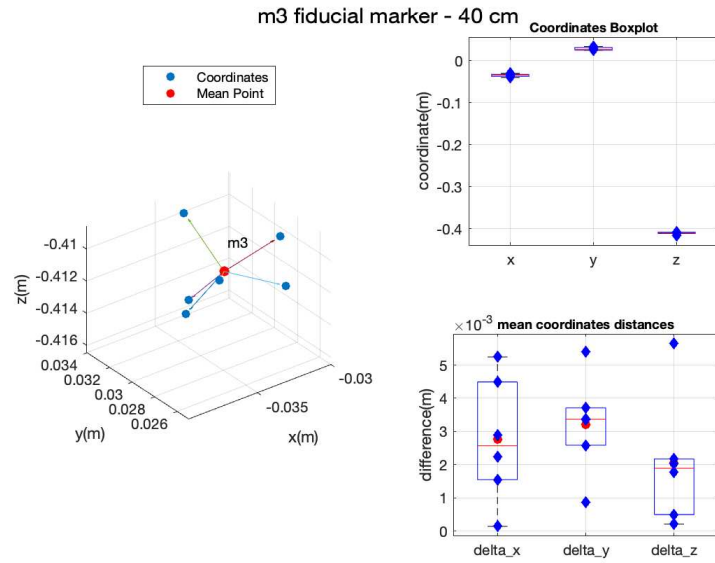


Figure 5.8: Repeatability M3 fiducial marker at 40cm

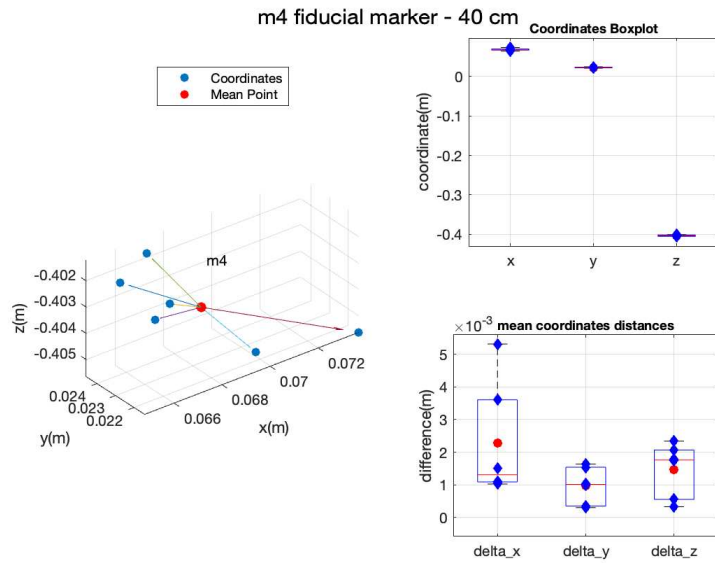


Figure 5.9: Repeatability M4 fiducial marker at 40cm

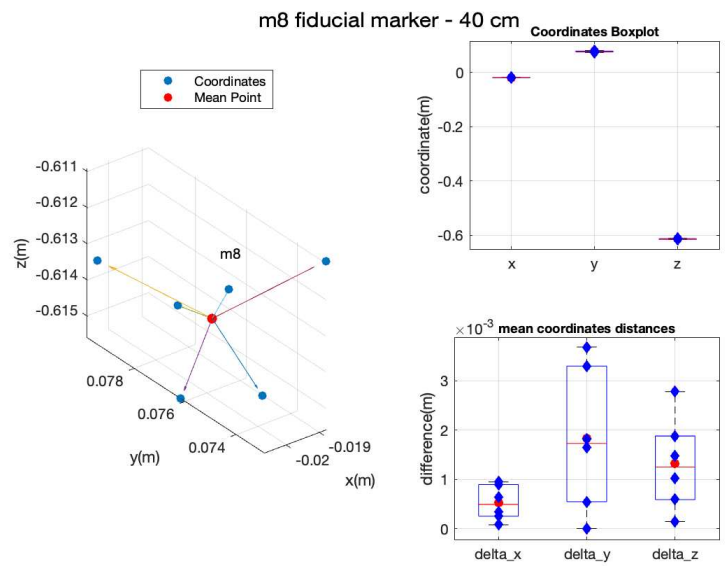


Figure 5.10: Repeatability M8 fiducial marker at 40cm

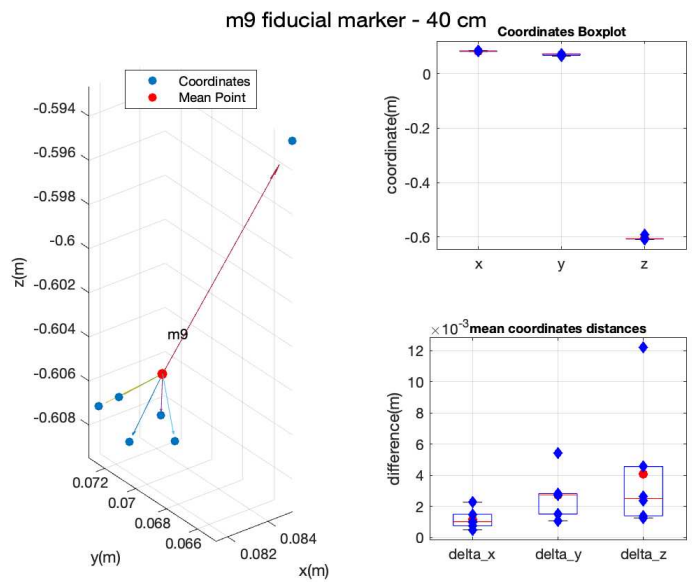


Figure 5.11: Repeatability M9 fiducial marker at 40cm

Measurements at 50 cm

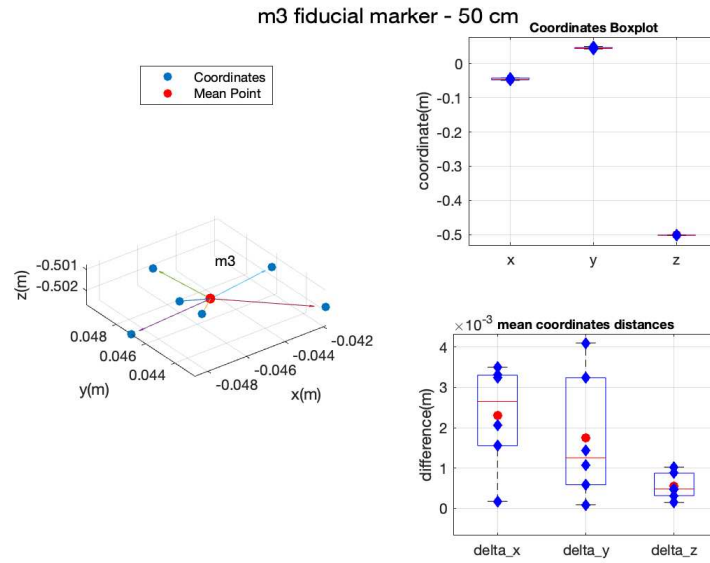


Figure 5.12: Repeatability M3 fiducial marker at 50cm

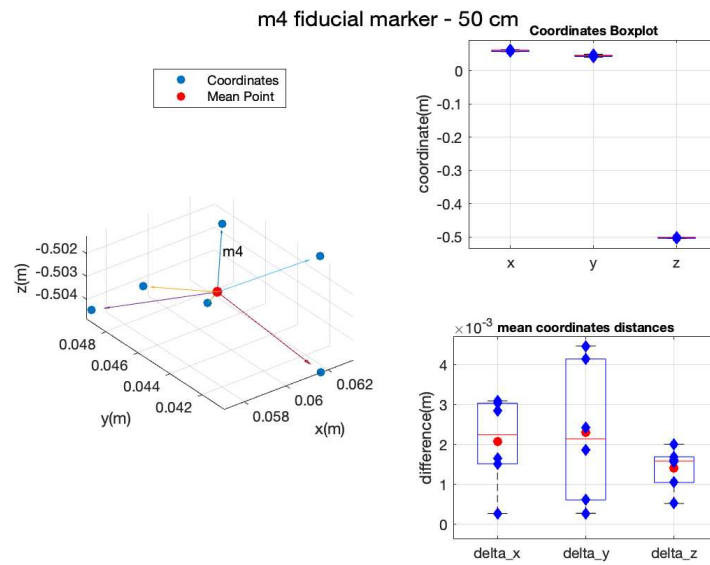


Figure 5.13: Repeatability M4 fiducial marker at 50cm

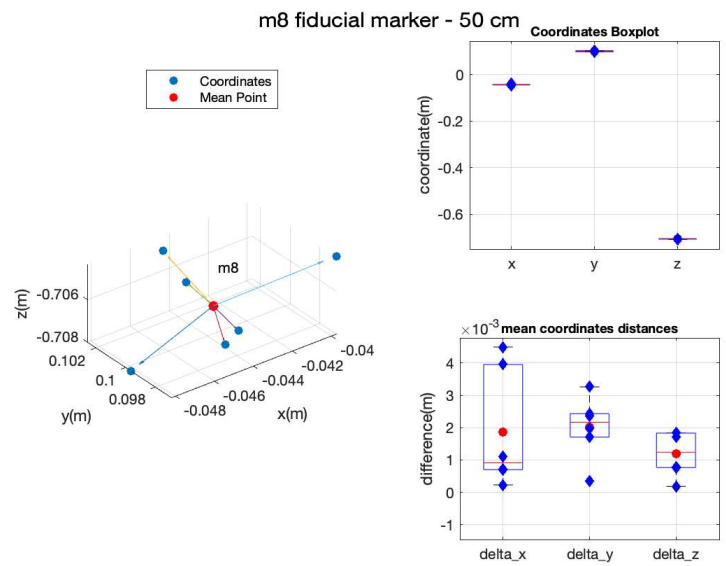


Figure 5.14: Repeatability M8 fiducial marker at 50cm

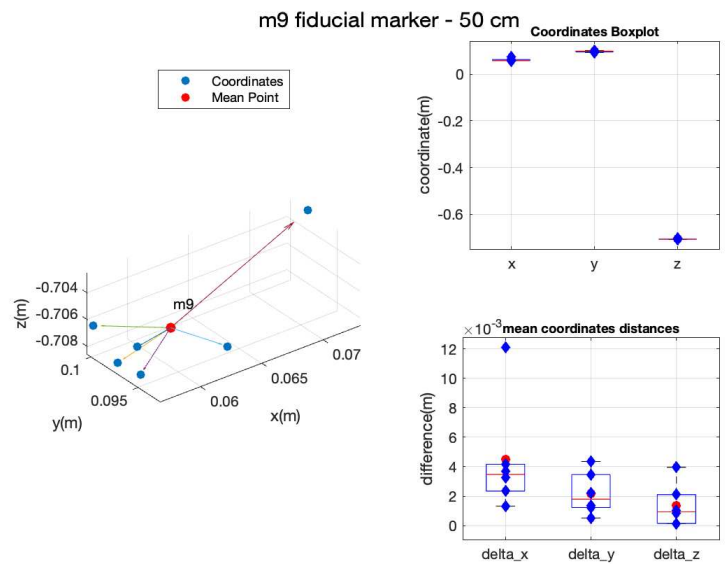


Figure 5.15: Repeatability M9 fiducial marker at 50cm

Measurements at 60 cm

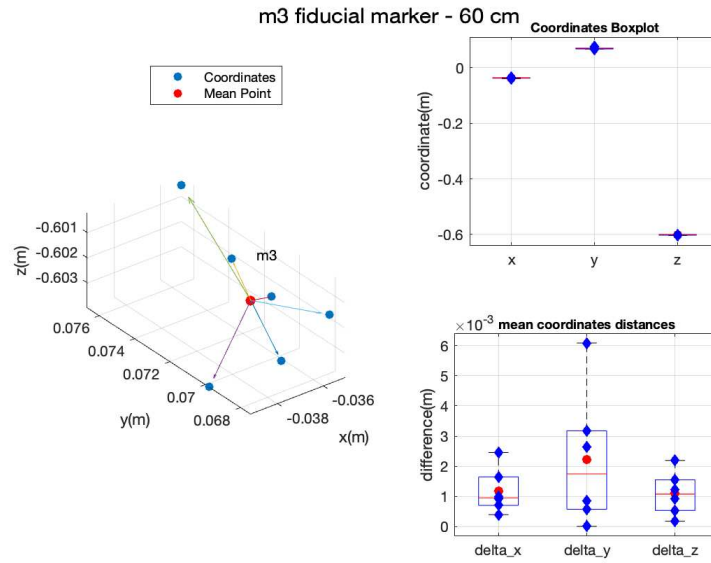


Figure 5.16: Repeatability M3 fiducial marker at 60cm

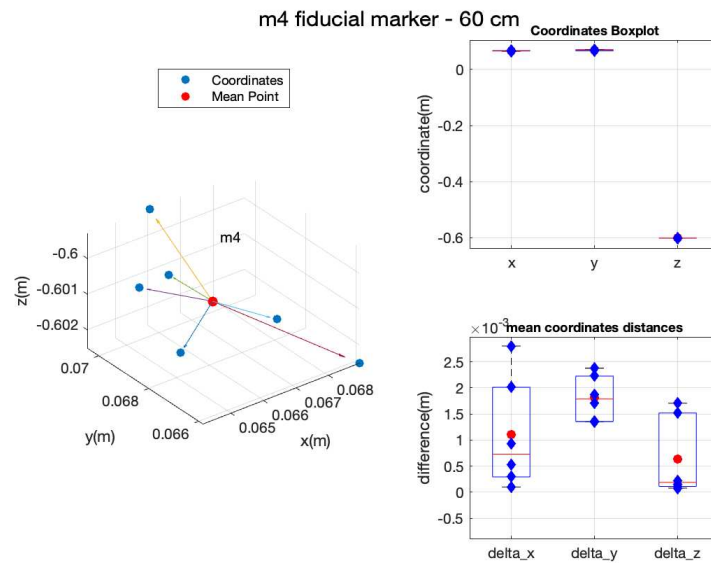


Figure 5.17: Repeatability M4 fiducial marker at 60cm

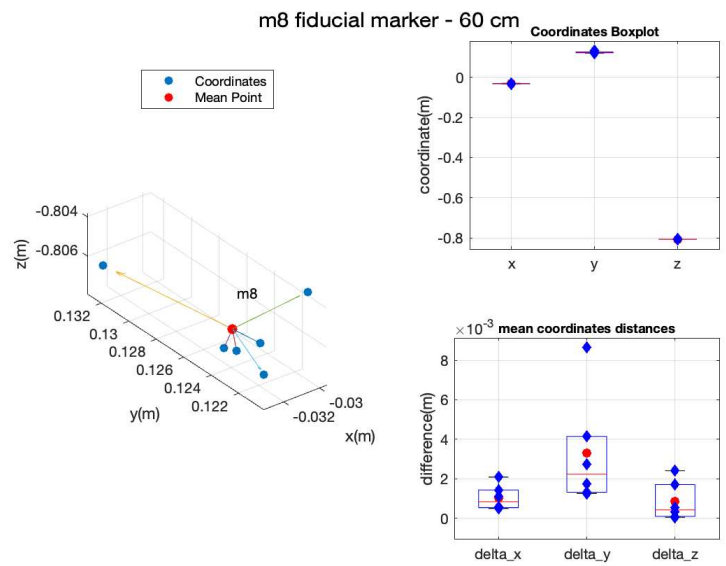


Figure 5.18: Repeatability M8 fiducial marker at 60cm

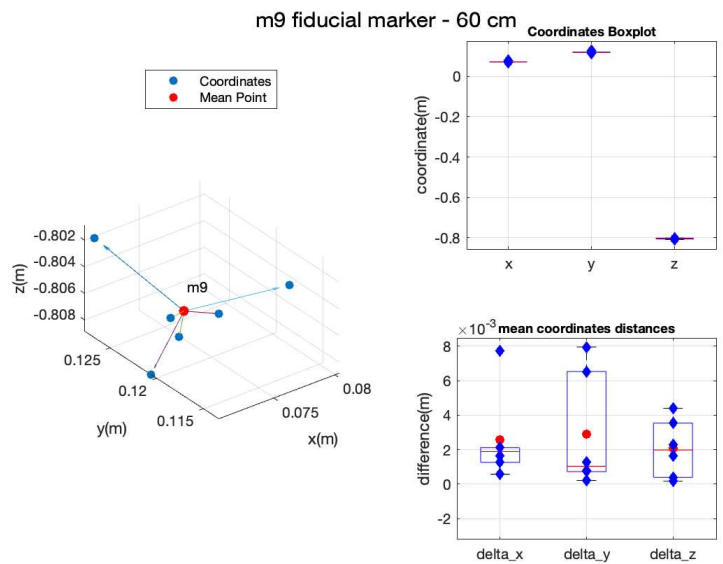


Figure 5.19: Repeatability M9 fiducial marker at 60cm

5.1.3 Relative point to point accuracy

This step aims to assess distance measurement accuracy by calculating the error between the measured and known distances. The evaluation is conducted on two levels: (1) distances calculated using the coordinates of fiducial points; (2) distances measured with calipers and the automatic system on the inserted K-Wire (subsection 4.1.3).

Fiducial Points Distances Analysis

There are four fiducial points considered, from which six distances can be derived. The known distances (Table 5.2) are compared with the measured ones from acquired points.

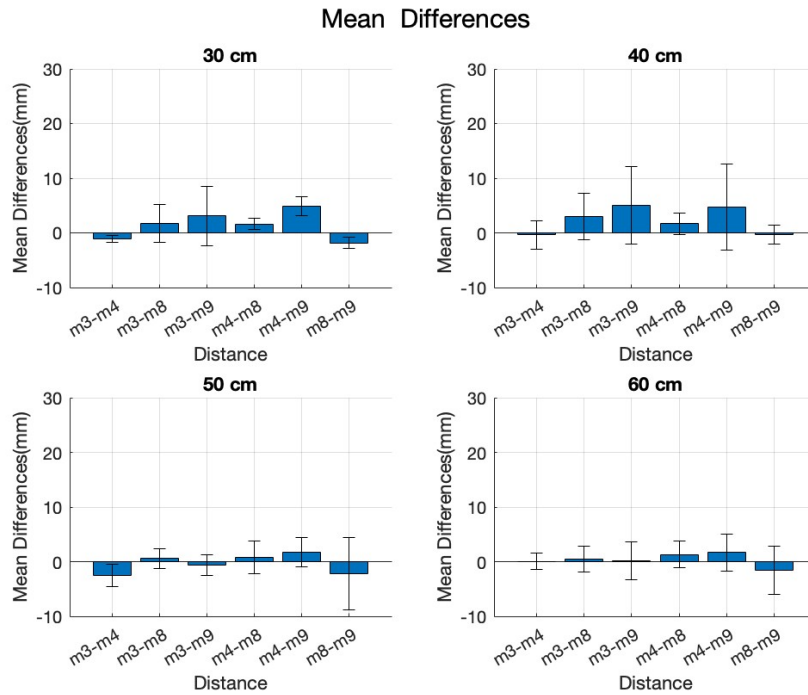


Figure 5.20: Mean differences distances between fiducial points (N=88)

Measurement error increases as the distance between the two markers increases. The figure 5.20 demonstrates that the shortest distances (m3-m4 and m8-m9) exhibit the lowest error and standard deviation values. Conversely, the greatest distances (m3-m9 and m4-m8) are associated with the highest errors and standard deviations.

The increasing distance between the setup and the camera has a positive effect in reducing the difference. As the distance between the setup and the camera increases, both the error and the standard deviation decrease. This is particularly emphasised in the figure 5.21 .The phenomenon could be attributed to the utilization of a wide Field of View (WFOV). It tends to cause greater distortion in distance measurements for objects that are closer to the camera.

Table 5.2: Ideal Distances between fiducial Points

Markers	Distance(mm)
m3-m4	103.00
m3-m8	211.99
m3-m9	235.69
m4-m8	235.69
m4-m9	211.99
m8-m9	103.00

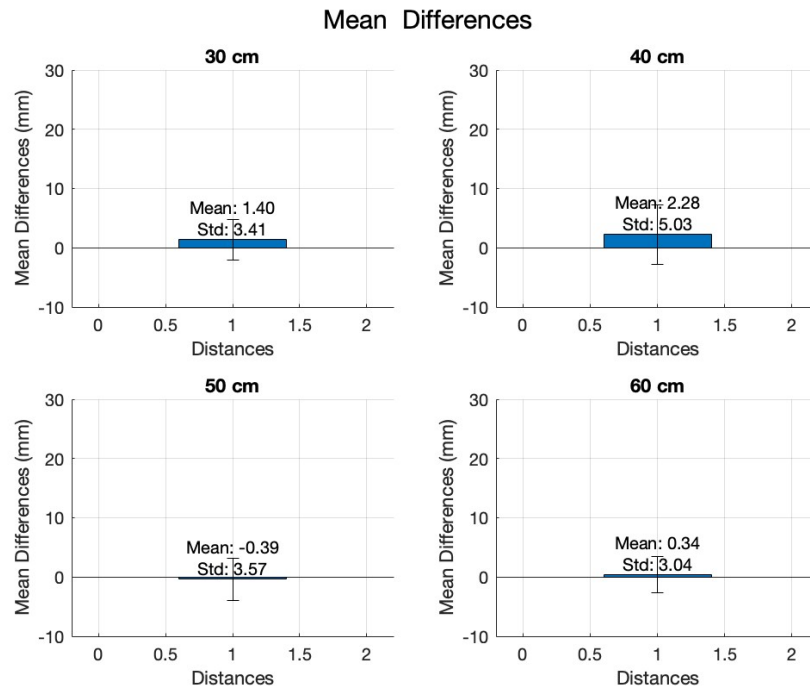


Figure 5.21: Mean distance differences between fiducial points (N=88)

Comparing Manual and Automatic Distance Measurements

Comparison Calibre and Automatic Unity Registration

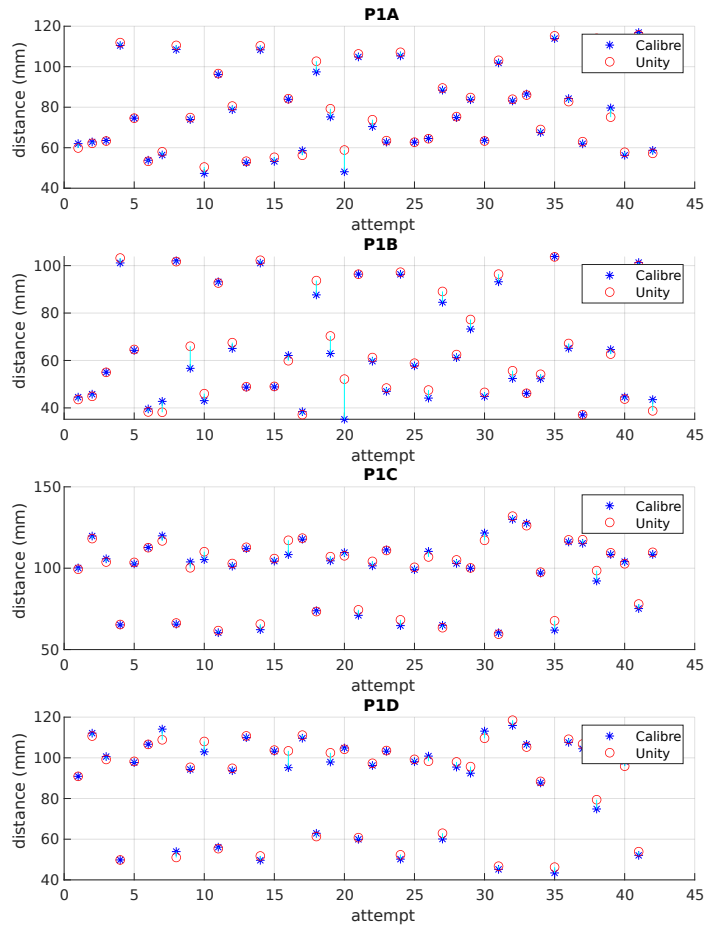


Figure 5.22: Comparison between Calibre and Automatic Distance Acquisition. 4 distance for target: manual measurement $N=168$; automatic measurement $N=168$

The simulation phantom presented in subsection 2.2.3 holds ten marks arranged in its circumference. During the insertion test involving 45 k-Wires, eight measurements were taken in each k-Wire. Specifically, two points on the positioned k-Wire were used as reference: the posterior extremity (P1) and the point of contact with the skin (P2). Distances from these reference points to four selected markers were recorded using both a manual gauge and the system that was developed for automatic measurements. Distance from P1 can be used to evaluate the accuracy

of the system.

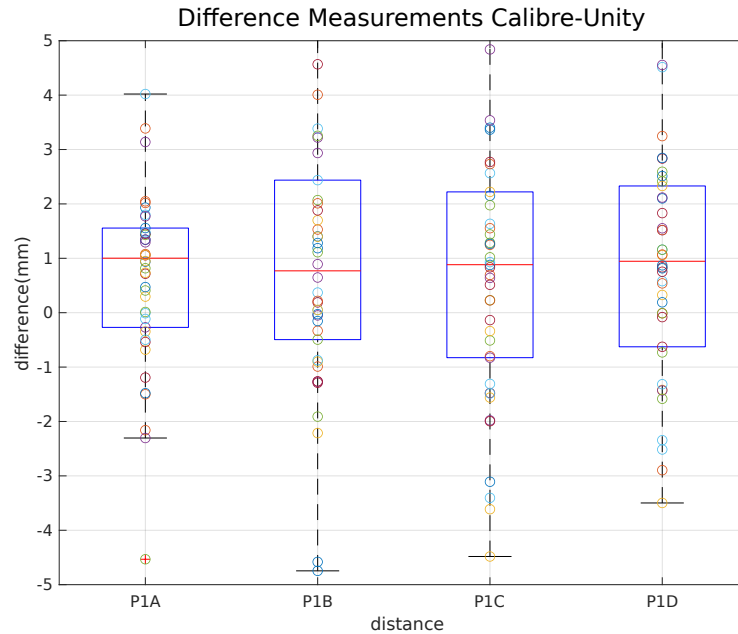


Figure 5.23: Difference between Calibre and Automatic Distance Acquisition. (N=42 for each box plot)

Figure 5.25 presents box plots illustrating the discrepancies between manual (gauge) and automatic measurements.

Difference	P1A	P1B	P1C	P1D	All
Mean(mm)	0.9381	1.4030	0.8783	0.8709	1.0226
SD(mm)	2.3243	3.6618	2.7053	2.4700	2.8217

Table 5.3: Mean and Standard Deviation Difference Values (N=42 for each distance)

Figure 5.23 and Table 5.3 present a comparison of measurement discrepancies across four distances using manual and automatic methods. The box plots in Figure 5.23 shows a symmetrical distribution of measurement differences around the zero line, with varying degrees of spread indicated by the range and outliers. Overall, the mean discrepancy is slightly over 1 mm with a variability of about 2.8 mm, suggesting generally reliable measurements but with some inconsistency.

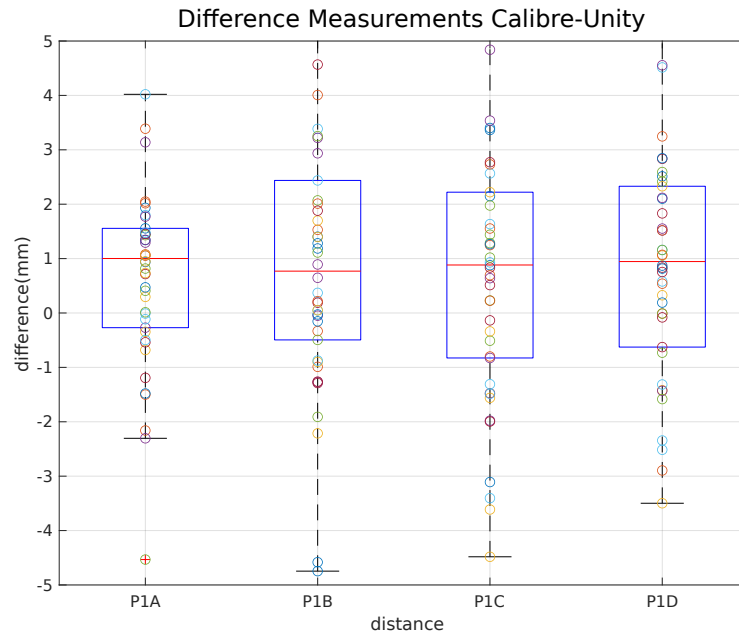


Figure 5.24: Calibre Acquisition (N=14 for each distance)

	P1A	P1B	P1C	P1D
Target 1				
Mean(mm)	74.4131	58.7775	107.3100	99.3713
SD(mm)	9.1665	7.6660	7.8223	5.9066
Target 2				
Mean(mm)	60.5369	44.3256	111.8894	104.1269
SD(mm)	9.1201	5.2156	8.2620	7.4262
Target 3				
Mean(mm)	105.4067	96.3133	68.1333	54.8425
SD(mm)	8.2539	5.9870	9.0475	8.6717

Table 5.4: Calibre Measurements for Different Targets

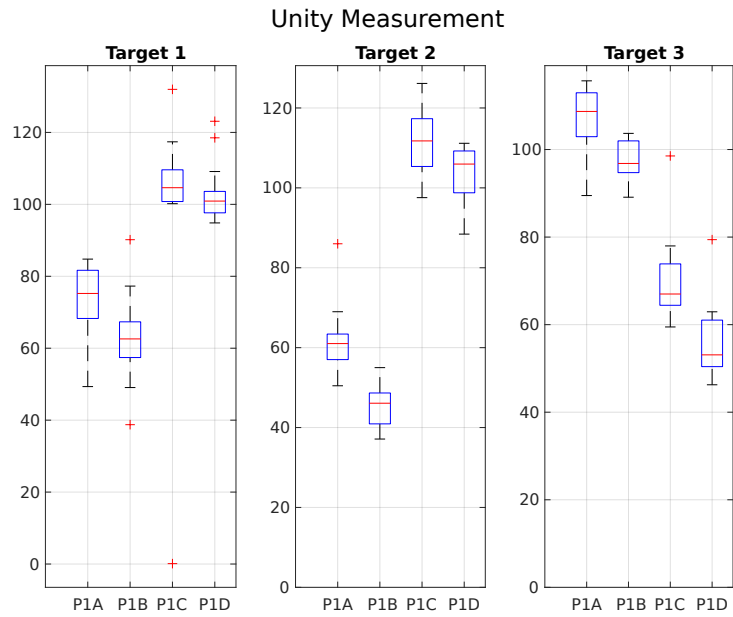


Figure 5.25: Automatic Acquisition (N=14 for each distance)

	P1A	P1B	P1C	P1D
Target 1				
Mean	73.2955	62.9820	101.0337	102.7532
SD	11.1214	11.4350	28.1838	8.0359
Target 2				
Mean	61.4079	45.4857	111.1676	103.6486
SD	8.1554	5.7060	7.8350	7.1330
Target 3				
Mean	106.9182	97.6741	70.1779	55.9618
SD	7.9098	4.5811	10.4177	9.1831

Table 5.5: Automatic Measurements for Different Targets

Comparing the two cases:

- The mean measurements for both calibre and automatic system are similar, with some variations across the targets and distances.
- The standard deviations for calibre measurements tend to be higher at shorter distances (P1A, P1B) and lower at longer distances (P1C, P1D), indicating more precise measurements at longer distances.
- For automatic measurements, the standard deviations are generally lower than calibre measurements, except for a spike at P1C across Targets 1 and 2, suggesting an issue with measurement consistency at that particular distance.
- The variability in measurements, as shown by the standard deviation, is a crucial factor that might affect the selection of measurement methods in practice.

Both measurement methods demonstrate variability, with unity measurements generally showing less variability except at certain distances where precision drops.

5.2 Data Testing Analysis

The evaluation encompassed a cohort of 18 participants who completed 47 distinct phases, collectively amounting to 7.6 hours. During this period, they performed 141 actions deemed as Estimated Correct Position (ECP) across a total of 182 Positioning Attempts (PA).

5.2.1 Duration

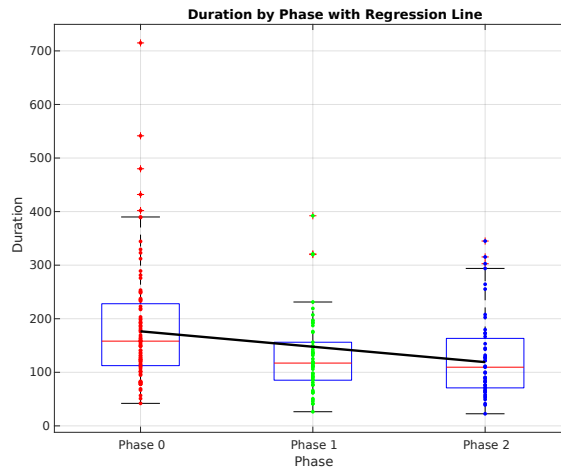


Figure 5.26: Duration by Phase with Individual Data Points (Phase 0 (N=33); Phase 1 (N=23); Phase 2 (N= 6))

	Phase 0	Phase 1	Phase 2
Mean (s)	185.10	130.54	127.62
SD (s)	113.90	72.26	78.84

Table 5.6: Statistical Duration Measures for Each Phase (Phase 0 (N=33) Phase 1 (N=23); Phase 2 (N=6))

The graph (Figure 5.26) and table 5.6 presented depict the duration of the three different phases. Box plots are overlaid with individual data points for Phases 0, 1, and 2. The regression line plotted across the phases indicates a decreasing trend in duration as we move from Phase 0 through Phase 2. It suggests that there might be a systematic reduction in duration, although the presence of outliers, especially in Phase 0. Furthermore, Phase 0 has the highest mean duration at 185.10 s and the greatest standard deviation at 113.90 s, indicating significant variability in

that phase. Phase 1 and Phase 2 have lower mean durations, 130.54 and 127.62 s, respectively, with Phase 1 having the least variability, as shown by the smallest standard deviation of 72.26 s. Phase 2 shows a slight increase in standard deviation (78.84 s) compared to Phase 1, suggesting a slight increase in variability.

5.2.2 Radiation Picture Counts

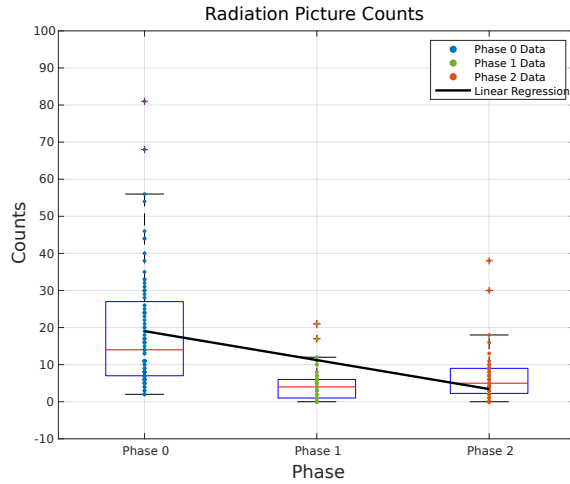


Figure 5.27: Radiation Picuter Counts. (Phase 0 (N=33) Phase 1 (N=23); Phase 2 (N= 6))

Table 5.7: Radiation Picture Counts Across Different Phases (Phase 0 (N=33) Phase 1 (N=23); Phase 2 (N= 6))

	Phase 0	Phase 1	Phase 2
Mean	22.22	4.87	6.60
SD	26.47	5.09	7.23

Figure 5.7 shows the distribution of radiation picture counts in the three separate phases (Phase 0, Phase 1, Phase 2). From Phase 0 to Phase 2, there is a general decrease in radiation picture counts, with Phase 1 having the lowest counts and the least variability. Phase 2 shows a slight increase in both mean counts and variability compared to Phase 1. The linear trend line indicates that, overall, there is a decrease in radiation picture counts across the phases.

5.2.3 Anatomical

Brachial Artery

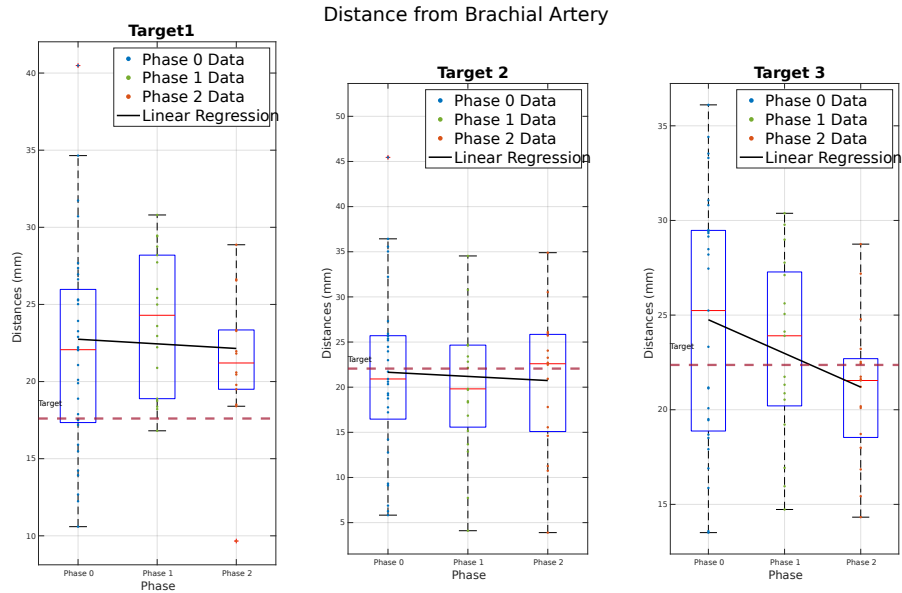


Figure 5.28: k-Wires implanted distance from Brachial Artery (Phase 0 (N=33); Phase 1 (N=23); Phase 2 (N= 6))

Figure 5.28 includes box plots depicting the distance from the brachial artery at three different targets over three phases.

- Target 1: The mean distance increases from Phase 0 to Phase 1, then decreases in Phase 2, with standard deviations decreasing across phases, indicating more consistent measurements in later phases.
- Target 2: There's a slight decrease in the mean distance from Phase 0 to Phase 1 and a more significant decrease to Phase 2. The standard deviation peaks in Phase 1, indicating the greatest variability in this phase.
- Target 3: Shows a decreasing mean distance from Phase 0 through Phase 2 with the standard deviation decreasing as well, suggesting increasing measurement precision.

Table 5.8: Distance from Brachial Artery ((Phase 0 (N=33) Phase 1 (N=23); Phase 2 (N=6)))

	Phase 0	Phase 1	Phase 2
Target 1			
Mean (mm)	21.98	23.97	21.38
SD (mm)	6.80	4.54	4.64
Target 2			
Mean (mm)	21.57	21.35	20.66
SD (mm)	9.61	10.26	7.95
Target 3			
Mean (mm)	24.65	23.18	21.10
SD (mm)	6.75	4.83	3.80

Distance measurements from the brachial artery across different phases show variability, with general trends towards decreasing distances in later phases. Variability decrease from Phase 0 to Phase 2 for Targets 1 and 3, which might suggest improved measurement techniques or conditions over time. The linear regression lines in the box plots suggest that while there is a trend of distance decreasing over phases for all targets, the rate of change and variability are not consistent across targets.

Median Nerve

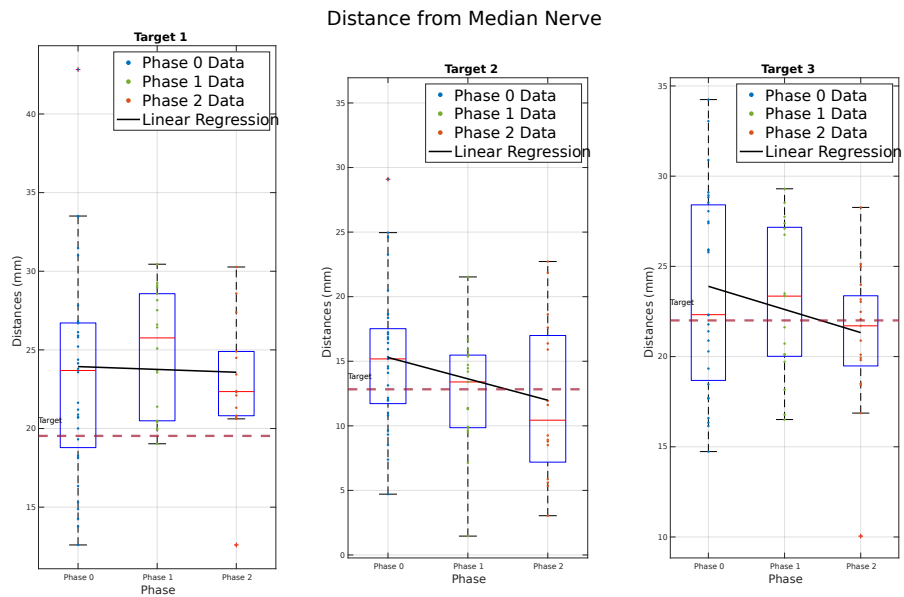


Figure 5.29: k-Wires implanted distance from Median Nerve(Phase 0 (N=33); Phase 1 (N=23); Phase 2 (N=6))

The box plots in Figure 5.29 depicts the distance from the Median Nerve for three different targets across three phases.

- Target 1: the mean distance slightly increases from Phase 0 to Phase 1 and then decreases in Phase 2. The standard deviation is highest in Phase 0 and lowest in Phase 1.
- Target 2: shows a consistent decrease in mean distance from Phase 0 through Phase 2, with the standard deviation peaking in Phase 1.
- Target 3's mean distance also decreases across the phases, with the standard deviation decreasing slightly, indicating more consistent measurements over time.

Table 5.9: Distance from Median Nerve ((Phase 0 (N=33) Phase 1 (N=23); Phase 2 (N= 6)))

	Phase 0	Phase 1	Phase 2
Target 1			
Mean	23.35	24.93	22.99
SD	6.66	3.90	4.28
Target 2			
Mean	15.31	13.61	12.00
SD	5.54	6.75	6.14
Target 3			
Mean	23.71	22.99	21.14
SD	5.58	4.20	4.03

Overall, the trend observed suggests that distances from the Median Nerve generally decrease over the phases for Targets 2 and 3, while Target 1 shows a slight fluctuation. The standard deviations tend to decrease from Phase 0 to Phase 2 for Targets 1 and 3, indicating more precise measurements as the phases progress. For Target 2, the highest variability occurs in Phase 1.

Ulnar Nerve

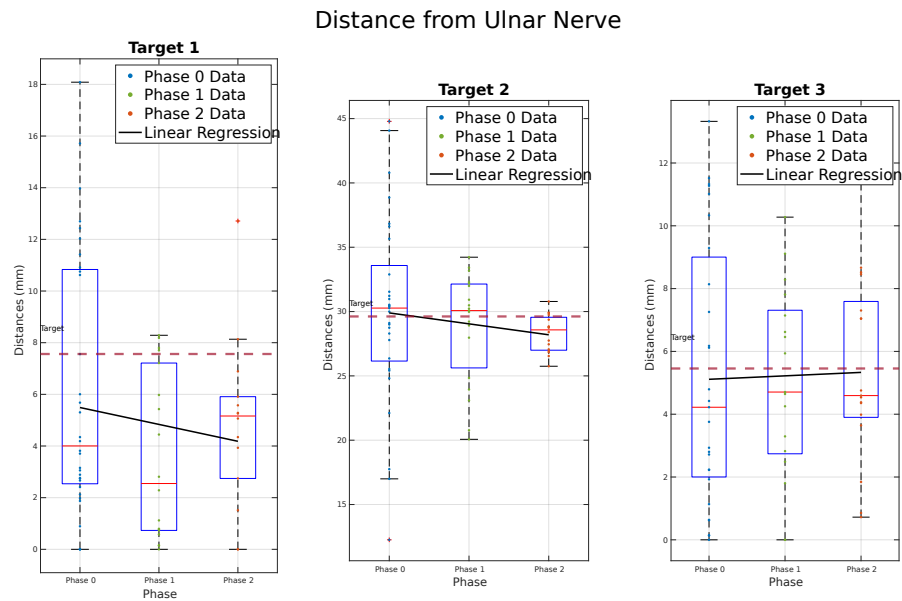


Figure 5.30: k-Wires implanted distance from Ulnar Nerve (Phase 0 (N=33) Phase 1 (N=23); Phase 2 (N= 6))

Figure 5.30 shows box plots for distances from the Ulnar Nerve for three different targets over three phases.

- Target 1: has a mean distance that decreases from Phase 0 to Phase 1 and then increases in Phase 2, with standard deviations indicating a moderate level of variability that doesn't significantly change across the phases.
- Target 2: shows a mean distance that decreases slightly across the phases, with a marked decrease in standard deviation from Phase 0 to Phase 2;
- Target 3: the mean distance initially decreases slightly from Phase 0 to Phase 1 and then increases in Phase 2, with a corresponding decrease in standard deviation;

Table 5.10: Distance from Ulnar Nerve (Phase 0 (N=33) Phase 1 (N=23); Phase 2 (N= 6))

	Phase 0	Phase 1	Phase 2
Target 1			
Mean	6.12	3.58	4.81
SD	5.07	3.24	3.31
Target 2			
Mean	30.00	28.83	28.30
SD	7.41	4.28	1.45
Target 3			
Mean	5.20	5.04	5.42
SD	4.20	3.05	2.96

The trends observed suggest that for Target 2, there is a consistent improvement precision (standard deviation) of insertion. Target 1 and Target 3 demonstrate minor fluctuations in standard deviation. with a general trend of improved precision.

Chapter 6

Discussion

This thesis examines the creation and validation of an AR image-guided surgery system in orthopaedics field. It explores the system's development and analyzes the efficacy of current AR technologies in enhancing surgical procedures.

6.1 System Development Principles

From a software-hardware design perspective, the goal was use alone Hololens 2, as development platform. It potentially can integrate the tracking and guidance systems into a single device. However, research indicates that despite having the requisite sensors, processors and display units, it wasn't fit for the intended use. A modular approach across hardware and software platforms appears to be the most suitable solution.

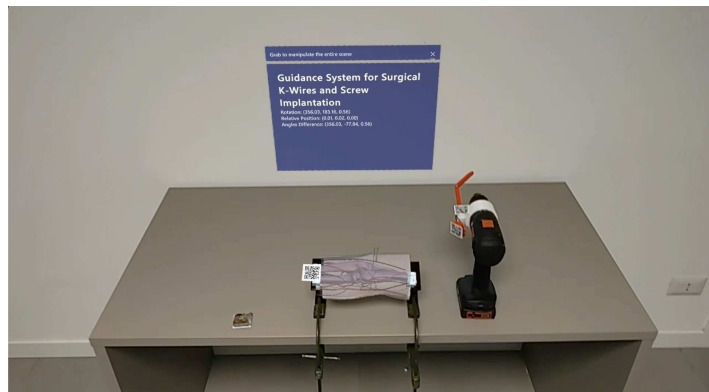


Figure 6.1: Augmented Reality Environment from HMD

6.1.1 Hologens integrated System

As reported in our work "*Mixed Reality for Orthopedic Elbow Surgery Training and Operating Room Applications: A Preliminary Analysis*"[69] it is possible to develop a readily available Hologens 2 system. To mediate the correspondence between the real and virtual worlds, QR code tracking was used. This was integrated into the Hologens platform via Vuforia and MRTK packages.



Figure 6.2: QR code for phantom and guide tracking and related features.

Vuforia is an augmented reality platform equipped with an SDK tailored for AR application development. Features for detection and tracking are extracted uploading the *Image Targets* to the Vuforia Development Portal (refer to Figure 6.2). In Hologens 2, these are detected by the RGB sensor. Tracking performance improves when targets are: (1) rich in detail; (2) high in contrast; (3) free from repetitive patterns; (4) in the correct format. In Hologens, they enable the coherent overlay of 3D virtual models onto physical spaces.



Figure 6.3: QR tracking and models superimposition

However, the computational cost did not permit effective tracking for the intended purpose. Specifically, initial recognition times were notably high. The

literature presents various works utilizing different types of QR codes, including ArUCOs, VuMarks, ARToolkit [70]. While these demonstrate varying characteristics and recognition times, they are unsuitable for the intended purpose. The potential improvement did not align with the project's objectives.

Additionally, to occur recognition the camera had to be positioned in a specific relative position from the marker. This is often proved incompatible with surgical gestures limiting the comfort use. It may be results challenging in a surgical context during the insertion of screws and k-wires. Occlusion zones, excessive distance of the tracking object from the camera and environmental conditions (brightness, scene crowding, etc.) are the main problems detected.

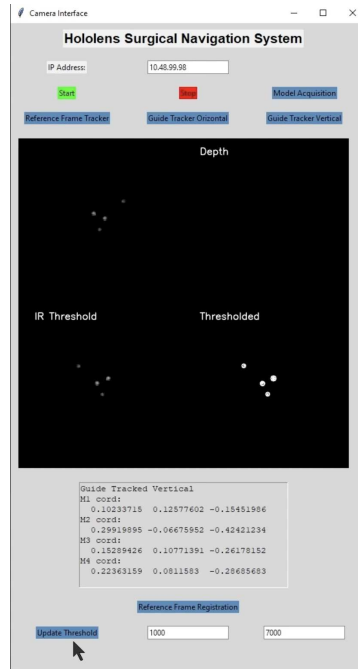


Figure 6.4: Communication Interface for coordinates estimation with Hololens IR Camera

The framework described in Chapter 2 was adapted to Hololens 2 to reduce computation costs. Using the "*HoloLens 2 Sensor Streaming [71]*" package the built-in IR camera is utilized as a capture sensor, transferring data via Wi-Fi to an IP address on the local network. With this setup, markers were accurately recognized, but the output coordinates exhibited local variability. This variability hindered the stable determination of the tracking tool's pose.

6.1.2 Modular System Development

Acquisition Module

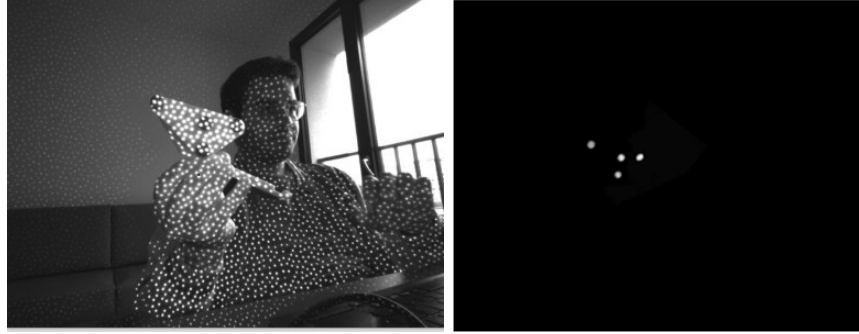


Figure 6.5: Realsense Depth Camera and Kinect Spherical Marker Acquisition comparison

The framework requires a depth camera to capture 3D scene coordinates. *Kinect Azure DK* and *Intel RealSense i435* are two viable options, each employing distinct technologies. The Kinect Azure DK was selected for its time-of-flight camera at wavelengths beyond the visible spectrum. Otherwise the Intel RealSense, which utilizes structured light technology, not acquire selectively markers reflected light (Figure 6.5).

The Kinect Azure DK supports both Near-FOV and Wide-FOV acquisition modes, offering a broader range of capture. Additionally, with the binned mode measurements are possible over greater distances, at the expense of lower resolution. This enabled a relatively wide acquisition field, increased flexibility in camera positioning relative to the setup and reduced occlusion zones.

Table 6.1: Comparison of Kinect Azure DK and Intel RealSense D435i

Category	Kinect Azure DK	Intel RS D435i
Technology	Time of Flight	Stereoscopic
Mode	WFOV 2x2 binned	NFOV
Resolution	512x512	1280 × 720
FOV	120° × 120°	87° × 58°
FPS	0, 5, 15, 30	Up to 90
Range	0.25 - 2.88 m	0.3 m - 3 m

Circle Detection

Independently from the orientation, slicing through a sphere always results in a circle. Utilizing this concept a circle detection algorithm to the processed images to identify potential circles is used. For circle detection, two types of algorithms can be used. One type fits a circle to the detected circular edge points. Examples include: Ray Circle Detector (RCD) and Hough Transform. The other type finds the center of gravity of a binary region. Examples of this are Maximally Stable Extremal Regions (MSER) and Detection and Filtering of Binary Large Objects (BLOBs).

Table 6.2: Comparison of circle detection algorithms.

Algorithm	Detection error (pixel)		Detection error (mm)		Avg. Time (ms)
	Left image	Right image	Left image	Right image	
RCD	1.20	1.41	0.08	0.10	3.42
HOUGH	1.59	2.24	0.11	0.16	1.51
BLOB	1.35	1.00	0.09	0.07	1.43
MSER	1.01	0.00	0.07	0.00	153.43

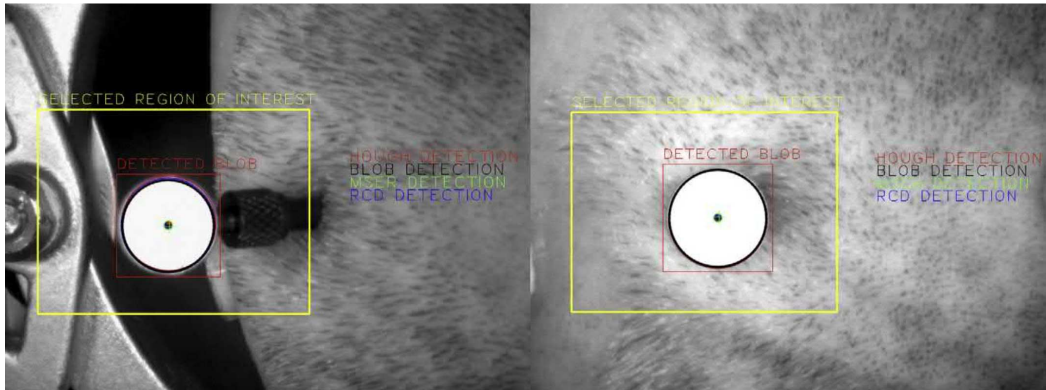


Figure 6.6: Assessing circle detection algorithms during surgery

Following the work of Šuligoj et Al. [72] circle are identified in images using the Circular Hough Transform (CHT). It has its performance in noisy environments, with occlusions and varying light intensities. As reported by Jerbić et Al. the MSER algorithm demonstrated the highest accuracy. However, the poor processing speed precluded its use in real-time patient localization [73].

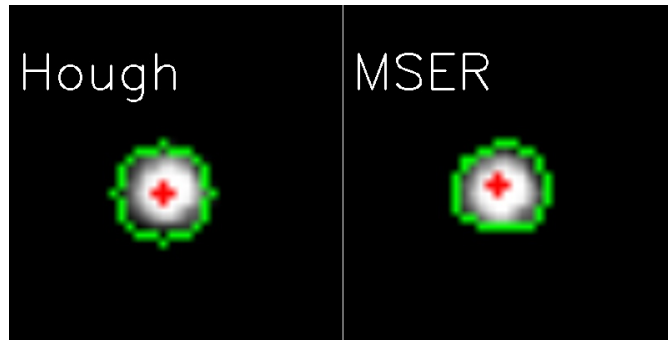


Figure 6.7: Assessing circle detection algorithms during surgery

The figure 6.8 shows a ROI in a IR image acquire with the described setup. The MSER and Hough algorithms are implemented with OpenCV. While Hough's algorithm, which focuses on the center, involves constructing a circumference, the MSER algorithm, in contrast, identifies the center of the sphere associated with the centroid based on the contours of the detected circle or ellipse. In the suggested setup, the execution times of both algorithms are similar (Table 6.4).

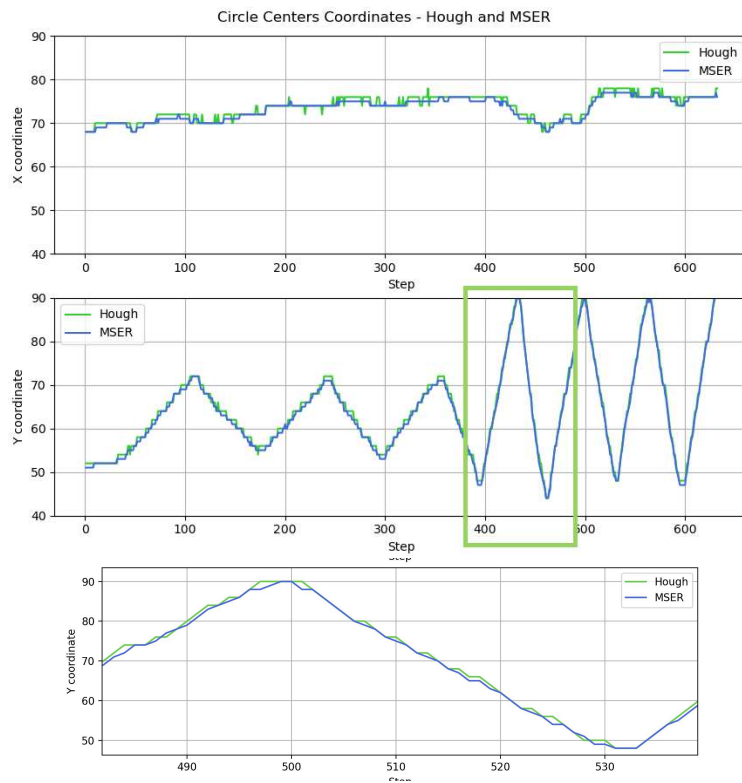


Figure 6.8: Center Circle Coordinates in Circle Detection - Hough and MSER

As can be seen in Figure 6.8 , the centre coordinates provided by MSER are smoother than those provided by Hoguh. Despite this, the MSER algorithm is less flexible than Hoguh. In fact, when varying the contrast or threshold to binarise the image, Hoguh is more robust. This is important as the environment in which this setup is used is highly subject to variations in lighting conditions that could interact with the ability of passive markers to reflect light.

Table 6.3: Mean Processing Times for Circle Detection (632 frames)

Mean Processing Time	
MSER	0.767 ms
Hough	0.662 ms

Matching Problem Solutions

Several methods have been analyzed to solve the matching problem, among which the Optimal Transport Theorem and Procrustes Analysis were found to be the most effective. The Optimal Transport theory [74] provides a more efficient implementation. It use around one-quarter the computing time per iteration as Procrustes analysis (2.16ms) on the same Apple M1 unit. Despite its straightforward implementation, it was subject to ambiguities in detection, especially when the tracking tool was placed in an orientation different from the model ones.

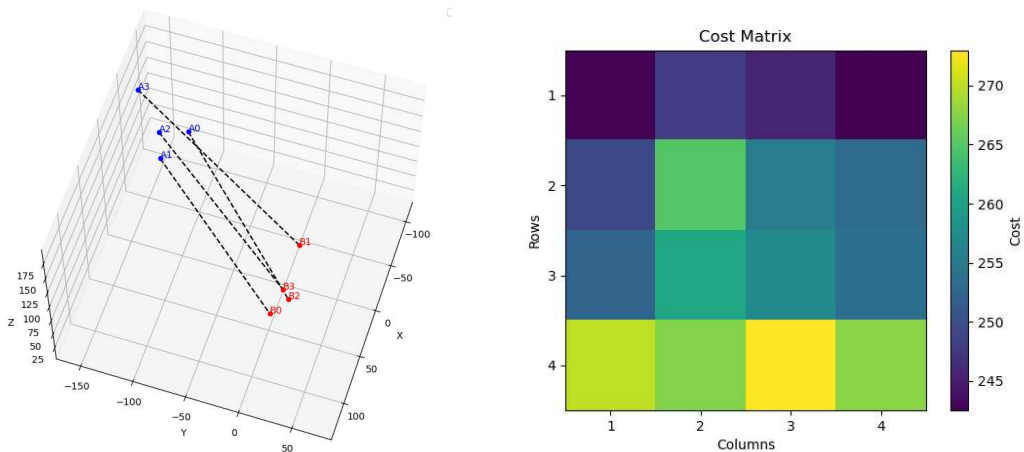


Figure 6.9: Application of the Optimal Transport Theorem between two sets of points. The cost matrix used to calculate the transport plan is shown on the right.

Procrustes Analysis, on the other hand, requires an iterative calculation on the image, which increases the computational cost. However, it effectively solves the problem of marker recognition ambiguity caused by orientation changes. In this method, each marker combination is rotated and shifted to minimize the distance between the model markers and the detected ones.

Table 6.4: Mean Processing Times for Matching Problem Resolution

Mean Processing Time	
OPT	0.58 ms
Procrustes	2.61 ms

6.1.3 System Criticism and Development Advancements

During the development and evaluation process of the developed system critical aspects were identified. The application of neural network are strategic points of improvements, which are expected to refine the system's accuracy and adaptability.

Points of improvement

- Acquisition System and Compatibility:
 - The augmented reality platform requires a specific setup, conflicting with the original aim to condensate multiple functions into a single device, like the Hololens.
 - A specific type of acquisition unit is needed at the current stage of development. Alternative depth cameras, such as Intel RealSense, are incompatible with the designated framework. The need for specific acquisition devices highlights the importance of developing more flexible compatibility standards.
- Potential Improvements and Accuracy:
 - The framework can be refined by adopting new computer vision techniques and modeling methods to enhance accuracy.
 - The system currently works in two phases: establishing a reference frame and tracking the navigation tool. User-induced instability can cause errors; the aim is to accurately track each tool in real-time.
 - Spheres used for recognition and virtualization may compromise quality by introducing errors.

- The system’s assumption of body rigidity is not always valid, as shown by the deflection of some tools in use, such as the k-Wire tip.
- User Interface Optimization:
 - The system needs improvements to ease use, as current complexity increases cognitive load during pre-testing. To decrease cognitive load, interactions should be simplified, and the user interface improved with intuitive guides to facilitate learning and usage.

CNN tracking system pipeline development

Several improvement points, previously mentioned can be addressed through the use of neural networks. These allow frames acquisition in the visible spectrum with a higher resolution. Additionally, specifically trained neural networks capable of determining the position of an object directly from the frame. As demonstrated below, it is also possible to obtain information on the deformation elements state. For example, the tip of a k-Wire can be identified, and its deformation state can be associated with it.

The use of neural networks within the framework facilitates the reintroduction of the idea of using Hologens as all-in-one platform. This device is equipped with four grayscale cameras that cover the frontal and lateral areas of the Hologens, for which the intrinsic and extrinsic parameters are known for each device. By recognizing an object and applying the Pinhole Camera model, it is possible to determine its position in space.

Data Acquisition Data for neural network training were sourced from a cellphone camera and Hologens 2 grayscale cameras. Three datasets were assembled:

- **First training dataset:** Images from a cellphone with IR sphere segmentations on a guide.
- **Second training dataset:** Images from a smartphone, including segmentations of IR spheres on a guide and k-Wire.
- **Third training dataset:** Images from an external camera combined with grayscale captures from Hologens, with IR sphere segmentations on a guide.

Data Extraction Data was extracted at 3 frames per second from both videos to capture various orientations and environmental conditions for training and testing.

Segmentation Process MATLAB's Image Segmenter was utilized for manual segmentation. For external camera images (in RGB), circular ROIs were outlined, binarized, and saved in .jpg format. To enhance the visibility of spheres in grayscale Hololens images, filters such as image equalization and CLAHE were applied. "PaintBrush" and "active contours" were used for k-Wire segmentation.

Dataset Subdivision The dataset is split into a training set (70%), a validation set (20%), and a test set (10%).

Data Augmentation For the first two training sessions, the following Data Augmentation settings were used:

```

1 image_datagen = ImageDataGenerator(rotation_range = 180,
2                                     width_shift_range = 0.2,
3                                     height_shift_range = 0.2,
4                                     horizontal_flip = True,
5                                     vertical_flip = True,
6                                     fill_mode = 'reflect')
```

For the third training session, after the 37th epoch, the following Data Augmentation settings were added:

```

1 image_datagen = ImageDataGenerator(rotation_range = 360,
2                                     width_shift_range = 0.8,
3                                     height_shift_range = 0.6,
4                                     horizontal_flip = True,
5                                     vertical_flip = True,
6                                     fill_mode = 'reflect',
7                                     rescale=1.5,
8                                     channel_shift_range=0.3)
```

The initial two training sessions were executed utilizing RGB color mode, whereas the third session employed Grayscale mode.

Network Training The network employs ResNet34 with ImageNet pre-trained weights for feature extraction. The encoder is frozen to focus on segmentation learning. The decoder uses "transpose" blocks for feature upsampling. It processes 512x512 pixel images, outputting a segmentation mask for specified classes (NUM_CLASSES) using a sigmoid activation.

```
1 BACKBONE = 'resnet34'  
2 model = Unet(backbone_name=BACKBONE,  
3             input_shape=(512, 512, 3),  
4             encoder_weights='imagenet',  
5             encoder_freeze=True,  
6             decoder_block_type='transpose',  
7             classes=NUM_CLASSES,  
8             activation='sigmoid')
```

A learning rate of 0.0001 was used for all datasets; for a number of epochs of 150, 250 and 87 respectively.

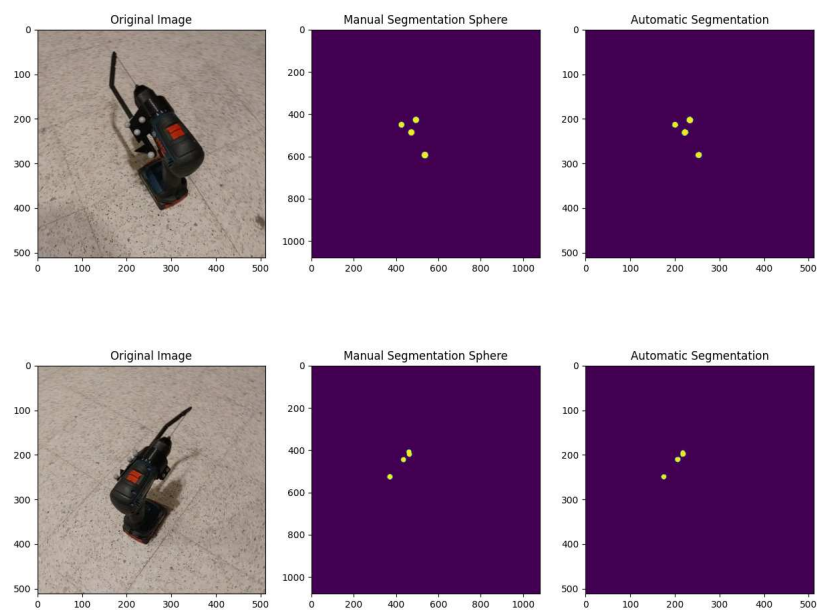


Figure 6.10: Test Set - First Training

Inference times averaged across all cases are:

- 300 ms with IntelCore i7 9th Gen CPU;
- 30 ms with RTX 2080 GPU with Max-Q Design.

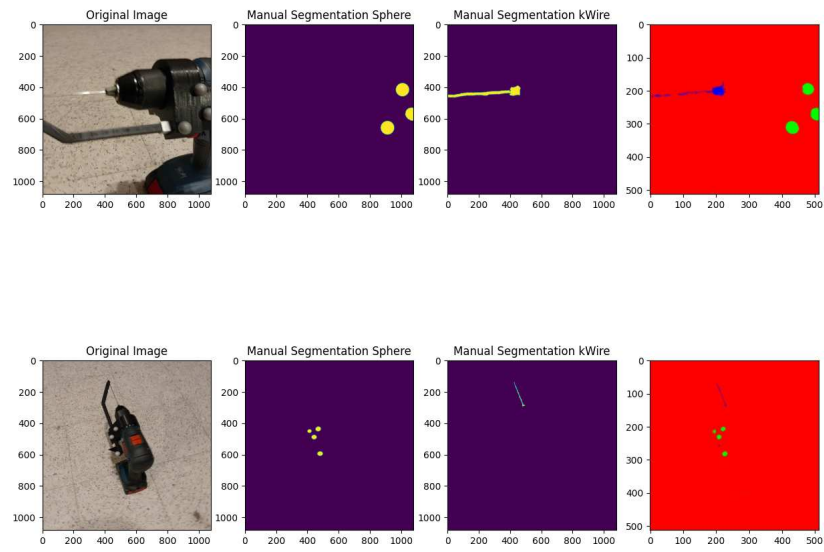


Figure 6.11: Test Set - Second Training

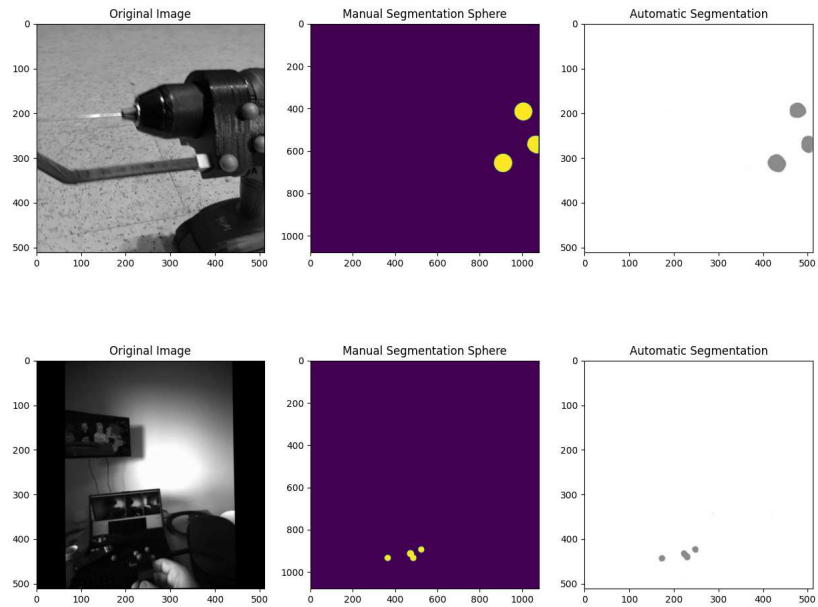


Figure 6.12: Test Set - Third Training

Triangulation in Space In the HoloLens 2, sensors are positioned within a device-defined coordinate frame known as the rigNode. Each sensor provides its transformation relative to the rigNode using a rigid extrinsic transformation, which includes rotation and translation. The origin within the device is set at the Left Front Visible Light Camera, which is defined by an identity transformation. By calculating the camera's intrinsic parameters and correlating the centers of the spheres detected in the frame with known points in the real world, it is possible to estimate the camera's extrinsic parameters.

```

1 camExtrinsics = estimateExtrinsics(centers, worldPoints,
  cameraIntrinsics);
2 camPose = extr2pose(camExtrinsics);

```



Figure 6.13: Frames and Sphere IR segmentation

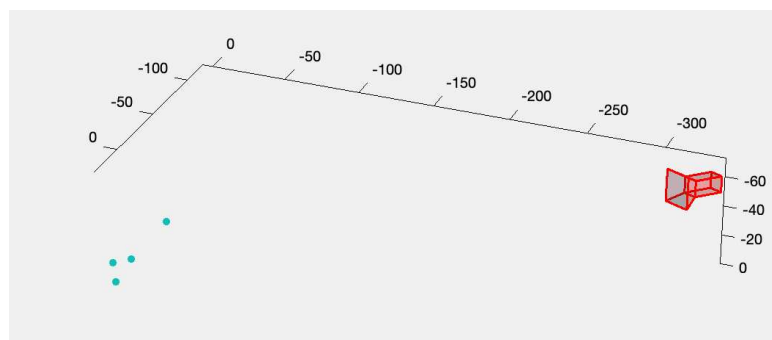


Figure 6.14: Points triangulation in Space

6.2 Results

6.2.1 System Performance Data Analysis

Point's relative location in a coordinate system

To evaluate the relative positions of points within the reference system, the fiducial marker was established as the system's origin point. Depending on the relative position of the fiducial markers on the stand, there is a different distribution of the acquired points in the (x,y) plane. In particular, markers closer to the camera tend to distribute around the origin co-ordinate; while markers that are further away are characterised by an offset. The relative position recorded on the z-axis remains approximately the same for all points.

Mean and standard deviation of error between recorded and expected positions as distance changes, it maintain a nearly constant value. Decomposing the error into its individual components errors in the x and y dimensions consistently exceed the error in the z dimension. This pattern confirms higher sensor measurement errors in the x and y components, while indicating greater accuracy in the z dimension.

The analysis indicates consistent error across tool poses; however, 'Tool Pose 5', which is inclined at 45 degrees, shows a higher error, possibly as a result of greater distortion in the image.

Repeatability of single-point coordinate

The goal of "*Repeatability of single point coordinates*" is to confirm consistent coordinate acquisition at a specific point. Here, the reference point is the average of the acquired coordinates. The deviation is calculated from this average, with no link to the sensor's distance. Generally, z deviations are smaller than x and y, but at greater distances (50 cm and 60 cm), z deviation aligns with x and y.

Relative point to point accuracy

The "*relative point-to-point accuracy*" is assessed by comparing distances to fiducial points and analyzing measurements obtained from calipers and automatic methods. Fiducial markers coordinates are associated with the graphical model, while the measurements acquired with the caliper are in relation to the physical model. This allows a direct comparison between measurements in virtual space and physical ones.

The fiducial points distances analysis reveals two correlations. As the distance between the two points increases, the registration error increases. Whereas as the

distance of the acquisition setup increases, the average error and standard deviation decreases. This can be attributed to using the camera in WFOV mode, whereby the optical distortion is greater for shorter distances. At a distance of 60 cm, the error decreases to 0.34 mm.

Comparing automatic and manual measurements the means difference range from 0.8783 mm to 1.4030, while the standard deviations, ranges from 2.3243 mm to 3.6618 mm. The an overall mean differences is of 1.022 mm with a standard deviation of 2.8217 mm. Furthermore, the measurements standard deviation across targets (characterized by different positions on the dummy) between the automatic and gauge measurements is nearly identical. This highlights the automatic system's capacity for consistent measurement reproduction. However, it does not offer any insights into the system's accuracy.

The comparison of the two methods shows similar deviations, with offset at individual points that barely affect distance calculations. This is crucial for the distances based virtualization system used to assess the impact of the implanted k-Wire. Caliper measurements lead to a greater systematic error than automatic measurements. Therefore, it is decided to consider the measurement obtained with the tracking system to be more reliable. Furthermore, the relative errors obtained are sufficiently acceptable for the automatic measurement to be considered sufficiently accurate and precise.

6.2.2 Data Testing Analysis

Duration

The data in Figure 5.27 indicates that the integration of Augmented Reality (AR) in Phases 1 and 2, as opposed to using only an X-ray simulator in Phase 0, results in a decrease in the time taken for k-Wire insertions into an elbow phantom. Despite this time reduction, the variability in duration increases slightly in Phase 2. This suggests that while AR aids efficiency, its application may introduce inconsistencies, may be due to increased precision often exercised in repetitive task execution and the potential onset of fatigue due to continuous testing. The overall trend, indicated by the regression line, points to improved efficiency with AR, but the presence of outliers suggests that individual experiences can vary significantly.

Radiation Picture Counts

The transition to AR guidance in orthopedic surgery, as evidenced by graphs 5.27 and Table 5.7, has resulted in a decrease in Radiation Picture Counts (RPCs), which implies a reduced need for intraoperative X-ray imaging. This reduction is

beneficial, considering the potential health implications of radiation exposure for both patients and surgical teams.

Anatomical

The analysis of distances from the brachial artery, median and ulnar nerves to three targets in different phases suggests that the use of Augmented Reality (AR) in Phases 1 and 2 improves accuracy compared to Phase 0, which only used an X-ray simulator. The trend lines indicate that distances in Phases 1 and 2 are closer to the target, implying that AR aids in precise targeting. The standard deviations decrease from Phase 0 to Phase 2, showing increased consistency with the integration of AR. The varying degrees of improvement across targets highlight that while AR generally enhances precision, its efficacy may differ based on the target's specifics. Overall, AR appears to contribute positively to both the accuracy and consistency of reaching the target distances in surgical procedures.

Chapter 7

Conclusion

This master's thesis introduces and evaluates a system that merges image-guided surgery (IGS) with augmented reality (AR) to boost the precision and safety of orthopedic surgeries, particularly for the elbow, aiming to lessen nerve damage and reduce X-ray exposure.

The dual-component system developed within this work —the tracking system and the X-ray simulation coupled with AR guidance— represents a leap towards modernizing surgical procedures. Through real-time, accurate tool positioning based on a virtual anatomy model, it potentially may reduce conventional surgery risks. Furthermore, the testing protocol and data analysis affirm the system's efficacy in improving surgical outcomes through enhanced precision, reduced operation time and radiation dose. It is fundamental consider their direct correlation with potential saving healthcare costs.

The AR's role in improving K-wire placement accuracy is highlighted by the results obtained, but a critical selection of the targets is crucial to minimize risks. However, advancements in real-time, precise tracking algorithms for surgical tools and anatomy, and algorithms that can differentiate tissues, pinpoint anatomical landmarks, and anticipate surgical hurdles, are needed to boost safety and effectiveness.

Overcoming data interoperability and real-time computing challenges is essential for these technologies' success in surgery, requiring standardized data integration protocols and fast processing for real-time guidance. Incorporating machine learning (eg. CNNs) and innovative computer vision techniques, could significantly enhance technology integration in future surgical procedures.

Appendix A

Protocol tables

phase 1 TEST – AR first time

Step	Instruction	Time
1	candidate wears the AR headset and is instructed on the tool	60 sec
2	candidate performs ocular calibration of the AR headset	60 sec
TOTAL TIME		≈ phase 0 TEST duration + 2 min

Table A.4: The above reports steps to perform in addition to phase 0 to perform a phase 1 test; Note that time is just an estimate

Step	Instruction	Time
1	Phantom is setup	60 sec
2	Candidate is showed the drill, kwire and explained how to use it	30 sec
3	Candidate is showed the virtual xray machine and explained how to use it	30 sec
4	Candidate is showed the mannequin and a brief description of what is inside	60 sec
5	Candidate is advised to utilize the x-ray machine to the extent they deem necessary	10 sec
6	The candidate is requested to perform a trial of the drill on a phantom to build assurance or confidence	60 sec
7	Candidate is shown target position of 3 Kwires and is given a printed paper with ortogonal xray view of them	120 sec
8	Candidate is instructed that when the test begins he/she will have to place 3 Kwire in 3 different positions, he/she will have the possibility to extract it and reposition it after manual/xray inspection and data registration of the data collector	20 sec
9	Candidate data is recorded on "AR kwire placement test companion"	60 sec
TEST BEGINS		
10	ECP 1	check ECP steps table
11	ECP 2	check ECP steps table
12	ECP 3	check ECP steps table
TEST ENDS		
13	Candidate leaves the room	30 sec
14	Technical phantom check	20 sec
TOTAL TIME		$\approx 10 \text{ min} + (\text{ECP time} \times 3)$

Table A.1: Preparatory and test steps

ECP step	Instruction	Time
ECP BEGINS		
1	PA 1	check PA steps table
2	PA 2	check PA steps table
3	... more PA until satisfactory position is reached by the candidate	check PA steps table
ECP ENDS		
4	ECP data collection	10 sec
TOTAL TIME		$\approx 10 \text{ sec} + (\text{PA time} \times 2..4)$

Table A.2: ECP steps

PA step	Instruction	Time
PA BEGINS		
1	Kwire is mounted on the drill by the director	20 sec
2	Kwire is positioned	20 sec
3	candidate analyzes Kwire position with available tools	20 sec
4	Kwire position is measured, computed and registered on database	100 sec
5	Kwire is extracted	10 sec
PA ENDS		
6	PA data collection	10 sec
TOTAL TIME		$\approx 3 \text{ min}$

Table A.3: PA steps

A.1 Acquired Points for Accuracy Evaluation at Different Distances

Table A.5: Points Repeatability at 30cm

Metric	M3	M4	M8	M9
Mean Coordinate (X, Y, Z)	-0.0609, 0.0051, -0.3068	0.0430, 0.0005, -0.3071	-0.0582, 0.0538, -0.5113	0.0464, 0.0474, -0.5088
Std. Dev. Coord. (X, Y, Z)	5.0483 4.0230 3.1133	5.0333 1.0165 1.0785	1.8526 1.0896 0.3765	1.0590 0.5753 1.3641
Min Dist. from Avg. Point	5.6476	3.4459	1.6017	1.1690
Max Dist. from Avg. Point	6.9665	5.5118	2.1231	1.9883
Δx_{\min} (mm)	2.5475	0.3322	0.2085	0.5935
Δx_{\max} (mm)	3.7853	3.3275	1.1753	0.8182
Δy_{\min} (mm)	1.0673	0.6172	0.3525	0.2388
Δy_{\max} (mm)	5.2102	5.2635	1.9702	1.0435
Δz_{\min} (mm)	2.2555	0.1522	0.2795	0.0678
Δz_{\max} (mm)	5.6907	3.8935	1.3647	1.4502

Table A.6: Points Repeatability at 40cm

Metric	M3	M4	M8	M9
Mean Coordinate (X, Y, Z)	-0.034, 0.028 , -0.41	0.068, 0.023, -0.403	-0.019, 0.076, -0.613	0.083, 0.070, -0.605
Std. Dev. Coord. (X, Y, Z)	3.5647, 3.8233, 2.9750	3.0645, 1.2110, 1.8087	0.6820, 2.4792, 1.7256	1.4344, 3.3412, 6.1065
Min Dist. from Avg. Point	3.4578	1.1339	1.1681	2.2817
Max Dist. from Avg. Point	7.9838	5.9306	4.4050	13.5643
Δx_{\min} (mm)	2.0180	0.3277	0.1485	1.0422
Δx_{\max} (mm)	3.3598	1.0272	3.6822	2.7498
Δy_{\min} (mm)	1.7640	0.5543	0.0058	0.7508
Δy_{\max} (mm)	5.2458	1.1062	1.8815	2.6437
Δz_{\max} (mm)	0.1398	1.0892	0.3510	0.9932
Δz_{\min} (mm)	3.3682	1.7357	1.8162	1.5118

Table A.7: Points Repeatability at 50cm

Metric	M3	M4	M8	M9
Mean Coordinate (X, Y, Z)	-0.0454, 0.0459, -0.5017	0.0601, 0.0451, -0.5029	-0.0443, 0.0993, -0.7062	0.0609, 0.0970, -0.7065
Std. Dev. Coord. (X, Y, Z)	2.8427, 2.4848, 0.6925	2.5263, 3.0624, 1.6312	2.7604, 2.4112, 1.4751	6.2537, 2.8096, 2.0906
Min Dist. from Avg. Point	2.1686	0.6488	1.9966	2.5423
Max Dist. from Avg. Point	4.7732	5.3021	5.3985	12.8056
Δx_{\min} (mm)	0.4712	0.6105	0.7170	1.3738
Δx_{\max} (mm)	1.5542	3.0902	2.4307	3.2648
Δy_{\min} (mm)	1.0248	1.6922	0.1807	1.0158
Δy_{\max} (mm)	3.3032	4.1445	1.9753	4.1638
Δz_{\min} (mm)	0.1758	0.2682	0.7637	0.1308
Δz_{\max} (mm)	4.0998	0.5232	3.2617	3.6708

Table A.8: Points Repeatability at 60cm

Metric	M3	M4	M8	M9
Mean Coordinate (X, Y, Z)	-0.0367, 0.0706, -0.6018	0.0662, 0.0681, -0.6008	-0.0317, 0.1243, -0.8062	0.0726, 0.1198, -0.8045
Std. Dev. Coord. (X, Y, Z)	1.4985, 3.3199, 1.4092	1.6209, 2.0340, 1.0310	1.2980, 4.6076, 1.3460	3.8277, 4.6614, 2.8320
Min Dist. from Avg. Point	0.9444	1.4056	1.4486	1.7722
Max Dist. from Avg. Point	6.4172	3.9639	8.7077	8.3707
Δx_{\min} (mm)	0.3980	0.1008	0.5255	0.3982
Δx_{\max} (mm)	1.5520	2.3782	8.6733	1.6552
Δy_{\min} (mm)	0.8520	0.0793	0.4878	0.8060
Δy_{\max} (mm)	2.4540	1.7102	1.7015	4.3978
Δz_{\min} (mm)	1.2240	0.2217	2.0808	0.2200
Δz_{\max} (mm)	6.0800	1.3562	2.7327	1.6628

Bibliography

- [1] G. Antoniadis et al. «Iatrogenic Nerve Injuries». In: *Deutsches Ärzteblatt international* (Apr. 2014) (cit. on p. 1).
- [2] T. Kretschmer et al. «Evaluation of iatrogenic lesions in 722 surgically treated cases of peripheral nerve trauma». In: *Journal of Neurosurgery* 94.6 (June 2001), pp. 905–912 (cit. on p. 1).
- [3] N. Pulos, E. H. Shin, R. J. Spinner, and A. Y. Shin. «Management of Iatrogenic Nerve Injuries». In: *Journal of the American Academy of Orthopaedic Surgeons* 27.18 (Sept. 2019), e838–e848 (cit. on p. 1).
- [4] L. Rasulić et al. «Iatrogenic Peripheral Nerve Injuries—Surgical Treatment and Outcome: 10 Years’ Experience». In: *World Neurosurgery* 103 (July 2017), 841–851.e6 (cit. on p. 1).
- [5] J. D. Stewart. «Peripheral nerve fascicles: Anatomy and clinical relevance». In: *Muscle amp; Nerve* 28.5 (Oct. 2003), pp. 525–541 (cit. on p. 1).
- [6] J. W. SMITH. «Factors Influencing Nerve Repair: I. Blood Supply of Peripheral Nerves». In: *Archives of Surgery* 93.2 (Aug. 1966), p. 335 (cit. on p. 2).
- [7] J. W. SMITH. «Factors Influencing Nerve Repair: II. Collateral Circulation of Peripheral Nerves». In: *Archives of Surgery* 93.3 (Sept. 1966), p. 433 (cit. on p. 2).
- [8] H. J. Seddon. «A Classification of Nerve Injuries». In: *BMJ* 2.4260 (Aug. 1942), pp. 237–239 (cit. on p. 2).
- [9] S. SUNDERLAND. «A CLASSIFICATION OF PERIPHERAL NERVE INJURIES PRODUCING LOSS OF FUNCTION». In: *Brain* 74.4 (1951), pp. 491–516 (cit. on p. 2).
- [10] J. Noble, C. A. Munro, V. S. S. V. Prasad, and R. Midha. «Analysis of Upper and Lower Extremity Peripheral Nerve Injuries in a Population of Patients with Multiple Injuries». In: *The Journal of Trauma: Injury, Infection, and Critical Care* 45.1 (July 1998), pp. 116–122 (cit. on p. 3).

-
- [11] E. W. Kelly and B. F. a. Morrey. «Complications of Elbow Arthroscopy». In: *The Journal of Bone and Joint Surgery-American Volume* 83.1 () (cit. on p. 3).
- [12] G. M. Jeong, S. C. Park, H. H. Kim, and T. K. Lim. «Nerve injury after elbow arthroscopy during the surgeon's learning curve». In: *Arthroscopy and Orthopedic Sports Medicine* 9.1 (May 2022), pp. 13–20 (cit. on p. 3).
- [13] N. F. Hilgersom et al. «Tips to avoid nerve injury in elbow arthroscopy». In: *World Journal of Orthopedics* 8.2 (2017), p. 99 (cit. on p. 3).
- [14] J. G. Alcid, C. S. Ahmad, and T. Q. Lee. «Elbow anatomy and structural biomechanics». In: *Clinics in Sports Medicine* 23.4 (Oct. 2004), pp. 503–517 (cit. on p. 3).
- [15] A. Nourbakhsh et al. «Innervation of the Elbow Joint: A Cadaveric Study». In: *The Journal of Hand Surgery* 41.1 (Jan. 2016), pp. 85–90 (cit. on p. 4).
- [16] X.-H. Yang et al. «Anatomical study of the anterior neurovascular interval approach to the elbow: observation of the neurovascular interval and relevant branches». In: *Folia Morphologica* 79.2 (June 2020), pp. 387–394 (cit. on p. 4).
- [17] R. M. Menorca, T. S. Fussell, and J. C. Elfar. «Nerve Physiology». In: *Hand Clinics* 29.3 (Aug. 2013), pp. 317–330 (cit. on p. 4).
- [18] H. Sharma, G. Taylor, and N. Clarke. «A Review of K-wire Related Complications in the Emergency Management of Paediatric Upper Extremity Trauma». In: *The Annals of The Royal College of Surgeons of England* 89.3 (Apr. 2007), pp. 252–258 (cit. on p. 5).
- [19] N. L. Hochwald, R. Levine, and P. Tornetta. «The risks of kirschner wire placement in the distal radius: A comparison of techniques». In: *The Journal of Hand Surgery* 22.4 (July 1997), pp. 580–584 (cit. on p. 5).
- [20] M. M. Hadeed et al. «Risk factors for screw breach and iatrogenic nerve injury in percutaneous posterior pelvic ring fixation». In: *Journal of Clinical Orthopaedics and Trauma* 33 (Oct. 2022), p. 101994 (cit. on p. 5).
- [21] T. Bage and D. M. Power. «Iatrogenic peripheral nerve injury: a guide to management for the orthopaedic limb surgeon». In: *EFORT Open Reviews* 6.8 (Aug. 2021), pp. 607–617 (cit. on p. 5).
- [22] M. A. Ikram, H. Shahzad, and J. V. Gnanou. «Iatrogenic ulnar nerve palsy associated with supracondylar humeral fracture in children: A systemic review on its management». In: *Trauma* (Sept. 2023) (cit. on p. 5).
- [23] H. Pandit et al. «Improved Fixation in Cementless Unicompartmental Knee Replacement: Five-Year Results of a Randomized Controlled Trial». In: *The Journal of Bone and Joint Surgery-American Volume* 95.15 (Aug. 2013), pp. 1365–1372 (cit. on p. 5).

- [24] L. T. Holly and K. T. Foley. «Intraoperative Spinal Navigation». In: *Spine* 28.supplement (Aug. 2003), S54–S61 (cit. on p. 6).
- [25] Z. Fan et al. «33 - Three-Dimensional Image-Guided Techniques for Minimally Invasive Surgery». In: *Handbook of Robotic and Image-Guided Surgery*. Ed. by M. H. Abedin-Nasab. Elsevier, 2020, pp. 575–584 (cit. on p. 6).
- [26] M. Bydon et al. «Accuracy of C2 pedicle screw placement using the anatomic freehand technique». In: *Clinical Neurology and Neurosurgery* 125 (Oct. 2014), pp. 24–27 (cit. on p. 6).
- [27] Y. Wang et al. «Computed tomography assessment of lateral pedicle wall perforation by free-hand subaxial cervical pedicle screw placement». In: *Archives of Orthopaedic and Trauma Surgery* 133.7 (Apr. 2013), pp. 901–909 (cit. on p. 6).
- [28] N. Dea et al. «Economic evaluation comparing intraoperative cone beam CT-based navigation and conventional fluoroscopy for the placement of spinal pedicle screws: a patient-level data cost-effectiveness analysis». In: *The Spine Journal* 16.1 (Jan. 2016), pp. 23–31 (cit. on p. 6).
- [29] R. G. Watkins, A. Gupta, and R. G. Watkins. «Cost-Effectiveness of Image-Guided Spine Surgery». In: *The Open Orthopaedics Journal* 4.1 (Aug. 2010), pp. 228–233 (cit. on p. 6).
- [30] S. Rajasekaran, S. Vidyadhara, P. Ramesh, and A. P. Shetty. «Randomized Clinical Study to Compare the Accuracy of Navigated and Non-Navigated Thoracic Pedicle Screws in Deformity Correction Surgeries». In: *Spine* 32.2 (Jan. 2007), E56–E64 (cit. on p. 6).
- [31] M. Arand et al. «Qualitative and Quantitative Accuracy of CAOS in a Standardized In Vitro Spine Model». In: *Clinical Orthopaedics and Related Research* 450 (Sept. 2006), pp. 118–128 (cit. on p. 6).
- [32] J. P. Du et al. «Accuracy of Pedicle Screw Insertion Among 3 Image-Guided Navigation Systems: Systematic Review and Meta-Analysis». In: *World Neurosurgery* 109 (Jan. 2018), pp. 24–30 (cit. on p. 6).
- [33] K. T. Foley, D. A. Simon, and Y. R. Rampersaud. «Virtual Fluoroscopy: Computer-Assisted Fluoroscopic Navigation». In: *Spine* 26.4 (Feb. 2001), pp. 347–351 (cit. on p. 6).
- [34] C.-D. Yang et al. «Non-invasive, fluoroscopy-based, image-guided surgery reduces radiation exposure for vertebral compression fractures: A preliminary survey». In: *Formosan Journal of Surgery* 45.1 (Feb. 2012), pp. 12–19 (cit. on p. 6).

- [35] *Handbook of Robotic and Image-Guided Surgery - 1st Edition*. <https://shop.elsevier.com/books/handbook-of-robotic-and-image-guided-surgery/abedin-nasab/978-0-12-814245-5>. Accessed: 2023-12-31. 2023 (cit. on pp. 7, 10).
- [36] S. A. Nicolau, L. Goffin, and L. Soler. «A low cost and accurate guidance system for laparoscopic surgery: validation on an abdominal phantom». In: *Proceedings of the ACM symposium on Virtual reality software and technology*. VRST05. ACM, Nov. 2005 (cit. on pp. 8, 31).
- [37] S. Nicolau, L. Soler, D. Mutter, and J. Marescaux. «Augmented reality in laparoscopic surgical oncology». In: *Surgical Oncology* 20.3 (Sept. 2011), pp. 189–201 (cit. on pp. 8, 31).
- [38] W. S. Khor et al. «Augmented and virtual reality in surgery—the digital surgical environment: applications, limitations and legal pitfalls». In: *Annals of Translational Medicine* 4.23 (Dec. 2016), pp. 454–454 (cit. on p. 8).
- [39] O. Ukimura and I. S. Gill. «Image-Fusion, Augmented Reality, and Predictive Surgical Navigation». In: *Urologic Clinics of North America* 36.2 (May 2009), pp. 115–123 (cit. on p. 8).
- [40] F. A. Casari et al. «Augmented Reality in Orthopedic Surgery Is Emerging from Proof of Concept Towards Clinical Studies: a Literature Review Explaining the Technology and Current State of the Art». In: *Current Reviews in Musculoskeletal Medicine* 14.2 (Feb. 2021), pp. 192–203 (cit. on p. 8).
- [41] P. Pessaux et al. «Towards cybernetic surgery: robotic and augmented reality-assisted liver segmentectomy». In: *Langenbeck's Archives of Surgery* 400.3 (Nov. 2014), pp. 381–385 (cit. on p. 8).
- [42] V. Penza, J. Ortiz, E. DE MOMI, et al. «Virtual Assistive System for Robotic Single Incision Laparoscopic Surgery». In: (2014), pp. 52–55 (cit. on p. 8).
- [43] P. J. Besl and N. D. McKay. «A Method for Registration of 3-D Shapes». In: *IEEE Trans. Pattern Anal. Mach. Intell.* 14 (1992), pp. 239–256 (cit. on p. 8).
- [44] Z. Zhang. «Iterative point matching for registration of free-form curves and surfaces». In: *International Journal of Computer Vision* 13.2 (Oct. 1994), pp. 119–152 (cit. on p. 8).
- [45] A. Sotiras, C. Davatzikos, and N. Paragios. «Deformable Medical Image Registration: A Survey». In: *IEEE Transactions on Medical Imaging* 32.7 (2013), pp. 1153–1190 (cit. on p. 8).
- [46] T. W. Sederberg and S. R. Parry. «Free-form deformation of solid geometric models». In: *ACM SIGGRAPH Computer Graphics* 20.4 (Aug. 1986), pp. 151–160 (cit. on p. 8).

- [47] D. Rueckert et al. «Nonrigid registration using free-form deformations: application to breast MR images». In: *IEEE Transactions on Medical Imaging* 18.8 (1999), pp. 712–721 (cit. on p. 8).
- [48] Z. Zhao et al. «Augmented reality technology in image-guided therapy: State-of-the-art review». In: *Proceedings of the Institution of Mechanical Engineers, Part H: Journal of Engineering in Medicine* 235.12 (July 2021), pp. 1386–1398 (cit. on p. 9).
- [49] F. Kerber et al. «Is autostereoscopy useful for handheld AR?» In: *Proceedings of the 12th International Conference on Mobile and Ubiquitous Multimedia. MUM '13. ACM, Dec. 2013* (cit. on p. 9).
- [50] *F2554 Standard Practice for Measurement of Positional Accuracy of Computer Assisted Surgical Systems*. <https://www.astm.org/f2554-10.html>. Accessed: 2024-01-08. 2024 (cit. on p. 10).
- [51] A. Sorriente et al. «Optical and Electromagnetic Tracking Systems for Biomedical Applications: A Critical Review on Potentialities and Limitations». In: *IEEE Reviews in Biomedical Engineering* 13 (2020), pp. 212–232 (cit. on p. 11).
- [52] G. Welch and E. Foxlin. «Motion tracking: no silver bullet, but a respectable arsenal». In: *IEEE Computer Graphics and Applications* 22.6 (2002), pp. 24–38 (cit. on p. 11).
- [53] *Azure Kinect DK – Develop AI Models | Microsoft Azure*. <https://azure.microsoft.com/en-us/products/kinect-dk>. Accessed: 2024-01-01. 2024 (cit. on p. 12).
- [54] qm13. *Azure Kinect DK hardware specifications | Microsoft Learn*. <https://learn.microsoft.com/en-us/azure/kinect-dk/hardware-specification>. Accessed: 2024-01-01. 2024 (cit. on p. 13).
- [55] S. Royo and M. Ballesta-Garcia. «An Overview of Lidar Imaging Systems for Autonomous Vehicles». In: *Applied Sciences* 9.19 (Sept. 2019), p. 4093 (cit. on p. 13).
- [56] *Passive Marker Spheres: Reflective Tracking Options - NDI*. <https://www.ndigital.com/optical-navigation-technology/passive-marker-spheres/>. Accessed: 2024-01-02. 2024 (cit. on p. 16).
- [57] *etiennedub/pyk4a: Python 3 wrapper for Azure-Kinect-Sensor-SDK*. <https://github.com/etiennedub/pyk4a/>. Accessed: 2024-01-03. 2024 (cit. on p. 18).
- [58] *OpenCV: Hough Circle Transform*. https://docs.opencv.org/3.4/d4/d70/tutorial_hough_circle.html. Accessed: 2024-01-04. 2024 (cit. on p. 20).

- [59] D. Kerbyson and T. Atherton. «Circle detection using Hough transform filters». In: *Fifth International Conference on Image Processing and its Applications, 1995*. 1995, pp. 370–374 (cit. on p. 20).
- [60] J. C. Gower. «Generalized procrustes analysis». In: *Psychometrika* 40.1 (Mar. 1975), pp. 33–51 (cit. on p. 22).
- [61] G. Welch, G. Bishop, et al. «An introduction to the Kalman filter». In: (1995) (cit. on p. 25).
- [62] J. Postel. *User Datagram Protocol*. Aug. 1980 (cit. on p. 29).
- [63] *X-rays*. <https://www.nibib.nih.gov/science-education/science-topics/x-rays>. Accessed: 2024-01-30. 2024 (cit. on p. 30).
- [64] T. M. Peters and C. A. Linte. «Image-guided interventions and computer-integrated therapy: Quo vadis?» In: *Medical Image Analysis* 33 (Oct. 2016), pp. 56–63 (cit. on p. 31).
- [65] joyjaz. *Microsoft HoloLens | Microsoft Learn*. <https://learn.microsoft.com/en-us/hololens/>. Accessed: 2024-01-15. 2024 (cit. on p. 32).
- [66] B. Fida et al. «Augmented reality in open surgery». In: *Updates in Surgery* 70.3 (July 2018), pp. 389–400 (cit. on p. 36).
- [67] R. R. McKnight et al. «Virtual Reality and Augmented Reality—Translating Surgical Training into Surgical Technique». In: *Current Reviews in Musculoskeletal Medicine* 13.6 (Aug. 2020), pp. 663–674 (cit. on p. 36).
- [68] M. Hofer, G. Strauß, K. Koulechov, and A. Dietz. «Definition of accuracy and precision—evaluating CAS-systems». In: *International Congress Series* 1281 (May 2005), pp. 548–552 (cit. on p. 40).
- [69] A. Cangelosi et al. «Mixed Reality for Orthopedic Elbow Surgery Training and Operating Room Applications: A Preliminary Analysis». In: *Smart Tools and Applications in Graphics*. Eurographics Association, 2023 (cit. on p. 74).
- [70] G. M. Costa, M. R. Petry, J. G. Martins, and A. P. G. M. Moreira. «Assessment of Multiple Fiducial Marker Trackers on HoloLens 2». In: *IEEE Access* 12 (2024), pp. 14211–14226 (cit. on p. 75).
- [71] *jdibenes/hl2ss: HoloLens 2 Sensor Streaming*. <https://github.com/jdibenes/hl2ss>. Accessed: 2024-03-05. 2024 (cit. on p. 75).
- [72] F. Suligoj et al. «Automated Marker Localization in the Planning Phase of Robotic Neurosurgery». In: *IEEE Access* 5 (2017), pp. 12265–12274 (cit. on p. 77).
- [73] B. Jerbić et al. «RONNA G4—Robotic Neuronavigation: A Novel Robotic Navigation Device for Stereotactic Neurosurgery». In: *Handbook of Robotic and Image-Guided Surgery*. Elsevier, 2020, pp. 599–625 (cit. on p. 77).

- [74] R. Flamary et al. «POT: Python Optimal Transport». In: *Journal of Machine Learning Research* 22.78 (2021), pp. 1–8 (cit. on p. 79).